Doklady Physics, Vol. 45, No. 8, 2000, pp. 359–362. Translated from Doklady Akademii Nauk, Vol. 373, No. 4, 2000, pp. 466–469.

PHYSICS

Association in Metallic Melts and Its Relation to Amorphization: Fe–P Alloys

A. I. Zaĭtsev, N. E. Shelkova, and A. D. Litvina

Presented by Academician O.A. Bannykh November 18, 1999

Received November 18, 1999

As a rule, the melts inclined to amorphization are characterized by an intense interparticle interaction. It is precisely the melts in which the association of their components occurs and which is accompanied by the formation of molecule-like complexes or clusters. However, the relationship of these two phenomena has not been analyzed until now. This work deals with such an analysis.

In the systems that can easily pass into amorphous state, the heat capacity for supercooled liquid, C_p(liq), is much higher than that for equilibrium crystals, C_p(cr). Hence, the entropy of supercooled liquid decreases with temperature much more quickly than the crystal entropy, and, at a temperature T_K, the entropies of these two phases would become equal. In fact, the vitrification occurs at the temperature $T_g > T_K$ [1]. Thus, the temperature T_K is a lower bound of the vitrification temperature T_g, and the glass entropy at T_g is larger than the crystal entropy. To consider the relative stability of liquid and crystals, we use the Gibbs melting energy at arbitrary temperature:

$$\Delta_m G = \Delta_m S(T_m - T) - \int_T^{T_m} \Delta C_p dT + T\int_T^{T_m} \frac{\Delta C_p}{T} dT. \quad (1)$$

Here, $\Delta_m S$ is the entropy of melting at the temperature T_m, and $\Delta C_p = C_p(\text{liq}) - C_p(\text{cr})$. To simplify our analysis, we assume that ΔC_p is independent of temperature. This assumption does not change the essence of our conclusions and allows equation (1) to be rewritten in the form

$$\Delta_m G = \Delta_m S(T_m - T) + \Delta C_p\left(T\left(1 + \ln\frac{T_m}{T}\right) - T_m\right). \quad (2)$$

The difference $T(1 + \ln(T_m/T)) - T_m$ is negative for $T < T_m$, and the two terms in equation (2) are of different sign: The first is positive, and the second is negative. Thus, decreasing $\Delta_m S$ and increasing ΔC_p result both in approaching the vitrification temperature T_g to the melting temperature T_m and increasing the thermodynamic stability against crystallization of supercooled liquid and, consequently, glass.

Keeping in mind that functions $\Delta_m S$ and ΔC_p are vital to the vitrification thermodynamics, we will consider the effect of association processes in liquid on these characteristics. Our analysis is performed within the framework of the model of ideal associated solutions for a binary melt A–B because the essence of our results is unaffected by either the introduction of an additional term, allowing for the interaction between the components of the associated solution, or the increase in the number of these components. The entropy of formation for an associated solution takes the form of two terms with different signs:

$$\Delta_f S = \sum n(A_iB_j)\Delta_f S(A_iB_j) - R\left\{\sum n(A_iB_j)\ln x(A_iB_j) + n(A_1)\ln x(A_1) + n(B_1)\ln x(B_1).\right\} \quad (3)$$

Here, $n(A_iB_j)$ and $\Delta_f S(A_iB_j)$ are the number of moles and the entropy of formation, respectively, for the associated complexes A_iB_j; $x(A_iB_j)$, $x(A_1)$, and $x(B_1)$ are the molar fractions of the complexes and two monomer particles, respectively, in the associated solution. The first (negative) term in (3) is due to the arising complexes, while the second (positive) term is related to the mixing of components in the associated solution. By lowering the temperature of the melt, the absolute value of first term increases and second term decreases. As a result, the entropy of formation for the solution decreases. At temperatures close to the liquidus, the first contribution dominates. In this case, the more complicated the empirical formula for a complex, the greater the decrease in entropy, because the decrease in the number of particles in the solution becomes much

Institute of the Physics of Metals and Structure Materials, Bardin Central Research Institute for the Iron and Steel Industry, Vtoraya Baumanskaya ul. 9/23, Moscow, 107005 Russia

1028-3358/00/4508-0359$20.00

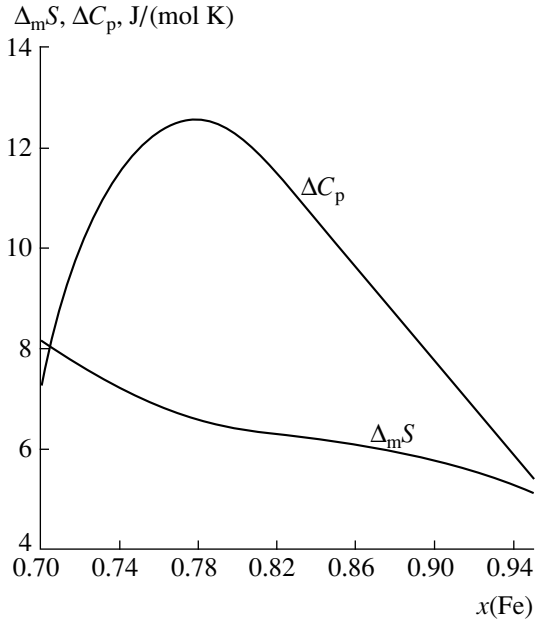

Fig. 1. Entropy of melting and ΔC_p for the Fe–P melt at 1321 K as versus concentration.

more pronounced [2]. As a consequence, the value of $\Delta_m S$ also decreases.

In the case of a single association reaction, with its enthalpy being independent of temperature, the excess (with respect to the additive sum of the heat capacities for pure liquid components) in the heat capacity for the associated solution is given by the expression

$$C_p^E = \frac{[\Delta_f H(A_i B_j)]^2}{\left\{RT^2\left[\frac{1}{x(A_i B_j)} + \frac{i^2}{x(A_1)} + \frac{j^2}{x(B_1)}\right]\right\}}. \quad (4)$$

In the case of a large number of association reactions, similar expressions take a cumbersome form, but the essence of the analysis is not changed. It follows from (4) that C_p^E is always positive. In other words, the occurrence of association processes results in increasing both the heat capacity of liquid and, consequently, the difference between the heat capacities of liquid and crystals. This increase is directly proportional to the enthalpy squared of formation for the associative complex and inversely proportional to the absolute temperature squared. When analyzing the temperature dependence of C_p^E, we have to take into account that the mole fractions of the complexes and monomer particles also depend on temperature. Our numerical analysis of equation (4) indicated that, for arbitrary thermodynamic parameters of an association reaction, the concentration dependence of C_p^E exhibits a peak when the macroscopic composition of the solution corresponds to the composition of an associative complex. In melts with several association reactions, the extremum corresponds to the association composition characterized by the minimum enthalpy of formation. The effect of other association reactions is less significant and increases with temperature. Thus, association processes in a liquid result in decreasing the entropy and in increasing the excessive heat capacity; i.e., they are favorable to the transition of the liquid to a glassy state.

We now consider the effect of association processes on the melt viscosity, that is, the most important property determining the kinetics of liquid–glass transition. To do this, we use the equation relating the viscosity to the configurational entropy S^{conf} [3]:

$$\ln(\eta) = A_e + \frac{B_e}{TS^{conf}}. \quad (5)$$

Here, A_e and B_e are constants. The temperature dependence of the configurational entropy can be presented in the following form:

$$S^{conf}(T) = S^{conf}(T_g) + \int_{T_g}^{T} \frac{C_p^{conf}}{T} dT. \quad (6)$$

Here, C_p^{conf} is the configurational heat capacity; and $S^{conf}(T_g)$ is the configurational entropy of the liquid at the glass transition temperature T_g, which remains fixed when the liquid transforms into a glassy state. According to [3], $S^{conf}(T_g)$ can be presented as the difference between the entropies of supercooled liquid and crystals at the temperature T_g. Similarly, the configurational heat capacity is close to a difference between the heat capacities of liquid and crystals, i.e., to ΔC_p.

The greater the liquid viscosity and the steeper its increase in the course of the supercooling of a melt, the more favorable, from the standpoint of kinematics, is the transition of the liquid into a glassy state [3]. According to (5) and (6), this transition occurs at high values of the configurational heat capacity and at low values of the configurational entropy at temperature T_g. In essence, these conditions coincide with the requirement that ΔC_p should be large and that ΔS_m should be small. Thus, from the viewpoint of both kinetics and thermodynamics, the association processes in a liquid are favorable to its amorphization.

We use the formulas obtained to quantitatively describe the amorphization of the iron–phosphorus melt. This melt is an ideal associated solution in which the aggregates such as FeP, Fe_2P, and Fe_3P are formed. The thermodynamic functions of their formation are as follows (with $\Delta_f H$ in J/mol and $\Delta_f S$ in J/(mol K)) [4]: $\Delta_f H(FeP) = -81025$, $\Delta_f S(FeP) = -1.4$, $\Delta_f H(Fe_2P) = -14599$, $\Delta_f S(Fe_2P) = -15.6$, $\Delta_f H(Fe_3P) = -207390$, and $\Delta_f S(Fe_3P) = -53.5$. These parameters and thermodynamic functions for crystal phases allow us to evaluate the concentration dependences of both the entropy

of melting and ΔC_p at the eutectic temperature of 1321 K (Fig. 1) [4]. If we take into account that the entropy of melting decreases with temperature and that only the eutectic alloy with $x(\mathrm{Fe}) = 0.826$ melts at the temperature of 1321 K, the results presented in Fig. 1 allow us to find the concentration range, $0.77 < x(\mathrm{Fe}) < 0.86$, in which the melt is most inclined to amorphization. This conclusion is very consistent with the available data [5–7]. It is precisely the concentration range in which the biggest complexes Fe_3P are intensively formed.

Typical features of the thermodynamic functions for the transition of crystal compounds into a supercooled liquid or glassy state are shown in Fig. 2 for an eutectic alloy. To evaluate these functions, we used the data of [8, 9] for pure components. It is clear that both the enthalpy and entropy of the transition vary irregularly with temperature. This is due to the magnetic contributions to the thermodynamic functions of the solid solutions (with body-centered cubic lattices) of phosphorus in Fe and Fe_3P. The separated nonmagnetic components of $\Delta_{tr}H$ and $\Delta_{tr}S$ monotonically decrease with temperature. According to the data available in literature [5–7], the temperatures of vitrification and crystallization for amorphous iron–phosphorus alloys almost coincide and are close to 650 K. At this temperature, we have $\Delta_{tr}S = 4.48$ J/(mol K), $\Delta_{tr}H = 6054$ J/mol, and $\Delta_{tr}G = 3141$ J/mol. The crystallization enthalpy for the amorphous alloy Fe–P with an eutectic composition was found by the authors of [5] to be equal to –6.3 kJ/mol. This value nearly coincides with the result of present calculations.

To approximate the temperature dependence of viscosity for the melts Fe–P, we assumed that the configurational entropy at the vitrification temperature was equal to the difference between the entropy of supercooled liquid (glass) and the nonmagnetic part of entropy of equilibrium crystalline composition. The configurational heat capacity was evaluated as the difference between the heat capacity of melt and the nonmagnetic part of the heat capacity of crystals. These assumptions allowed us to describe, within the accuracy of experimental data, the temperature dependence of viscosity for iron–phosphorus melts [5, 10–12] in a wide range (more than 1200 K) from the vitrification temperature of 650 K to metallurgy temperatures of 1823–1873 K. The accuracy of the description for a melt with an eutectic composition is illustrated in Fig. 3. In this case, we found the following values of the constants in equation (5): $A_e = 44\,078 \pm 540$ and $B_e = -6.17 \pm 0.17$.

In conclusion, it is worth emphasizing that our results give unambiguous evidence of a direct relationship between the phenomena of association and amorphization. Moreover, the concept of association makes it possible to quantitatively treat thermal and transport properties of melts in the course of their transition into the glassy state.

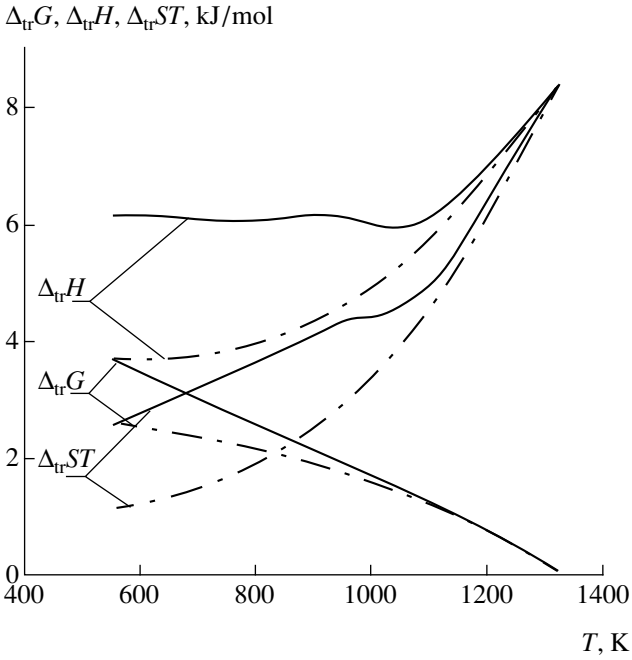

Fig. 2. Temperature dependences of (solid lines) the thermodynamic functions for the transition of the crystal compound Fe–P with an eutectic composition into glassy state or supercooled (metastable) melt and (dot–dash lines) the differences between the corresponding thermodynamic functions of liquid and of nonmagnetic constituents of crystals.

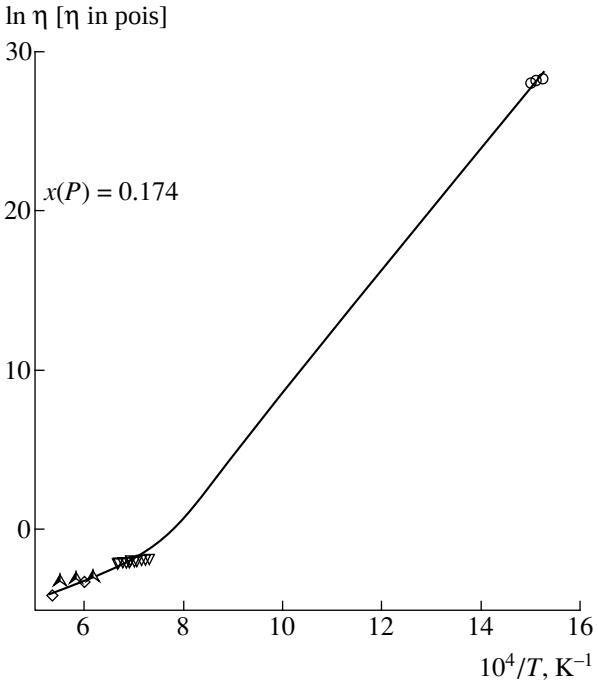

Fig. 3. Temperature dependences of the viscosity for the melt Fe–P with an eutectic composition. Solid line is the result of our calculations based on Eqs. (5) and (6); the points are the experimental data of [5] (circles), [10] (triangles), [11] (double triangles), and [12] (diamonds).

ACKNOWLEDGMENTS

This work was supported by the Russian Foundation for Basic Research, project no. 99-02-16465.

We thank B.M. Mogutnov for helpful remarks and participation in discussions of the results.

REFERENCES

1. O. V. Mazurin, *Structure and Stabilization of Inorganic Glasses* (Nauka, Leningrad, 1978).
2. A. I. Zaitsev and B. M. Mogutnov, High Temp. Mater. Sci. **34**, 155 (1995).
3. P. Richet and D. R. Neuville, Adv. Phys. Geochem. **10**, 132 (1992).
4. A. I. Zaitsev, Zh. V. Dobrokhotova, A. D. Litvina, and B. M. Mogutnov, J. Chem. Soc., Faraday Trans. **91**, 703 (1995).
5. K. Russew, L. Anestiev, L. Stojanova, and L. Sapondjiev, J. Mater. Sci. Technol. **3** (2), 3 (1995).
6. T. Miyazaki, Y. Xingbo, and M. Takahashi, J. Magn. Magn. Mater. **60**, 204 (1986).
7. M. Naka, T. Masumoto, and H. S. Chen, J. Phys. Colloq. **41**, C8-839 (1980).
8. A. T. Dinsdale, CALPHAD: Comput. Coupling Phase Diagrams Thermochem. **15**, 317 (1991).
9. I. Karakaya and W. T. Thompson, Bull. Alloy Phase Diagrams **9**, 232 (1988).
10. Y. Nishi, K. Watanabe, K. Suzuki, and T. Masumoto, J. Phys. Colloq. **41**, C8-359 (1980).
11. I. Dragomir, A. F. Vishkarev, and V. I. Yavoĭskiĭ, Izv. Vyssh. Uchebn. Zaved., Chern. Metall., No. 7, 48 (1964).
12. A. A. Vostryakov, N. A. Vatolin, and O. A. Esin, Fiz. Met. Metalloved. **18**, 476 (1964).

Translated by V. Chechin

Doklady Physics, Vol. 45, No. 8, 2000, pp. 363–366. Translated from Doklady Akademii Nauk, Vol. 373, No. 4, 2000, pp. 470–473.

PHYSICS

Studies of Mechanical Properties of Quasicrystalline Al–Cu–Fe Phase by the Indentation Technique

Academician V. I. Trefilov, Yu. V. Mil'man, D. V. Lotsko, A. N. Belous, S. I. Chugunova, I. I. Timofeeva, and A. I. Bykov

Received April 7, 2000

A special packing of atoms in quasicrystals, which is characterized by the absence of translational periodicity and the predominantly covalent type of interatomic bonds [1], causes a specific character of their mechanical properties. Quasicrystals are brittle materials with a nearly vanishing macroscopic plasticity [2]. At the same time, in measuring the hardness, distinct indentations are formed, and scratching causes striations and cuttings [3, 4]; i.e., the microplasticity is revealed under high-pressure local deformation. The brittle state of quasicrystals is retained up to relatively high temperatures (600°C for Al–Cu–Fe, 700°C for Al–Pd–Mn), and with a further increase of deformation temperature, the compression testing reveals rather high microplasticity—the deformation prior to fracture can exceed 70–80% [2, 5, 6]. The deformation of quasicrystals at elevated temperatures is characterized by a pronounced work softening, which is observed neither in crystalline nor in amorphous materials.

At least, in Al–Pd–Mn (icosahedral quasicrystal), the phenomenon of work softening at elevated temperatures was explained based on the dislocation mechanism of deformation [6]. The Bürgers vector in quasicrystals has two components, the phonon and phason ones. When the dislocations move, the phason component induces a structural and chemical disorder in contrast to the case of the phonon component, which is similar to the Bürgers vector of dislocations in crystals. It was argued in [6] that the deformation of Al–Pd–Mn quasicrystals is controlled by the obstacles in the form of Mackay's pseudoclusters consisting of 51 atoms. The moving dislocations disturb the ordered atomic arrangement in clusters, giving rise to the corresponding increase in the entropy. As a result, the activation energy decreases, and the deformation is facilitated. A significant enhancement of the phason components in the Bürgers vectors of dislocations with the growth of strains was observed in experiments [5].

The quasicrystalline icosahedral Al–Cu–Fe phase (an approximate composition $Al_{63}Cu_{25}Fe_{12}$) is very interesting to researchers, since it has high values of hardness (HV ≤ 10 GPa), elastic modulus ($E \approx$ 100 GPa), and wear resistance [3]. In addition, this phase is thermodynamically stable [3]. Recently, it has been established [7] that the deformation of the polycrystalline Al–Cu–Fe phase occurs within the characteristic bands, where a high density of dislocations is observed; the dislocations are grouped in networks or walls. The analysis of the obtained results and the available published data allowed the authors of [7] to conclude that under plastic deformation there occurs the phase transformation of a quasicrystalline phase into an approximant phase characterized by atomic packing with a translational periodicity along one of the fivefold axes.

There is still no consensus concerning the nature of low-temperature microplasticity of quasicrystals. It was argued that it can be caused by a phase transition into a more plastic phase under the indenter [3], but there is no proof confirming the existence of such a transition.

Recently, a new method based on the indentation technique was proposed to determine mechanical properties of low-plasticity materials [8, 9]. The calculations of a mean deformation at the indenter–sample contact area allow us to plot the deformation curve similar to the stress–strain curve, which is obtained under uniaxial loading. This can be done with the help of a set of indenters with different angles at the top. A new characteristic of the material plasticity δ_H is represented, which is defined as a contribution of plastic strain to the total elastoplastic strain under the indenter [8].

In this paper, the results of the first implementation of this method to the studies of mechanical properties of compact Al–Cu–Fe quasicrystalline material are presented. The set of the used methods also includes the

Frantsevich Institute of Materials Science Problems, National Academy of Sciences of Ukraine, ul. Krzhizhanovskogo 3, Kiev, 252680 Ukraine

1028-3358/00/4508-0363$20.00

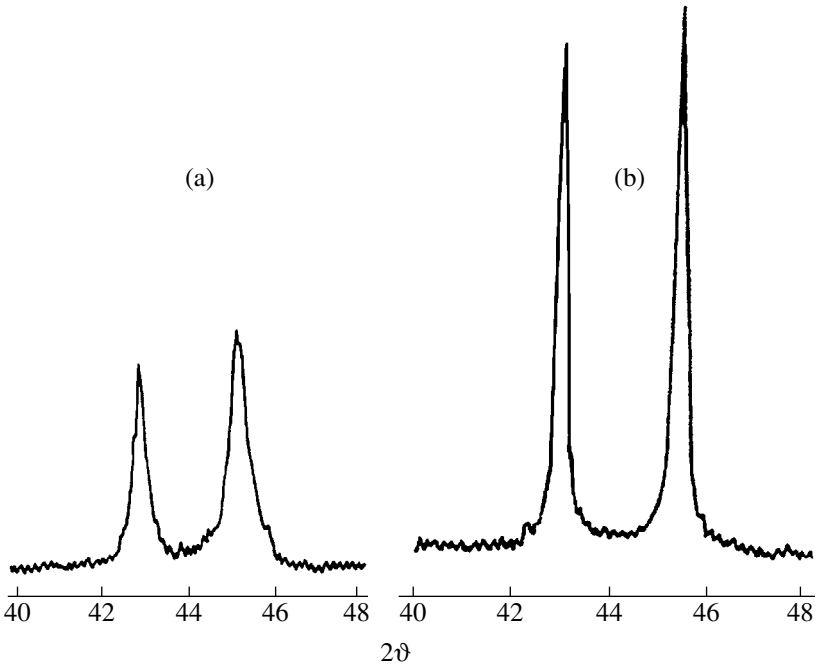

Fig. 1. Regions in X-ray diffraction patterns of the pressed samples: (a) sample 1 (annealing of the powder prior to pressing; (b) sample 2 (annealing of the pressed sample).

analysis of the temperature dependence of hardness and the estimates of the elastic modulus based on the results of indentation with the recording of the loading diagram.

The powder with a quasicrystalline Al–Cu–Fe phase was obtained by sputtering the melt in the air flow. Compact samples having cylindrical shape with the diameter and height equal to 5 mm were prepared by pressing the powder with the particle size 50–100 μm in the high-pressure chamber at 700°C under quasihydrostatic compression. The measurement of the hardness was performed at the end surfaces of the samples subjected to the mechanical grinding and polishing. The powders and sintered samples were annealed for 2 h in the vacuum furnace at 700°C in order to obtain a single-phase quasicrystalline state. Both the powder prior to pressing (sample 1) and the pressed cylinder (sample 2) were annealed.

The hardness at the elevated temperatures was measured in vacuum, and the low-temperature hardness, under the layer of the cooling liquid. For studies of the temperature dependence of hardness, the Vickers indenter was used, and for the plotting of the deformation curve, the set of trihedral pyramidal indenters with the angles at the top $\gamma = 45°, 55°, 60°, 65°, 70°, 75°$, and 80°. The X-ray diffraction studies were carried out using the filtered CuK_α radiation. The density was determined by hydrostatic weighing.

Mechanical properties and density of the pressed samples

Sample	Treatment	HV, GPa	E, GPa	δ_H	ρ, g/cm^3
1	Annealing prior to pressing	4.37	113	0.612	4.709
2	Annealing after pressing	7.53		0.419	4.693

The metallographic studies of polished surfaces of the samples revealed the regions of homogeneous material with the size by the order of magnitude larger than the sizes of the powder particles. There were also large pores (30–50 μm in diameter) at the distance of about 1 mm from each other.

The X-ray diffraction study (Fig. 1) revealed a pronounced difference in the linewidths for samples 1 and 2, i.e., the pressing in the range of the high-temperature plasticity led to a significant increase of the defect density in the material, and the subsequent annealing eliminated these defects. The hardness and plasticity characteristics of these samples at room temperature turned out to be also quite different (see the table). This difference cannot be attributed to the different porosity, since the densities of the samples are very close, the density of a hard sample being somewhat lower. The elastic modulus determined by us (see, table) corresponds to the upper limit reported in the literature for Al–Cu–Fe quasicrystals [6].

The deformation curves obtained by the indentation method are presented in Fig. 2 for samples 1 and 2. The deformation curves plotted in the coordinates which are the mean contact pressure (hardness according to Meyer HM) and the total strain at the contact area ε_t

exhibit a pronounced softening, which is especially high for sample 2. Thus, it is shown that the deformation curves at room temperature have the same character as that at elevated temperatures [2, 5, 6].

Following [9], we calculated the values of δ_H using expression

$$\delta_H = 1 - 14.3(1 - \nu - 2\nu^2)\frac{HV}{E}, \qquad (1)$$

where E and ν are the elastic modulus and the Poisson coefficient for the material deformed by the diamond indenter. In the literature, we were unable to find the value of ν needed to estimate E [10] for Al–Cu–Fe. In calculations, we put $\nu = 0.28$ in agreement with the measured elastic constants of Al–Pd–Mn quasicrystal [11].

We pay attention to two regions in the temperature dependence of hardness (Fig. 3): the 78–673 K range, where the hardness changes only slightly and the range above 673 K characterized by an abrupt decrease in the hardness. In the secondary electron image of the hardness indentation for sample 2, "tongues" are seen at room temperature (a thin layer pressing out around the indentation) (Fig. 4). The increase in δ_H corresponds to the decrease in hardness with the growth of temperature. Both tetrahedral and trihedral indenters give rise to radial cracks appearing sometimes at the top of indentation. However, it was impossible to find any regularities relating the arising cracks to the load magnitude and the shape of indenter. The surface of the indentations was smooth, without indications of fracture and slip of the material.

The athermal region on the HV(T) curve in Fig. 3 is similar to that observed earlier by Gridneva, Mil'man, and Trefilov [12] for single crystals of Si and Ge semiconductors and then by Suzuki and Ohmura [13] at nanoindentation of Si. It was shown in [12] that under effect of the indenter, such a region can be caused by the pressure-induced transition to the more plastic metallic phase. Near the low-temperature indentations in silicon, the "tongues" of the plasitified material were found [13].

In recent experiments, it was found that the icosahedral Al–Cu–Fe phase remains stable under the quasihydrostatic pressure up to 35 GPa [14]. A different situation takes place upon deviation from the quasihydrostatic conditions. It was shown in the case of Al–Pd–Mn that, under the uniaxial load applied to the sample placed in the high-pressure cell, we have the transformation of quasicrystalline phase to the crystalline bcc phase at 20 GPa with the grain size about 3–6 nm. The grains are surrounded by amorphous interlayers [15]. It is obvious that under intrusion of the indenter, the stressed state is close to the latter case.

The mean stress at the contact area is $\sigma = P/S$, where P is the load on the indenter and S is the contact area. For P = const, at the first stages of loading, when S is small, the pressure-induced phase transformation occurs under the indenter. The arising plastic phase is

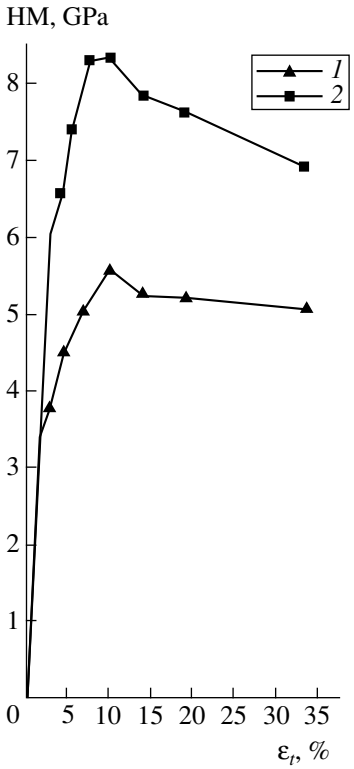

Fig. 2. Hardness according to Meyer versus total strain under the indenter. The designation of samples corresponds to Fig. 1.

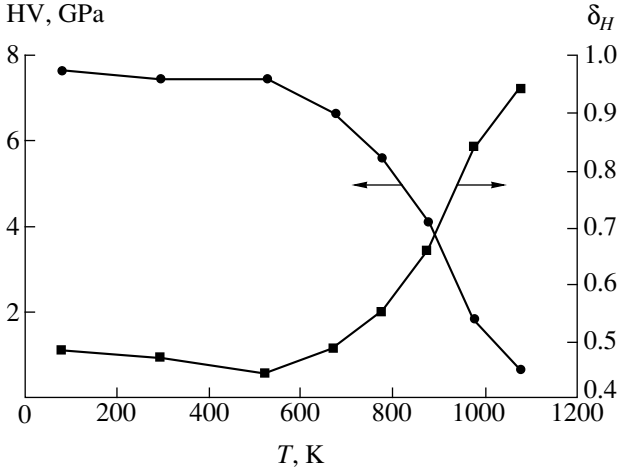

Fig. 3. Temperature dependence of the hardness HV and plasticity characteristic δ_H for sample 2 (load P = 2.34 N).

pressed out in the shape of thin interlayers, area S is increases, and stress σ decreases. The indenter stops when $\sigma = \sigma_{cr}$, where σ_{cr} is the threshold pressure of the phase transition. Thus, we have HV = σ_{cr} in the athermal region.

These results (the work softening at room temperature, the athermal region on the HV(T) curve, the "tongues" around the indentation) and the literature

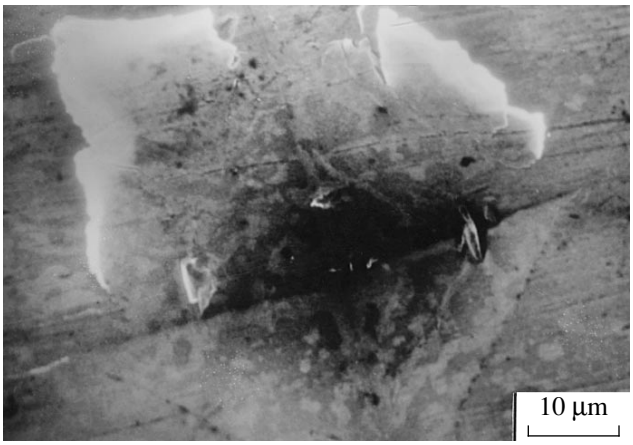

Fig. 4. Secondary electron image of the Vickers indentation at room temperature for sample 2 (P = 5 N).

data [2, 5] suggest that the phase transition in quasicrystals is related to the process of plastic deformation, in the course of which the accumulation of phason distortions results in the violation of the order in the atomic packing. It is clear that with the temperature decrease, the dislocation density in the layer under the indenter increases, despite the reduction in the magnitude of plastic strain under the indenter characterized by δ_H. This occurs owing both to the decrease in the dislocation mobility and the slowing in the process of polygonization and recovery. One can suggest that the observed indications of the phase transition are related to the attainment of a certain critical value for the density of dislocations.

Together with the decrease in hardness, the characteristic of plasticity δ_H increases with temperature reaching the value of 0.95 at 1073 K (Fig. 3). According to [8], the macroscopic plasticity manifests itself at $\delta_H \approx 0.9$ in the crystalline (mainly, metallic) materials. The comparison of the temperature dependence of δ_H and the results of compression tests [2] demonstrates that in Al–Cu–Fe quasicrystals it arises at much lower δ_H values, $\delta_H \approx 0.7$. Note that the estimate of δ_H in Fig. 3 was performed without taking into consideration the temperature dependence of the elastic modulus. The account taken of this dependence results in a certain decrease in the magnitude of δ_H at elevated temperatures. Such an early manifestation of the microscopic plasticity can be related both to the features of the deformation mechanism of quasicrystals and to the different conditions of testing under compression and tension.

It is of interest to note that, in contrast to the crystalline materials, the accumulation of distortions in the Al–Cu–Fe quasicrystal in the course of high-temperature deformation (at pressing) drastically reduced the hardness under these conditions (see table). The elimination of these distortions by annealing enhanced the hardness.

REFERENCES

1. K. Kimura, H. Matsuda, R. Tamura, *et al.*, in *Proceedings of the V International Conference on Quasicrystals*, Avignon, 1995 (World Scientific, Singapore, 1995), pp. 730–738.
2. L. Bresson and D. Gratias, J. Non-Cryst. Solids **153**/**154**, 468 (1993).
3. U. Köster, W. Liu, H. Liebertz, *et al.*, J. Non-Cryst. Solids **153**/**154**, 446 (1993).
4. E. Hornbogen and M. Schandl, Z. Metallkd. **83** (2), 128 (1992).
5. S. S. Kang and J. M. Dubois, Philos. Mag. A **66** (1), 151 (1992).
6. M. Feuerbacher, C. Metzmacher, M. Wollgarten, *et al.*, Mater. Sci. Eng., A **233**, 103 (1997).
7. U. Köster, X. L. Ma, J. Greiser, *et al.*, in *Proceedings of the VI International Conference on Quasicrystals*, Tokyo, 1997 (World Scientific, Singapore, 1997), pp. 505–508.
8. Yu. V. Milman, B. A. Galanov, and S. I. Chugunova, Acta Metall. Mater. **41**, 2523 (1993).
9. Yu. V. Mil'man, in *Modern Materials Science of the XXI Century* (Naukova Dumka, Kiev, 1998), pp. 637–656.
10. B. A. Galanov, O. N. Grigor'ev, Yu. V. Mil'man, *et al.*, Probl. Prochn., No. 6, 52 (1990).
11. Y. Amazit, M. Fisher, B. Perrin, *et al.*, in *Proceedings of the V International Conference on Quasicrystals, Avignon*, 1995 (World Scientific, Singapore, 1995), pp. 584–587.
12. I. V. Gridneva, Yu. V. Mil'man, and V. I. Trefilov, Phys. Status Solidi A **14** (1), 177 (1972).
13. T. Suzuki and T. Ohmura, Philos. Mag. A **74** (5), 1073 (1996).
14. J. P. Itie, S. Lefebvre, A. Sadac, *et al.*, in *Proceedings of the V International Conference on Quasicrystals, Avignon, 1995* (World Scientific, Singapore, 1995), pp. 168–171.
15. Y. Yan, N. Baluc, J. Peyronneau, *et al.*, in *Proceedings of the V International Conference on Quasicrystals, Avignon, 1995* (World Scientific, Singapore, 1995), pp. 668–671.

Translated by T. Galkina

Doklady Physics, Vol. 45, No. 8, 2000, pp. 367–371. Translated from Doklady Akademii Nauk, Vol. 373, No. 5, 2000, pp. 607–610.

PHYSICS

Parabolic Approximation in the Theory of the Sound Propagation in Three-Dimensionally Heterogeneous Media

O. A. Godin

Presented by Academician L.M. Brekhovskikh October 27, 1999

Received November 26, 1999

The parabolic approximation [1; 2; 3, Section 7.6] is widely used in the mathematical simulation of wave fields, in particular, in oceanic and atmospheric acoustics. In a wide scope of direct and inverse problems for finding the physically significant results in terms of this approximation, it is necessary [4–6] for the reciprocity principle and the energy conservation law expressing the fundamental symmetries of the true wave field to remain valid for the solutions to the parabolic equation. Wide-angle parabolic equations providing the validity of the reciprocity principle and the energy conservation in two-dimensional problems related to the propagation of sound in media with piece-wise continuous variation of parameters along the trace are proposed in [7, 8]. The goal of this study is the generalization of these results to the three-dimensional case. We propose a class of energy-conserving and reciprocal three-dimensional parabolic equations and investigate the properties of their solutions.

In stagnant fluid with the time-independent density ρ and the velocity of sound c, the acoustic pressure satisfies the equation [see 3, Section 4.1]

$$\frac{\partial}{\partial x}\left(\frac{1}{\rho}\frac{\partial p}{\partial x}\right) + k_0^2(1+\hat{S})p = Q,$$
$$\hat{S} = \frac{\rho}{k_0^2}\left[\frac{\partial}{\partial y}\left(\frac{1}{\rho}\frac{\partial}{\partial y}\right) + \frac{\partial}{\partial z}\left(\frac{1}{\rho}\frac{\partial}{\partial z}\right)\right] + \frac{k^2}{k_0^2} - 1. \quad (1)$$

Here, $k(x) = \omega/c$ is the wave number; ω is the wave frequency; $k_0 = \text{const}$; and $Q = i\omega\rho a + \rho\nabla(\rho^{-1}\mathbf{f})$, where a and $\mathbf{f}$ are the volume densities for sources of both the volume velocity and extraneous force. For simplicity, we assume ρ and c to be smooth functions of coordinates and the media to be boundless or to have ideal (absolutely soft or absolutely rigid) boundaries, which are invariant with respect to the translations along the Ox-axis. The differential operator $\hat{S}$ is self-conjugate with respect to the scalar product

$$\langle p^{(1)}, p^{(2)}\rangle = \iint dydz\, p^{(1)}(p^{(2)})^*/\rho(x), \quad (2)$$

where the integration is carried out over the waveguide cross section. The Ox-axis is chosen along the preferential direction of the wave propagation. It is assumed that the medium parameters vary either weakly or smoothly with x and that the propagation constants ξ_n for local modes contributing substantially to the acoustic field are concentrated in the neighborhood of k_0, so that $\varepsilon \equiv \|\hat{S}p\|/\|p\| \ll 1$.

Similarly to [8], where the two-dimensional case was investigated, we consider the three-dimensional parabolic equation in the form

$$[\rho^{-1/2}\Phi_2(\hat{S})p]_x = ik_0\rho^{-1/2}\Phi_1(\hat{S})p\Phi_2(\hat{S})p + \rho^{-1/2}g(\hat{S})Q, \quad (3)$$

where $\Phi_N(a)$ are the analytical functions satisfying the condition $\Phi_N(a^*) = [\Phi_N(a)]^*$, which serve for approximations of the functions $(1+a)^{1/2N}$, $N = 1, 2$. For $Q = 0$ and $\partial/\partial y = 0$, equations (3) transform into the energy-conserving two-dimensional parabolic equations proposed and investigated in [8]. Efficient methods for solving these equations are developed for the cases when the pseudodifferential operators $(1+\hat{S})^{1/2N}$ are approximated by the rational functions $\Phi_N(\hat{S})$ [9–13].

We determine the function g from the condition that parabolic equation (3) approximates the solutions to the wave equation in the case of a stratified fluid, i.e., when $c = c(z)$, $\rho = \rho(z)$, and the medium is unbounded in y. In the layered medium, the problem is reduced to the two-dimensional case by the Fourier transform with respect

Shirshov Institute of Oceanology, Russian Academy of Sciences, ul. Krasikova 23, Moscow, 117218 Russia

1028-3358/00/4508-0367$20.00

to y. For the point source $Q = \delta(x - x_0)$, the solution to equation (3) for $x \geq x_0$ has the form

$$p(x) = \sum_n \int_{-\infty}^{+\infty} dq \exp[iqy + ik_0\Phi_1(\alpha_n)(x - x_0)] \times \frac{g(\alpha_n) f_n(z) f_n(z_0)}{2\pi\Phi_2(\alpha_n)}, \quad (4)$$
$$\alpha_n = \frac{\xi_n^2 - q^2}{k_0^2} - 1,$$

where $f_n(z)$ and ξ_n are, respectively, the eigenfunctions and the propagation constants of normal waves in a layered waveguide. If the vertical wave operator has a continuous spectrum, the summation over the discrete mode subscript n is supplemented in (4) by integration over the continuous spectrum. Solution to (1) for $x \geq x_0$ also has the form of (4) but differs with respect to the replacement of $k_0\Phi_1(\alpha_n)$ by $(\xi_n^2 - q^2)^{1/2}$ and of $g(\alpha_n)/\Phi_2(\alpha_n)$ by $-0.5i(\xi_n^2 - q^2)^{-1/2}$. Hence, for

$$g = (2ik_0\Phi_2)^{-1}, \quad (5)$$

the solutions to parabolic equation (3) approximate the solutions to wave equation (1) for the waves propagating toward increasing x. The degree of proximity for these solutions is determined by the accuracy of the approximating $(1 + a)^{1/2N}$ by the functions $\Phi_N(a)$. Expanding the solutions in terms of two-dimensional modes $f_{n,m}(y, z)$, it is easy to ascertain that parabolic equation (3), (5) also provides the approximation of the wave equation in a medium with cylindrical boundaries and parameters depending on y and z. In the limiting case when the error of the approximation of $(1 + a)^{1/2N}$ by the functions $\Phi_N(a)$ tends to zero and the field involves only the modes propagating towards increasing x, the difference between the solutions to equation (1) and to parabolic equation (3), (5) vanishes for an arbitrary Q.

We show that the solutions to parabolic equation (3), (5) satisfy the reciprocity principle in the three-dimensionally heterogeneous medium. Let the wave $p_1(x)$ propagating towards increasing x and the wave $p_2(x)$ propagating towards decreasing x be generated by the sources Q_1 and Q_2, respectively. The parabolic equation based on p_2 differs from (3), (5) due to the replacement of k_0 by $-k_0$. Multiplying the parabolic equation for p_2 by $\rho^{-1/2}\Phi_2(\hat{S})p_1$ and summing up the result obtained with the product of (3) by $\rho^{-1/2}\Phi_2(\hat{S})p_2$, integrating with respect to y and z over the waveguide cross section and taking into account that the operator $\hat{S}$ is self-conjugate, we obtain

$$\frac{\partial}{\partial x}\langle\Phi_2(\hat{S})p_1,\ \Phi_2(\hat{S})p_2^*\rangle = \frac{1}{2ik_0}(\langle p_1,\ Q_2^*\rangle - \langle p_2,\ Q_1^*\rangle). \quad (6)$$

In the region free of sources, equation (6) is reduced to the formulation of the reciprocity principle considered for two-dimensional parabolic equations in [7, 8]. Integrating (6) with respect to x, we find

$$\int d^3x p_1 Q_2/\rho = \int d^3x p_2 Q_1/\rho. \quad (7)$$

This formulation of the reciprocity principle for the solutions to parabolic equations exactly repeats the well-known result (see [3, Section 4.2]) for the solutions to the wave equation. In particular, from (7) and the above expression for Q, it follows that in the parabolic approximation under consideration, as in the case of true sound fields, the acoustic pressure is invariant with respect to a rearrangement of the receiver and the volume-velocity point source. The vibrational-velocity projection to the force-action direction is invariant with respect to the rearrangement of the extraneous-force source.

The validity of the energy conservation law for the solutions to parabolic equation (3) in the case of $\mathrm{Im}\,k^2 = 0$ can be found similarly. This conclusion differs from that mentioned above by using the complex conjugation p^* of the field under consideration instead of p_2 and leads to the following result:

$$\frac{\partial J}{\partial x} = 0,\ J = \frac{k_0}{2\omega}\int\int dydz\rho^{-1}\left|\Phi_2(\hat{S})p(x)\right|^2. \quad (8)$$

Here, J represents the energy flux through the waveguide cross section x = const. In the regular segment of a three-dimensional waveguide with cylindrical boundaries, the contributions of normal waves into J are additive by virtue of the orthogonality of modes. In the case of an isolated propagating mode, J (8) differs from the true acoustic-energy flux only by the replacement of the propagation constant $\xi_{n,m}$ by $\Phi_2^2(\xi_{n,m}^2/k_0^2 - 1)$. As in the two-dimensional case [8], parabolic equation (3) leads to a positive energy flux in the nonpropagating (supercritical) modes, where $\xi_{n,m}^2 < 0$, for $\Phi_N(a^*) = [\Phi_N(a)]^*$. The elimination of this deficiency requires using the approximations $\Phi_N(a)$ with complex coefficients for the radicals $(1 + a)^{1/2N}$. The consideration of such approximations is beyond the scope of this study. We note only that, for parabolic equation (3), (5) with complex coefficients, the above reciprocity relationships and their derivation remain valid, including for the case of an absorbing medium.

For estimating the principal phase-error term accumulated with distance and introduced by the parabolic

approximation, it will suffice to compare the solutions to the wave equation and parabolic equation in a layered medium (see [3, Section 7.6]). In the wave zone of a source, we use the saddle-point method (see [3, Appendix A]) for calculating the integral in (4). Let $\Phi_N(a) = (1 + a)^{1/2N} + O(a^{m_n})$ and $m_1 \geq 2$. In this case, the exponent in (4) has a stationary point

$$q_s = \xi_n \sin\varphi[1 + O(b^{m_1})],\ b = \chi_n^2 + \varphi^2,$$
$$\chi_n = \arccos\frac{\xi_n}{k_0},\ \varphi = \arctan\frac{y - y_0}{x - x_0}. \quad (9)$$

Here, χ_n is the glancing angle formed by the wave vector of a mode with the *xy* plane; the azimuth angle ϕ characterizes the deviation of the direction to the receiver from the *Ox*-axis, i.e., from the chosen preferential direction of the wave propagation. Calculating the contribution of stationary point (9) into integral (4) and comparing the result with the true field mode, we find that the parabolic approximation introduces the relative error $O(b^{m_1})$ into the phase and $O(b^{m_1} + b^{m_2})$ into the amplitude of the mode. For applicability of the parabolic approximation, ϕ and χ_n must be small. However, quantitative limitations for these angles rapidly weaken with the growth in the accuracy of the approximations of Φ_N used in parabolic equation (3). The distances to a source and the frequencies for which the parabolic equation can be used are bounded from above by the condition of correct reproduction of mode phases:

$$k_0(x - x_0)(\chi^2 + \phi^2)^{m_1} \ll 1, \quad (10)$$

where χ is the characteristic value of χ_n for the modes contributing substantially into the field. Note that, according to (10), in the applicability domain of the parabolic approximation, the field can undergo strong variations in the transverse directions *y* and *z* including the mode-phase deviations from its value at $y = 0$ for *x*, $z = \text{const}$, which are large compared to unity.

In contrast to the two-dimensional case [8], the amplitude error in the three-dimensional problem depends not only on the accuracy of the approximation provided by the function Φ_2 but also on Φ_1. The above estimates of the phase error for $\phi = 0$ coincide with earlier estimates for the two-dimensional waveguide [8]. (It is easy to show that the last estimates are also valid for the three-dimensional waveguide with cylindrical boundaries.) As applied to the horizontally heterogeneous media, the values of ϕ in criterion (10) are bounded from below by the angle of horizontal refraction. In the case when the sound propagates in ocean or atmosphere, this angle is, as a rule, much smaller than the grazing angles, and the horizontal refraction does not practically manifest itself at the frequencies and distances for which it is rightful to use parabolic equation (3), (5). Two-dimensional wide-angle parabolic equations used nowadays provide a high phase accuracy for the grazing angles $\chi \leq \beta$, where β amounts to at least one-half of radian [9–12]. The usage of the same approximations Φ_1 in three-dimensional parabolic equation (3) guarantees the phase accuracy for the azimuth angles $-\beta \leq \phi \leq \beta$. If the field is required to be calculated within a still wider range of azimuth angles, then to fulfill (10) and to cover the entire range, it may be necessary to solve several parabolic equations (3), (5) differing by the choice of the direction for the *Ox*-axis.

In the three-dimensionally heterogeneous medium, the asymptotic errors in the parabolic approximation can be estimated by comparing the high-frequency solutions to the wave equation and to the parabolic equation. Restricting ourselves to consideration of the fields far from the caustics, we present the solutions in the form of the ray (Debye) expansions $p = \exp(ik_0\theta(x))A(x, k_0)$, where k_0 serves as a formal large parameter and $A(x, k_0) = A_0(x) + (ik_0)^{-1}A_1(x) + \ldots$. Using the method of mathematical induction with respect to $M = 1, 2, \ldots$, it is easy to establish the validity of the identity

$$\hat{S}^M(Ae^{ik_0\theta}) = Ae^{ik_0\theta}\alpha^M\left\{1 + \frac{iM}{k_0\alpha}\left[\mathbf{v}_\perp\nabla\ln\frac{A^2}{\rho}\right.\right.$$
$$\left.\left. + \nabla\mathbf{v}_\perp + (M-1)\mathbf{v}_\perp\nabla\ln\alpha\right] + O(k_0^{-2})\right\}, \quad (11)$$
$$\mathbf{v} = \nabla\theta = (\nu_1, \mathbf{v}_\perp),\quad \mathbf{v}_\perp = (0, \nu_2, \nu_3),$$
$$\alpha = 1 - n^2 - \mathbf{v}_\perp^2 \text{ and } n^2 = k^2/k_0^2.$$

For an arbitrary analytical function Φ, expanding $\Phi(\hat{S})$ in terms of $\hat{S}$, we obtain from (11)

$$\Phi(\hat{S})Ae^{ik_0\theta} = Ae^{ik_0\theta}\left\{\Phi(\alpha) + \frac{i}{k_0}\left[\nabla(\mathbf{v}_\perp\Phi'(\alpha))\right.\right.$$
$$\left.\left. + \Phi'(\alpha)\mathbf{v}_\perp\nabla\ln\frac{A_0^2}{\rho}\right] + O(k_0^{-2})\right\}. \quad (12)$$

Substituting the Debye expansion into (3) and using (11) and (12), we obtain in the major order with respect to k_0 that $\nu_1 = \Phi_1(\alpha)$, i.e., the eikonal equation in the parabolic approximation. Introducing the Hamiltonian

$$H(x, \mathbf{v}) = 0.5[\Psi(\nu_1) - n^2 + 1 + \mathbf{v}_\perp^2] \quad (13)$$

allows reducing the solution of the eikonal equation to the solution of the Hamiltonian ray equations

$$\frac{d\mathbf{x}}{d\tau} = \boldsymbol{\eta} \equiv (\mu, \mathbf{v}_\perp),$$
$$\mu = [2\Phi_1'(\alpha)]^{-1};\ \frac{d\mathbf{v}}{d\tau} = 0.5\nabla n^2. \quad (14)$$

Here, the parameter τ describes the position of a point under consideration at the ray, $\Psi(\nu_1)$ is the function inverse to $\Phi_1(a)$. The equations of true rays (see [3, Section 5.1]) differ from (14) in the replacement of $\boldsymbol{\eta}$ by $\boldsymbol{\nu}$.

According to (14) in the parabolic approximation, the fluid turns out to be an acoustically anisotropic medium, and the directions of the normal $\boldsymbol{\nu}$ to the wave front and of the ray tangent $\boldsymbol{\eta}$ do not coincide. The anisotropy and differences between rays and eikonals corresponding to the wave equation and the parabolic equation tend to zero with increasing the accuracy of the approximation of $\boldsymbol{\Phi}_1$. It should be emphasized that parabolic equation (3) completely describes the three-dimensional refraction. In the limit, $\boldsymbol{\Phi}_1(a) \longrightarrow (1 + a)^{1/2}$, H (13) transforms into the known Hamiltonian $H = 0.5(\boldsymbol{\nu}^2 - n^2)$ for solutions to the wave equation (see [3, Section 5.1]), and, according to (14), $\boldsymbol{\eta} = \boldsymbol{\nu}$.

Similarly to the derivation of the eikonal equation, substituting the Debye expansion into (3) and equating the terms not containing k_0 with the help of (12) and (14), we obtain the transport equation

$$\frac{d}{d\tau}\ln\left(\frac{A_0^2}{\mu\rho}\Phi_2^2(\alpha)\right) + \nabla\left(\frac{dx}{d\tau}\right) = 0, \qquad (15)$$

which allows us to calculate an amplitude of the ray field. This equation differs from the corresponding result following from the wave equation only by the presence under the logarithm of an additional factor Φ_2^2/μ. A physical meaning of the transport equation consists in the fact (see [3, Section 5.1]) that, in the ray tube, the energy flux is conserved, its density being equal to $k_0 A_0^2\, \Phi_2^2/\omega\rho\mu$ in the case under consideration. The local energy-conservation law for the high-frequency sound can be also found directly from the parabolic equation while ignoring the consideration of the ray geometry. Indeed, multiplying parabolic equation (3) by $\rho^{-1/2}\Phi_2(\hat{S})p^*$ and using (12) for simplifying the real part of the product, it is easy to obtain

$$\nabla I = 0,$$
$$I = (\omega\rho\mu)^{-1}k_0|p|^2\Phi_2^2(\alpha)\eta[1 + O(k_0^{-1})]. \qquad (16)$$

It is also easy to verify that expression (16) for the density of the energy-flux in high-frequency waves agrees with exact integral relationship (6).

We compare the high-frequency solutions to energy-conserving parabolic equation (3) and to the traditional parabolic equation

$$\frac{\partial p}{\partial x} = ik_0\Phi_1(\hat{S})p, \qquad (17)$$

whose coefficients involve no derivatives of medium parameters with respect to x. When the same approximation Φ_1 for the square root of the operator is used in (3) and (17), both parabolic equations lead to the same eikonal equation but to different transport equations. It follows from (17) that

$$\frac{d}{d\tau}\ln\left(\frac{A_0^2}{\mu\rho}\right) + \nabla\left(\frac{d\mathbf{x}}{d\tau}\right) = -\mu\frac{\partial}{\partial x}\ln\rho. \qquad (18)$$

If the medium density varies along the propagation direction, the right-hand side in (18) differs from zero, and the energy flux in the ray tube is not conserved. When $\rho_x \equiv 0$, equation (18) expresses the conservation of a certain energy quantity, but its values corresponding to these two parabolic equations differ. This fact leads to a difference in the amplitude errors. For simplicity, let the error in the approximation of Φ_1 be negligible, so that we can ignore the difference in the geometry of rays corresponding to the parabolic equation and the wave equation. In this case, the amplitude of the solution to parabolic equation (17) differs for $\rho_x \equiv 0$ from the ray amplitude of the solution to the wave equation by the factor $[\mu(\tau_2)/\mu(\tau_1)]^{-1/2} = 1 + O(b)$, where τ_1 and τ_2 correspond to the point of a position of the source and receiver, respectively. According to (15), in the case of an arbitrary ρ_x, the deviation of the ray amplitudes for parabolic equation (3) amounts to

$$\left[\frac{\mu(\tau_2)\Phi_2^2(\tau_2)}{\mu(\tau_1)\Phi_2^2(\tau_2)}\right]^{-1/2} = 1 + O(b^{m_1} + b^{m_2}).$$

Therefore, the amplitude error in parabolic equation (3), in contrast to (17), tends to zero with an increase in the accuracy of approximations of $\Phi_{1,2}$.

Thus, the usage of parabolic equation (3), (5) proposed in this study instead of traditional parabolic equation (17) enables us to improve the accuracy in the calculating amplitude without reducing that of the phase and to provide the energy conservation and the exact validity of the reciprocity principle in simulating the sound fields in three-dimensional heterogeneous media.

ACKNOWLEDGMENTS

Studies underlying this paper were carried out in the Institute of Oceanology of the RAS under the partial support of the Russian Foundation for Basic Research, as well as of INTAS, the INTAS–RFBR project no. 95-1002, and in the University of Victoria, B.C., Canada) under the support of NSERC.

REFERENCES

1. F. D. Tappert, in *Propagation of the Waves and Underwater Acoustics*, Ed. by R. Keller and A. Papadakis (Springer, Heidelberg, 1977; Mir, Moscow, 1980), pp. 180–226.
2. S. M. Rytov, Yu. A. Kravtsov, and V. I. Tatarskiĭ, *Introduction to Statistical Radio Physics* (Nauka, Moscow, 1978).

3. L. M. Brekhovskikh and O. A. Godin, *Acoustics of Layered Medium*, Vol. 2: *Point Sources and Bounded Beams* (Nauka, Moscow, 1989; Springer, Berlin, 1999).
4. L. Nghiem-Phu and F. D. Tappert, J. Acoust. Soc. Am. **78** (1), 164 (1985).
5. F. B. Jensen, W. A. Kuperman, M. B. Porter, and H. Schmidt, in *Computational Ocean Acoustics* (AIP, New York, 1993), Chap. 6.
6. O. A. Godin, D. Yu. Mikhin, and A. V. Mokhov, Akust. Zh. **42**, 501 (1996) [Acoust. Phys. **42**, 441 (1996)].
7. O. A. Godin, Dokl. Akad. Nauk **361**, 329 (1998) [Dokl. Phys. **43**, 393 (1998)].
8. O. A. Godin, Wave Motion **29**, 175 (1999).
9. K. V. Avilov, in *Acoustics of Ocean Medium* (Nauka, Moscow, 1989), pp. 10–19.
10. M. D. Collins, J. Acoust. Soc. Am. **92**, 2069 (1992).
11. M. D. Collins, R. J. Cederberg, D. B. King, *et al.*, J. Acoust. Soc. Am. **100** (1), 178 (1996).
12. D. Lee and A. D. Pierce, J. Comput. Acoust. **3** (2), 95 (1995).
13. D. Yu. Mikhin, in *Proceedings of the IV European Conference on Underwater Acoustics, 1998* (CNR-IDAC, Rome, 1998), pp. 679–684.
14. D. Yevick, C. Rolland, and B. Hermansson, Electron. Lett. **25** (18), 1254 (1989).
15. D. Lee and M. H. Schultz, *Numerical Ocean Acoustic Propagation in Three Dimensions* (World Scientific, Singapore, 1995).

Translated by V. Bukhanov

Doklady Physics, Vol. 45, No. 8, 2000, pp. 372–375. Translated from Doklady Akademii Nauk, Vol. 373, No. 5, 2000, pp. 611–614.

PHYSICS

Generalized Equation for Inverse Population in a Laser Active Medium

Academician A. L. Mikaelyan and Yu. G. Turkov

Received March 28, 2000

Usually, equations describing the evolution of the inverse population in laser theory are valid only for idealized energy levels of an active medium.

Allowing for the actual structure of energy levels in a laser material necessitates the consideration of a system of differential equations describing the evolution of the population of all levels playing a significant role in the process of laser generation. Such an approach requires solving a system of equations of a high order, which is possible only by numerical computer simulation.

In addition, in this approach, certain difficulties appear associated with the lack of complete information on corresponding spectroscopy constants of a material, which, as a rule, are known with an acceptable accuracy only for a rather limited number of energy states.

Nevertheless, as is shown below, under certain simplifications, allowance for the actual structure of the energy levels of a laser material can be realized in a fairly simple manner. In this case, a system of high-order differential equations can be reduced to only one equation. It has the meaning of an equation for the inverse population density and generalizes well-known equations for three- and four-level active media.

The simplified assumptions mentioned above are associated with the possibility to isolate separate groups of energy levels closely related to each other. The energy exchange processes between these levels lead to the rapid establishment of thermodynamic equilibrium.

In this case, it is natural that the admissible rate of establishing the thermodynamic equilibrium, for which we consider the energy levels to be closely bound with each other, is defined by the speed of proceeding processes of the laser generation. For example, in different situations, the same levels may be considered to be either strongly bound in the continuous laser-generation mode or isolated in the energy sense while generating short pulses.

When considering processes of generation and amplification of laser radiation, it is reasonable to isolate groups of levels to which the upper and lower levels of the laser transition belong.

The diagram of the energy levels for a certain active laser medium is presented in Fig. 1. We assume that a laser transition takes place between the *j*th level of the level group *2* and an *i*th level of the level group *1* (rigorously speaking, the subscripts *i* and *j* should be denoted by a combination of two numbers, namely, 1, *i* and 2, *j*, where the former implies belonging to a corresponding group (1 or 2)). Thus, $i = 1_1, 1_2, 1_3, \ldots$; and $j = 2_1, 2_2, 2_3, \ldots$). We assume also that the distribution of the level populations within each group always corresponds to the thermodynamic equilibrium. Then, we may write out

$$n_i = \gamma_i n_1, \quad n_j = \gamma_j n_2, \tag{1}$$

where n_1 and n_2 are the total number of atoms occupying all energy levels belonging to the groups 1 or 2, respectively, i.e., the populations of these groups.

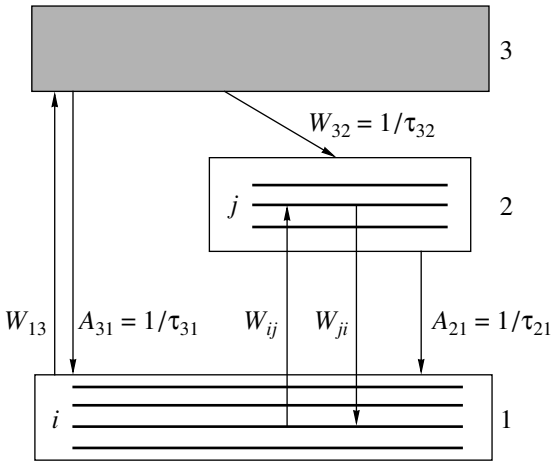

Fig. 1.

Institute of Optoneyral Technologies,
Russian Academy of Sciences,
ul. Vavilova 44/2, Moscow, 117333 Russia

1028-3358/00/4508-0372$20.00

The coefficients γ_i and γ_j are easily determined from the Boltzmann distribution for the population:

$$\gamma_i = \frac{g_i e^{-\frac{E_i - E_{10}}{kT}}}{\sum_i g_i e^{-\frac{E_i - E_{10}}{kT}}}, \quad \gamma_j = \frac{g_j e^{-\frac{E_j - E_{20}}{kT}}}{\sum_j g_j e^{-\frac{E_j - E_{20}}{kT}}}. \tag{2}$$

Here, E_i and E_j are the energies of the levels i and j, respectively; E_{10} and E_{20} are the energies of lower levels in the groups 1 and 2, respectively; g_i and g_j are the degeneracy multiplicities for the levels i and j, respectively; k is the Boltzmann constant; and T is temperature of an active medium.

It is worth noting that the energy scheme under consideration generalizes the level schemes for both three- and four-level active medium under the condition of a rapid relaxation of the lower laser level. In this case, this level may be included in the group 1 of levels being in the thermodynamic equilibrium with the ground level.

For the scheme under consideration, the system of equations describing the evolution for the populations of the level groups 1, 2, and 3 takes the form

$$\frac{dn_1}{dt} = W_{ji}\gamma_j n_2 - W_{ij}\gamma_i n_1 - W_{13}(n_1 - n_3) + \frac{n_2}{\tau_{21}} + \frac{n_3}{\tau_{31}}, \tag{3}$$

$$\frac{dn_2}{dt} = -W_{ji}\gamma_j n_2 + W_{ij}\gamma_i n_1 + \frac{n_3}{\tau_{32}} - \frac{n_2}{\tau_{21}}, \tag{4}$$

$$\frac{dn_3}{dt} = W_{13}(n_1 - n_3) - \frac{n_3}{\tau_{32}} - \frac{n_3}{\tau_{31}}, \tag{5}$$

where W_{ij} and W_{ji} are the induced-transition probabilities bound with each other by the relation

$$g_i W_{ij} = g_j W_{ji}.$$

The lifetimes and excitation probabilities of the active atoms under the action of pumping, which are involved into equations (3)–(5), determine the effective rates of the energy exchange between the isolated level groups.

As is seen, the entire difference between equations (3)–(5) and usual ones applied to an ideal active laser medium (see, e.g., [1]) lies in the fact that the probabilities W_{21} and W_{12} are replaced by the quantities $\gamma_j W_{ji}$ and $\gamma_i W_{ij}$, respectively, which represent effective values for the corresponding transition probabilities. Hence, introducing the notation

$$W_{21\text{eff}} = g_j W_{ji}, \quad W_{12\text{eff}} = g_i W_{ij} \tag{6}$$

or, which is the same, a similar notation for effective values of the transition cross sections

$$\sigma_{21\text{eff}} = g_j \sigma_{ji}, \quad \sigma_{12\text{eff}} = g_i \sigma_{ij}, \tag{7}$$

we formally arrive again at the equations for the idealized three-level medium including the equation for inverse population density. There is only one distinction between them. The parameter g_2/g_1 involved in this equation is replaced by a more general parameter

$$G = \frac{W_{12\text{eff}}}{W_{21\text{eff}}} = \frac{\sigma_{12\text{eff}}}{\sigma_{21\text{eff}}} = \frac{\gamma_i g_j}{\gamma_j g_i}. \tag{8}$$

Indeed, assuming that active atoms are not accumulated on the levels of the group 3, i.e., $n_3 \ll n_1$ and $\frac{dn_3}{dt} = 0$, we have from Eq. (5)

$$n_3 = W_{13}\frac{\tau_{31}}{\tau_{31} + \tau_{32}}\tau_{32} n_1. \tag{9}$$

Substituting this relationship into (3) and (4), we obtain

$$\begin{aligned} \frac{d\Delta}{dt} &= -(1 + G)\Delta W_{21\text{eff}} \\ &+ n_0\left(W_\text{p} - \frac{G}{\tau_{21}}\right) - \Delta\left(W_\text{p} + \frac{1}{\tau_{21}}\right), \end{aligned} \tag{10}$$

where

$$\Delta = n_2 - G n_1 \tag{11}$$

is the generalized inverse population density introduced instead of the generally accepted quantity $n_2 - \frac{g_2}{g_1} n_1$;

$$W_\text{p} = W_{13}\frac{\tau_{31}}{\tau_{31} + \tau_{32}} \tag{12}$$

is the effective value of the excitation probability for an active atom under the action of pumping; and n_0 is the total number of active atoms per unit volume.

At $G = 1$, equation (10) transforms into that for the three-level active medium; at $G = 0$, it transforms into that for the four-level medium with the vacant low level of the laser transition.

The gain of the active medium with the generalized scheme of the energy levels is

$$\alpha = \sigma_{ji} n_j - \sigma_{ij} n_i = \sigma_{ji}\gamma_j n_2 - \sigma_{ij}\gamma_i n_1 = \sigma_{21\text{eff}}\Delta. \tag{13}$$

When the contribution to the gain of several closely lying laser lines must be taken into account, the effective cross sections of the induced transition should be introduced in the form

$$\sigma_{21\text{eff}}(\nu) = \sum_{ij}\sigma_{ji}(\nu)\gamma_j, \quad \sigma_{12\text{eff}}(\nu) = \sum_{ij}\sigma_{ij}(\nu)\gamma_i. \tag{14}$$

In this case, as before, the parameter G in Eq. (10) is determined by the relation $\sigma_{12\text{eff}}/\sigma_{21\text{eff}}$.

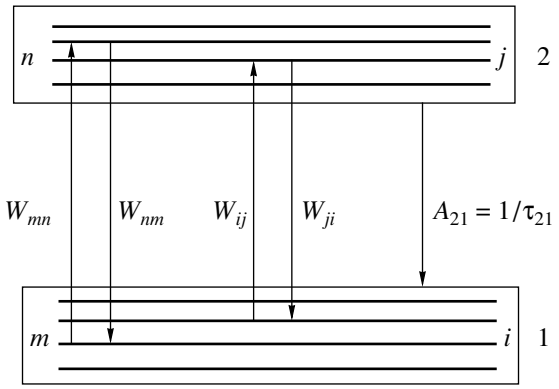

Fig. 2.

If the level 3 is situated closely to the upper laser level (as this takes place for the semiconductor pumping of YAG:Nd-laser), then its equilibrium Boltzmann population should be taken into account. With this purpose, this level may be included into the level group 2 tightly bound with the upper level of the laser transition. The energy diagram depicted in Fig. 2 assumes that the excitation of the active medium is attained owing to the atom transitions from the level m of the group 1 to the level n of the group 2, and the laser generation corresponds to the same transition between levels j and i. In this case, performing calculations similar to those used while deriving (10), we arrive at the following equation for the generalized density of the inverse population:

$$\frac{d\Delta}{dt} = -(1+G)\Delta W_{21\text{eff}} + n_0\left[W_\text{p}(1-G_\text{p}G) - \frac{G}{\tau_{21}}\right] - \Delta\left[W_\text{p}(1+G_\text{p}) + \frac{1}{\tau_{21}}\right]. \quad (15)$$

Here, Δ, G, and $W_{21\text{eff}}$ are, as before, expressed by the same formulas (11), (8), and (6);

$$G_\text{p} = \frac{\sigma_{nm\,\text{eff}}}{\sigma_{mn\,\text{eff}}} = \frac{\gamma_n g_m}{\gamma_m g_n}, \quad (16)$$

and $W_\text{p} = \gamma_m W_{mn}$ is the effective probability for excitation of an atom under the action of pumping radiation. The quantities γ_n, γ_m, g_n, g_m have the same meaning as the corresponding quantities for the levels i and j.

In a certain sense, we can say that Eq. (15) describes the evolution of the inverse population in a quasi-two-level laser. In particular, it follows from this equation that the inequality $G_\text{p}G < 1$ is the necessary condition for the existence of the inversion ($\Delta > 0$) in the steady-state mode of such a laser. It is easy to show that this condition is equivalent to the well-known relation

$$E_n - E_m > E_j - E_i;$$

i.e., the frequency of pumping radiation must exceed the frequency of the laser radiation.

It is worth noting that Eq. (15) is easily generalized for the case when several lines with a close frequency lines play the role. The parameters G and G_p represent the ratios of the corresponding effective cross sections determined by summation over all lines similarly to [14].

At $G_\text{p} = 0$, Eq. (15) transforms into (10).

Equations derived enable us to easily perform calculations of solid-state lasers with an allowance for the actual structure of energy levels and the active medium temperature determining the values of the coefficients γ in accordance with formulas (2). For a more convenient application of these equations in practice, it would be desirable to form information tables for the temperature dependences of the coefficients γ and parameters G and G_p of the basic spectral lines for laser crystals.

As an example, we demonstrate the advantage of the approach proposed in calculating the output power of the solid-state laser operating in the steady-state mode. Using Eq. (10), it is not difficult to obtain the generalized formula for the output power in the form

$$P_\Sigma = \frac{h\nu n_0 V \ln\frac{1}{r}}{(1+G)\tau_{21}(2\beta l - \ln r)} \times\left[k - G - (k+1)\frac{2\beta l - \ln r}{2\sigma_{21\text{eff}} n_0 l}\right]. \quad (17)$$

Here,

$$k = W_\text{p}\tau_{21},$$

$h\nu$ is the energy of photons for the laser generation; V and l are the volume and the length of an active sample, respectively; r is the reflection factor of the output mirror in the optical resonator (the second mirror is assumed to be ideally reflecting); and β is the nonresonance loss in the crystal. In the particular cases of $G = 1$ and $G = 0$, this formula transforms into well-known expressions for the output power of three- and four-level lasers [1].

When the evolution of the inverse population obeys Eq. (15), the formula for the output power of a continuous-wave laser has the form

$$P_\Sigma = \frac{h\nu n_0 V \ln\frac{1}{r}}{(1+G)\tau_{21}(2\beta l - \ln r)} \times\left[k - G - (k+1)\frac{2\beta l - \ln r}{2\sigma_{21\text{eff}} n_0 l} - kG_\text{p}\left(G + \frac{2\beta l - \ln r}{2\sigma_{21\text{eff}} n_0 l}\right)\right]. \quad (18)$$

The last term in this formula determines the decrease of the generation power caused by the finite population density for the upper level of the transition

used for laser optical pumping as well as by the presence of several levels in a group to which the lower level of this transition belongs. For $G_p = 0$, formula (18) takes the form of (17).

To illustrate, we consider a ruby laser [1]. In a ruby crystal, two twofold degenerate metastable levels $\bar{E}$ and $2\bar{A}$ separated by the distance 29 cm^{-1} should be related to the level group 2. The laser transition takes place from the lower of these levels $\bar{E}$ (R_1 line) or from the upper $2\bar{A}$ level (R_2 line) onto the $^4A_2$ ground level degenerated fourfold, which is unique in the level group 1 (as a rule, laser generation takes place for the stronger R_1 line). The values of the parameter G for the R_1 and R_2 lines of the laser transition in a ruby crystal, evaluated by formulas (8) and (2), are given here for the temperature range between 50 and 450 K.

T, K	50	100	150	200	250	300	350	400	450
G (R_1 line)	0.717	0.829	0.879	0.906	0.923	0.935	0.944	0.950	0.956
G (R_2 line)	1.652	1.259	1.160	1.116	1.091	1.075	1.063	1.055	1.049

As is seen, when applied to a ruby laser, the usually used three-level approximation ($G = 1$) is fairly accurate at room and higher temperature. However, to investigate a laser operating at lower temperatures, as well as in the case when we need comparative analysis of ruby laser characteristics for the R_1 and R_2 lines, it is necessary to take into account actual values and temperature dependences of the parameters G for these lines.

In conclusion, we present a relationship useful for practice, which concerns continuous–wave four-level lasers. This relationship interrelates the differential energy efficiency (i.e., the linear part of the ratio for the generation power to the increment of the pumping power) and the threshold pumping power. It is evident that both characteristics are determined in the same degree by the efficiency of the pumping system; therefore, their values must be interrelated. The relationship mentioned above is easily derived from formula (17) at $G = 0$ and with an allowance for the fact that the product of the differential energy efficiency of the laser by the threshold pumping power is numerically equal to the output generation power at the double excess of the threshold. This product has the form

$$P_{th}\eta_{diff} = \frac{h\nu V \ln\frac{1}{r}}{2\tau_{21}\sigma_{21eff}l}, \qquad (19)$$

where P_{th} is the threshold pumping power and η_{diff} is the differential laser efficiency.

In particular, for a YAG laser (assuming $h\nu = 1.87 \times 10^{-19}$ J, $\sigma_{21eff} = 3.4 \times 10^{-19}$ cm^2, $\tau_{21} = 240$ μs, $V = 1$ cm^3, $l = 5$ cm, and $r = 0.9$), we obtain $P_{th}\eta_{diff} = 24$ W. For example, in the case of the threshold pumping power of 1000 W, the differential energy laser efficiency is equal to 2.4%.

REFERENCE

1. A. L. Mikaelyan, M. L. Ter-Mikaelyan, and Yu. G. Turkov, *Solid-State Lasers* (Sovetskoe Radio, Moscow, 1967).

Translated by Yu. Vishnyakov

Doklady Physics, Vol. 45, No. 8, 2000, pp. 376–379. Translated from Doklady Akademii Nauk, Vol. 373, No. 6, 2000, pp. 746–749.

PHYSICS

Self-Organization Processes in a System of Magnetic Moments in Polycrystals

V. K. Karpasyuk and E. I. Beznisko

Presented by Academician Yu.V. Gulyaev December 20, 1999

Received December 21, 1999

The processes of evolution and self-organization in nonlinear dissipative physical systems including those characteristic of magnetic microstructure in solids are currently attracting a considerable amount of interest. The self-organization phenomena in garnet ferrite films with perpendicular anisotropy have received the most study [1, 2]. The problem of self-organized criticality arising in polycrystals in the course of their demagnetization is widely debated [3, 4]. The basic factor determining the transition between two different ordered states of the domain structure is the long-range magnetodipole interaction. It is quite difficult to take proper account of this interaction in real materials, and this sends us to address the analysis of the simplest models [5]. The most complicated problem concerns a theoretical description of self-organization in a three-dimensional system of domains.

So far, only the spatial distribution of magnetization was considered in the analysis of self-organization processes. In this paper, we study the evolution of angular distribution of magnetic moments in polycrystalline ferrites under the effect of a pulsed magnetic field. We consider the ferrites with cubic crystal lattice having the [111] axes of easy magnetization. The analysis is based on the solution of a nonlinear integro-differential equation derived here. The equation characterizes the dynamics of remagnetization processes in polycrystals and takes into account the interaction between grains, hysteresis, and saturation.

Following the model concepts put forward in [6], we assume that magnetic moments of grains are oriented along the easy magnetization axes closest to the direction of the applied field and are uniformly distributed within a cone with a linear opening angle $2\alpha_m$ [$\alpha_m = \arccos(1/\sqrt{3})$]. Each grain is characterized by a rectangular hysteresis loop, its magnetization stems from the motion of 180° domain walls.

Due to the misorientation of the crystallographic axes of neighboring grains, the normal magnetization component has discontinuities at the grain walls. These discontinuities give rise to the internal stray magnetic fields. The mean value of the stray field component along the easy magnetization axis of a grain directed at angle α with magnetization **J** of the polycrystal (parallel to applied field **H**) is determined by the formula [6]

$$H_M = b(J - M(\alpha)\cos\alpha)\cos\alpha, \tag{1}$$

where $b \sim 1$ is the parameter depending on the configuration of the grain surface and $M(\alpha)$ is the magnetization of the grain under study. The domain wall velocity is proportional to the effective field

$$H_{\text{eff}} = H\cos\alpha + H_M - sH_\omega, \tag{2}$$

if $|H\cos\alpha + H_M| > H_\omega$ and $H_{\text{eff}} \ll H_{\text{crit}}$, where H_ω is the threshold field of the wall displacement, $s = \text{sgn}(H\cos\alpha + H_M)$, and H_{crit} is the Walker critical field [7]. Under the above conditions, the variation rate of relative magnetization m in a spherical grain obeys the integro-differential equation

$$\frac{dm(\alpha, t)}{dt} = 3\Lambda(\alpha, t)(1 - x^2)[h(t)\cos\alpha - s + 2p^2(j(t) - m(\alpha, t)\cos\alpha)\cos\alpha]. \tag{3}$$

Here, $m = M/M_S$ (M_S is the saturation magnetization), $j = J/M_S$, $h = H/H_\omega$, $x = -2\cos((\pi + \arccos m)/3)$ is the boundary position normalized by the grain radius and measured with respect to the grain center ($-1 \le x \le 1$), and $p = [bM_S/(2H_\omega)]^{1/2}$ is the parameter characterizing the magnetodipole interaction between grains. The saturation and hysteresis are taken into account by parameter $\Lambda(\alpha, t)$:

$$\Lambda = 1, \text{ if } ((H_{\text{eff}} < 0) \wedge (-1 < m(\alpha, t) \le 1)) \vee \vee ((H_{\text{eff}} > 0) \wedge (-1 \le m(\alpha, t) < 1)), \tag{4}$$

otherwise $\Lambda = 0$.

Astrakhan State Pedagogical University,
ul. Tatishcheva 20a, Astrakhan, 414056 Russia

1028-3358/00/4508-0376$20.00

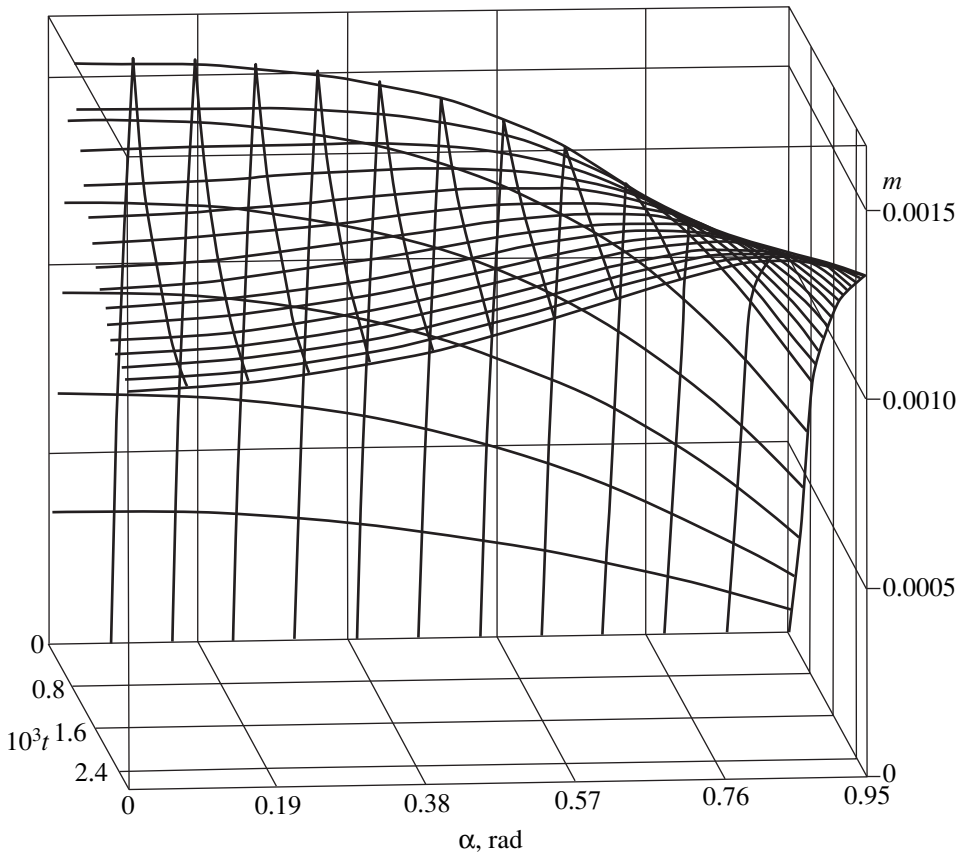

Fig. 1. Evolution of the angular distribution of grain magnetization $m(\alpha, t)$ under the effect of alternating-sign magnetic field pulses. The first pulse: amplitude $h_1 = 2$, duration $\tau_1 = 8 \times 10^{-4}$; subsequent pulses: $|h| = 2.5$, $\tau = 3 \times 10^{-5}$; the interval between pulses is $\tau_p = 10^{-5}$.

The relative magnetization of the polycrystal is a functional depending on $m(\alpha, t)$:

$$j(t) = (1 - \cos\alpha_m)^{-1} \int_0^{\alpha_m} m(\alpha, t) \cos\alpha \sin\alpha d\alpha. \quad (5)$$

We choose normalization of t in such a way that at $h = 2$ in the absence of intergrain interaction ($p = 0$), the time needed for magnetization of a grain with $\alpha = 0$ from the state $m(0, 0) = -1$ is equal to unity.

The integration of equation of motion (3) taking into account relationships (4) and (5) was performed by numerical methods for a discrete set of α values.

The time dependence of the angular distribution of the grain magnetic moments during magnetization of a polycrystal by the different series of rectangular field pulses $h(t)$ from the demagnetized state $[m(\alpha, 0) \equiv 0]$ at $p = 20$ are plotted in Figs. 1–3.

Under the effect of short alternating-sign pulses, the angular distribution of magnetization can be nonmonotonic with a peak and an inflection point (Figs. 1 and 2). Figure 1 demonstrates that, during the first (positive) pulse, the grains with $\alpha = 0$ have the maximum magnetization, and after the last (51th) pulse, their magnetization turns out to be minimal. If the amplitude of the applied field is close to threshold value H_ω, then after a fairly large number of pulses, the distribution ceases to respond to them and has a rather exotic form.

Under the effect of rather long and intense field pulses (see, for example, Fig. 3), the most rapid change at the initial stage is observed in the magnetization of grains with the small angles α (at not very high values of $|h|$, the domain walls with $\alpha \approx \alpha_m$ can initially be immobile). Then, magnetization rate for grains with the large α gradually increases (the larger is α, the faster is the growth). Finally, the angular distribution of magnetization tends to that shown in Fig. 4.

In conclusion, the magnetization of polycrystals is accompanied by self-organization related to the magnetodipole interaction of grains. The self-organization gives rise to the angular distributions of magnetic moments drastically different from those induced by the applied field alone. The proposed method for the analysis of the self-organization processes can be generalized by taking into account the statistics of forma-

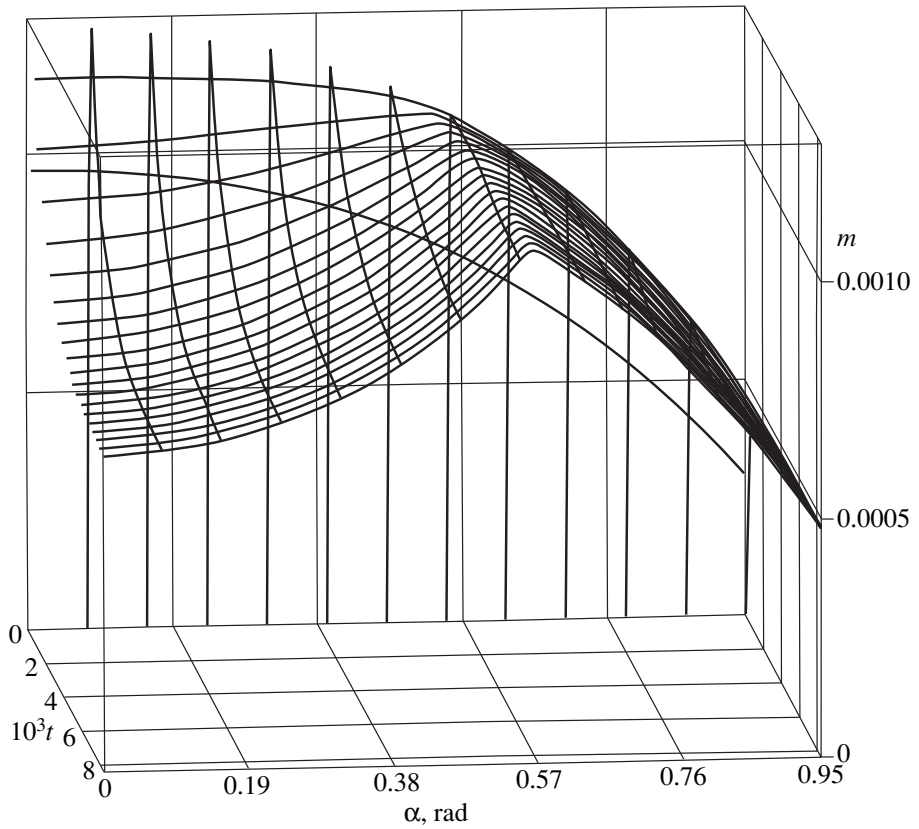

Fig. 2. $m(\alpha, t)$ curves under effect of the alternating-sign magnetic field pulses. The first pulse: $h_1 = 2$, $\tau_1 = 6 \times 10^{-4}$; the subsequent pulses: $|h| = 1$, $\tau = 9 \times 10^{-5}$; $\tau_p = 10^{-5}$.

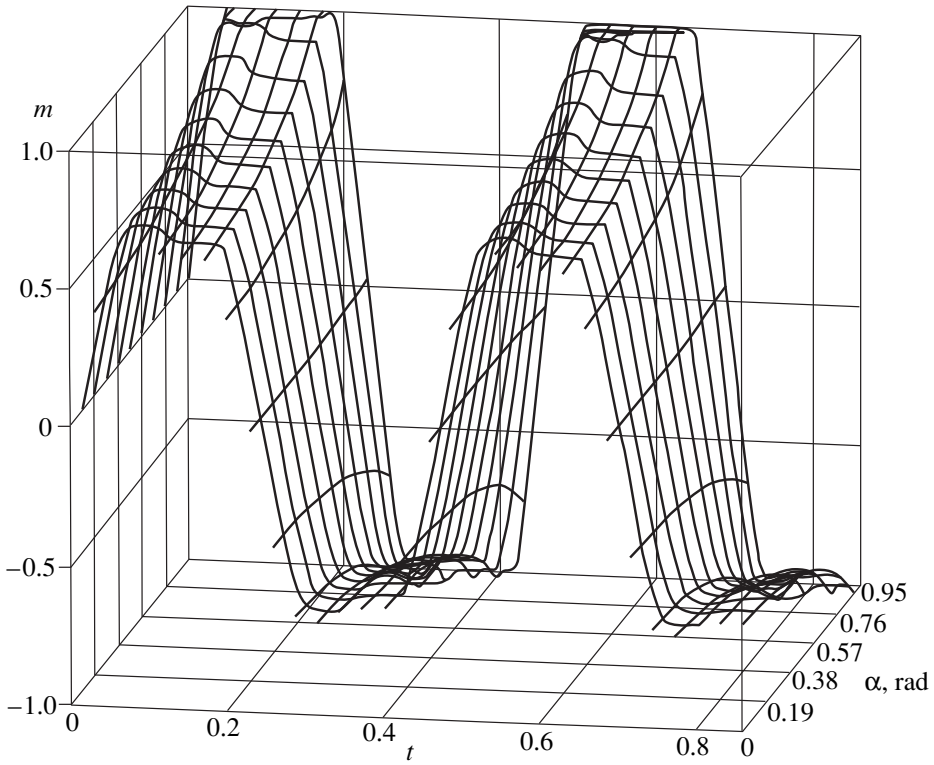

Fig. 3. $m(\alpha, t)$ under effect of the alternating-sign magnetic field pulses with amplitude $|h| = 10$ and durations: $\tau_1 = 0.1$, $\tau = 0.15$, and $\tau_p = 0.08$.

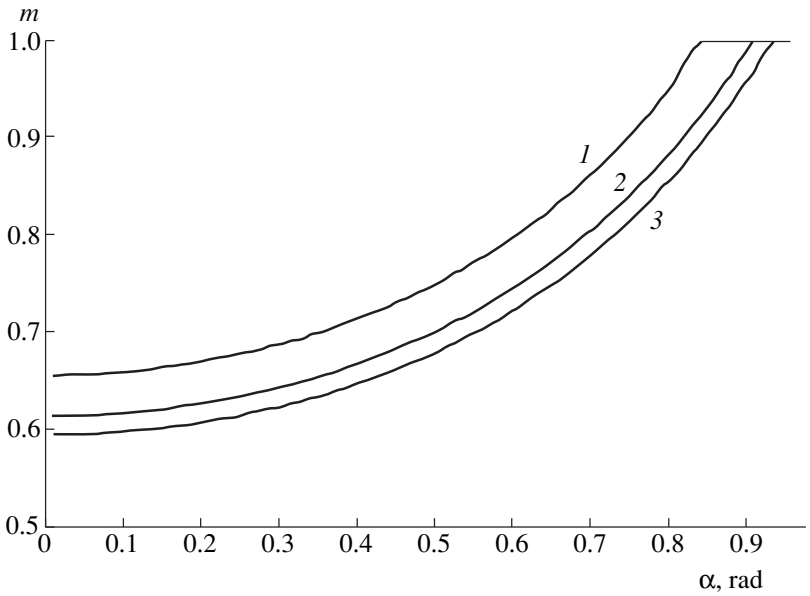

Fig. 4. The eventual angular dependence of grain magnetization in the remanent magnetization state of a polycrystal: (*1*) $p = 10$; (*2*) $p = 20$; (*3*) $p = 40$.

tion and annihilation of the domain walls, as well as the distribution in size and coercitivity of the grains.

REFERENCES

1. G. S. Kandaurova and A. A. Rusinov, Pis'ma Zh. Éksp. Teor. Fiz. **65**, 60 (1997) [JETP Lett. **65**, 63 (1997)].
2. F. V. Lisovskiĭ, E. G. Mansvetova, E. P. Nikolaeva, *et al*., Zh. Éksp. Teor. Fiz. **103**, 213 (1993) [JETP **76**, 116 (1993)].
3. O. A. Chubykalo and J. M. González, J. Appl. Phys. **83**, 7228 (1998).
4. O. A. Chubykalo, J. M. González, and J. Gonzalez, Physica D **113**, 382 (1998).
5. F. V. Lisovskiĭ and O. P. Polyakov, in *Proceedings of XVI International School–Seminar* (Moscow, Russia, 1998), Part 2, pp. 492–493.
6. V. K. Karpasyuk, V. N. Kiselev, G. N. Orlov, *et al*., in *Electromagnetic Properties and Nonstoichiometry of Ferrites with Rectangular Hysteresis Loops* (Nauka, Moscow, 1985), p. 149.
7. T. H. O'Dell, in *Ferromagnetodynamics: The Dynamics of Magnetic Bubbles, Domains, and Domain Walls* (MacMillan, New York, 1981; Mir, Moscow, 1983), p. 256.

Translated by Yu. Vishnyakov

Doklady Physics, Vol. 45, No. 8, 2000, pp. 380–383. Translated from Doklady Akademii Nauk, Vol. 373, No. 6, 2000, pp. 750–753.

PHYSICS

Phonon Spectra for Crystal Lattices of V, Cr, Mn, Fe, Co, Ni, and Cu

N. N. Sirota*, I. M. Sirota, T. M. Soshnina*, and T. D. Sokolovskiĭ*****

Presented by Academician O.A. Bannykh December 8, 1999

Received December 9, 1999

Lattice phonon spectra for 3*d* elements with a cubic structure (V, Cr, Mn, Fe, Co, Ni, and Cu) are calculated approximately using the Mie–Grüneisen potentials.

Calculations were performed based on the Born–Karman–De Launay–Blackman (BKDB) method [1–4]. The De Launay force constants α_{ij} and β_{ij}, as well as the Born–Karman coupling constants A_{ij}, were determined using the Mie–Grüneisen potentials

$$U = -\frac{a}{r^m} + \frac{b}{r^n}. \quad (1)$$

The De Launay force constants β_{ij} correspond to the first derivative of the binding energy $U(r)_j$ in the crystal lattice of element *j*. The derivative is represented as a function of the nearest neighbor interatomic distance r_1 normalized by radius r_{ij} of the *i*th coordination sphere:

$$\beta_{ij} = \frac{1}{r_{ij}}\left(\frac{\partial U(r)}{\partial r}\right)_{r_{ij}}. \quad (2)$$

The force constants α_{ij} are equal to the second derivative of the binding energy $U(r)_{ij}$ as a function of *r* [4, 5]:

$$\alpha_{ij} = \left(\frac{\partial^2 U(r)_j}{\partial r^2}\right)_{r_{ij}}. \quad (3)$$

The derivatives are taken at points r_{ij}, which correspond to the radius of the *i*th coordination sphere of element *j* ($i \le 4$).

The values of ratio $\frac{r_0}{r_i} = k$ are presented in Table 1. Here, $r_i \equiv r_0$ is the radius of the first coordination sphere and r_i is the radius of the *i*th sphere. The data in Table 1 correspond to crystal structures of A_1 and A_2 types with face-centered cubic (fcc) and body-centered cubic (bcc) unit cells, respectively. The values of coordination numbers z_i for each coordination sphere are also given in Table 1.

For crystal structures of the A_1 and A_2 types, the radii of the first coordination spheres are related to lattice constant *a* by expressions $r_{1(A_1)} = \frac{\alpha}{\sqrt{2}}$ and $r_{1(A_2)} = \frac{a\sqrt{3}}{2}$. Elastic moduli characterizing the rigidity of monatomic crystals belonging to the A_1 structural type are expressed in terms of the De Launay force constants [4]

$$\begin{aligned} ac_{11} &= 2\alpha_1 + 2\beta_1 + 4\alpha_3 + 12\alpha_3 + 12\beta_3 + 8\alpha_4 + 8\beta_4, \\ ac_{12} &= \alpha_1 - 5\beta_1 - 4\beta_2 + 6\alpha_3 - 30\beta_3 + 4\alpha_4 + 20\beta_4, \\ ac_{44} &= \alpha_1 + 3\beta_1 + 4\beta_2 + 6\alpha_3 + 18\beta_3 + 4\alpha_4 + 12\beta_4. \end{aligned} \quad (4)$$

Bulk moduli $B = -\frac{1}{V}\frac{\partial^2 U}{\partial V^2}$ characterizing the uniform compression depend on exponents *m* and *n* in the Mie–Grüneisen potential [7]:

$$B = -\frac{mn}{9}\frac{U_m}{V}. \quad (5)$$

The De Launay force constants α_{ij} and β_{ij} are expressed through equilibrium energy U_0 of atomization per unit volume and through distance $r_0 \equiv r_1$ between the nearest neighbor atoms (radius of the first coordination sphere) by the expressions as follows:

$$\alpha_{ij} = \frac{mn(m+1)}{n-m}\frac{U_0}{r_0^2}k^{m+2}\left[1 - \frac{n+1}{m+1}k^{n-m}\right], \quad (6)$$

$$\beta_{ij} = -\frac{mn}{n-m}\frac{U_0}{r_0^2}k^{m+2}[1 - k^{n-m}]. \quad (7)$$

Using expressions (6) and (7), we calculated the values of force constants α_{ij} and β_{ij} for the transition elements with Z = 23–29 at fixed values of exponents *m* and *n* specified in Table 2.

* *Moscow State University of Environmental Engineering, ul. Pryanishnikova 19, Moscow, 127550 Russia*

** *Institute of Control Sciences (Automation and Telemechanics), Russian Academy of Sciences, Profsoyuznaya ul. 65, Moscow, 117806 Russia*

*** *Institute of Solid State and Semiconductor Physics, Belarussian Academy of Sciences, ul. Brovki 17, Minsk, 220072 Belarus*

1028-3358/00/4508-0380$20.00

Table 1. Coordination numbers z_i, coefficients $k_i = r_0/r_i$ in four coordination spheres (I–IV) for A_1 and A_2 structural types

Type of structure	I		II		III		IV	
	z_i	k_i	z_i	k_i	z_i	k_i	z_i	k_i
A_1	12	1	6	0.7071	24	0.57736	12	0.5
A_2	8	1	6	0.8683	12	0.612	24	0.5222

Table 2. Binding energies U_m (kJ/mol), U_0 (kJ/cm^3), atomic volumes V (cm^3), lattice constants a (Å), nearest neighbor distances $r_0 \equiv r_1$ (Å), exponents m, n, force constants α_i, β_i of four coordination spheres (I–IV)

Z	Element	a	V	U_m	U_0	r_1	m	n
23	V	3.024	8.34	512.96	65.565	2.619	3.5	7
							4	7
24	Cr	2.8846	7.23	396.64	58.48	2.5	6	8
							6	10
25	Mn	3.863	7.38	279.073	38.0	2.731	5	7
26	Fe	2.8645	7.09	417.689	62.8	2.477	6	8
							6	10
27	Co	3.5441	6.62	495.094	68.452	2.506	3	7
							3.5	7
28	Ni	3.5238	6.59	423.84	68.56	2.492	3.5	7
29	Cu	3.6147	7.09	339.322		2.556	3.5	7

I		II		III		IV	
α_1	β_1	α_2	β_2	α_3	β_3	α_4	β_4
36318.33	0.0	1812.38	1861.16	−2141.39	573.60	−1070.80	261.27
41506.67	0.0	1404.34	2047.72	−2307.63	562.05	−1083.38	240.66
69576.03	0.0	−2413.87	2765.69	−2492.74	429.95	−874.68	139.95
86970.04	0.0	−5252.43	3031.74	−2344.59	369.49	−743.47	111.32
29180.49	0.0	−2579.29	644.83	−1040.13	208.03	−455.95	85.49
76139.21	0.0	−2641.57	3026.58	−2728.98	470.51	−957.19	153.15
95174.02	0.0	−5747.90	3317.72	−2565.76	404.35	−813.60	121.82
35250.89	0.0	−3115.80	1168.45	−1759.02	502.59	−963.89	258.19
41126.05	0.0	−3705.81	1227.44	−1907.59	489.07	−984.81	236.70
4216.73	0.0	−3795.08	1257.01	−1953.54	500.85	−1008.54	242.40
29773.50	0.0	−2682.85	888.62	−1381.01	354.06	−712.96	171.36

Exponents m and n in potential (1) for a large number of elements were determined and discussed by Fürth [8] based on available experimental data.

In our paper, the phonon spectra for crystal lattices of transition metal elements with Z = 23–29 are determined using the calculated De Launay force constants corresponding to four coordination spheres. The calculations were performed by the BKDB method based on the solution of a secular equation

$$\left|D(q) - Mw^2(L)\right| = 0, \tag{8}$$

where M is the atomic mass, L is the unit matrix, and $D(q)$ is the dynamical matrix depending on vector q.

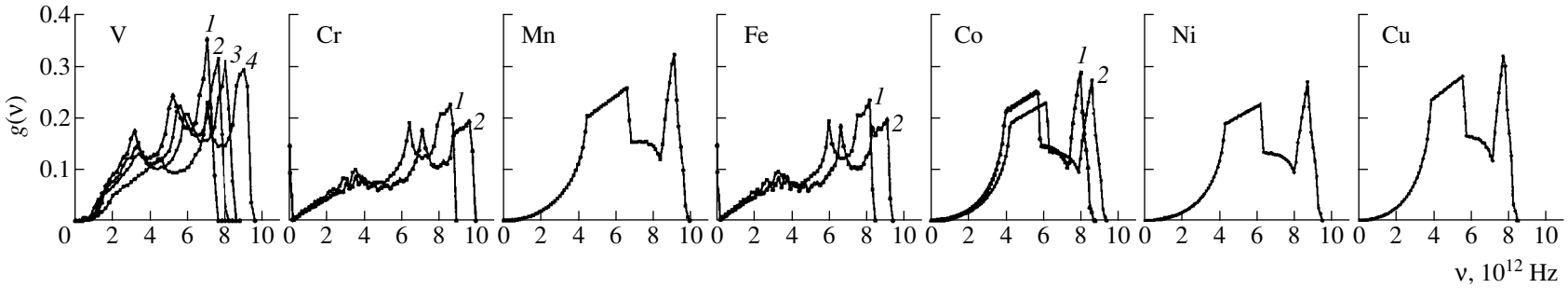

Fig. 1. Phonon spectra corresponding to the crystal lattices of elements with $Z = 23–29$ calculated using the following values of m and n: (*1*) $m = 3$, $n = 7$; (*2*) $m = 3.5$, $n = 7$; (*3*) $m = 4$, $n = 7$; (*4*) $m = 5$, $n = 7$ for V; (*1*) $m = 6$, $n = 8$; (*2*) $m = 8$, $n = 10$ for Cr; $m = 5$, $n = 7$ for Mn; (*1*) $m = 6$, $n = 8$; (*2*) $m = 6$, $n = 10$ for Fe; (*1*) $m = 3$, $n = 7$; (*2*) $m = 3.5$, $n = 7$ for Co; $m = 3.5$, $n = 7$ for Ni; and $m = 3.5$, $n = 7$ for Cu.

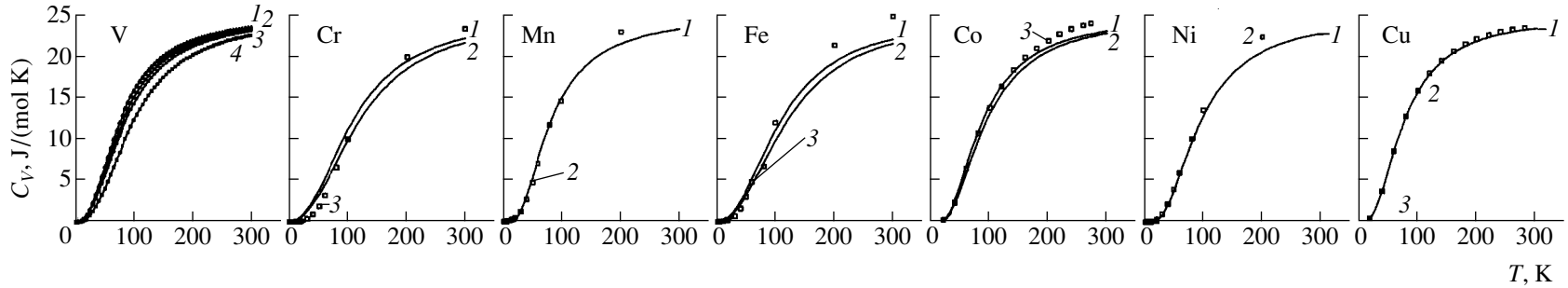

Fig. 2. Specific heat $C_V(T)$ determined based on the phonon spectra calculated using the following parameters: (*1*) $m = 2$, $n = 7$; (*2*) $m = 3.5$, $n = 7$ for V; (*3*) $m = 4$, $n = 7$; (*4*) $m = 5$, $n = 7$; (*1*) $m = 6$, $n = 8$; (*2*) $m = 8$, $n = 10$ for Cr (*3* are experimental points); (*1*) $m = 5$, $n = 7$ for Mn (*2* are experimental points); (*1*) $m = 6$, $n = 8$; (*2*) $m = 6$, $n = 10$ for Fe (*3* are experimental points); (*1*) $m = 2$, $n = 7$; (*2*) $m = 3.5$, $n = 7$ for Co (*3* are experimental points); (*1*) $m = 3.5$, $n = 7$ for Ni (*2* are experimental points); (*1*) $m = 3.5$, $n = 7$ for Ni (*2* are experimental points); and (*1*) $m = 3.5$, $n = 7$ for Cu (*2* are experimental points).

The calculations were carried out for $\frac{1}{48}$th of the Brillouin zone at 1618 points. The points were chosen by the Monte Carlo method [5].

The calculated lattice phonon spectra of elements with Z = 23–29 are shown in Fig. 1. The figure also illustrates the effect on the boundary value ν_m of the variation in m at n = const and the same for n at m = const. At fixed exponent n, the increase in m, as well as the increase of n for m = const, is accompanied by a nearly linear increase of boundary frequency ν_m. The determined values of m and n, which do not differ much from to those found by Fürth, correspond to boundary frequency ν_m close to the Debye frequency ν_D. Note that at variation of m, n, and $\frac{U_0}{r_0^2}$, their large deviation from the equilibrium values causes an "overshoot" of the initial point of the spectrum related to "negative" frequencies arising in the Brillouin zone.

The equilibrium molar values of atomization energies U_m [9] and interatomic distances r_0 determined using the equilibrium values of lattice constant a [10] and given values of m and n are presented in Table 2. The values of exponents m and n, for which the calculated values of $C_V(T)$ are in the best agreement with experimental data, are m = 6, n = 10 for Cr, m = 6, n = 10 for Fe, m = 5, n = 7 for Mn, and m = 3.5 and n = 7 for Co, Ni, and Cu.

The temperature dependence of specific heat $C_V(T)$ is shown in Fig. 2; it is determined based on the calculated phonon spectra (see Fig. 1). The experimental points [11, 12] are also plotted in addition to the calculated curves. The experimental data $C_V(T)_{\text{expt}}$ (points) presented in Fig. 2 include not only the lattice contribution to the specific heat, but the magnetic and other contributions as well. The deviations of experimental points from the calculated $C_V(T)$ curves observed at high temperatures are caused predominantly by the magnetic contribution to $C_V(T)_{\text{expt}}$. A good agreement between calculated and experimental data for $C_V(T)$ is observed for copper and, below 100–200 K, also for the other elements with relatively small magnetic contribution to $C_V(T)$.

In conclusion, we demonstrated for the first time that the calculations of the phonon spectra for the elements of cubic structure performed by the BKDB method using the Mie–Grüneisen potential lead us to results interesting from the viewpoint both of fundamental science and its applications.

REFERENCES

1. M. Born and K. Huang, *Dynamical Theory of Crystal Lattices* (Clarendon Press, Oxford, 1954; Inostrannaya Literatura, Moscow, 1958).
2. V. Blackman, Proc. R. Soc. (London), Ser. A **148**, 384 (1934).
3. De Launay, in *Solid State Physics*, Ed. by F. Seits and D. Turnbull (Academic Press, New York, 1956), Vol. 2, pp. 219–348.
4. S. C. Upadhyaya, J. C. Upalhyaya, and R. Shyam, Phys. Rev. B **44**, 122 (1991).
5. N. N. Sirota and T. D. Sokolovskiĭ, in *Chemical Bond in Semiconductors and Solids* (Consultant Bureau, New York, 1967), pp. 139–143.
6. P. Debye, Ann. Phys. **39** (4), 89 (1912).
7. N. N. Sirota, in *Physics and Physicochemical Analysis* (Moscow, 1957), Vol. 1, pp. 138–150.
8. R. Fürth, Proc. R. Soc. (London), Ser. A **193** (992), 87 (1944).
9. *Properties of Elements*, Part 1: *Physical Properties, Reference Book*, Ed. by G. V. Samsonov (Metallurgiya, Moscow, 1976).
10. J. Emsley, *The Elements* (Claremdon Press, Oxford, 1989; Mir, Moscow, 1993).
11. H. Zeise, in *Termodynamik. Tabellen* (S. Hirzel, Leipzig, 1954), Vol. 3/1.
12. *Handbook on Physicochemical Fundamentals of Cryogenics*, Ed. by M. P. Malkov (Énergoatomizdat, Moscow, 1985).

Translated by T. Galkina

Doklady Physics, Vol. 45, No. 8, 2000, pp. 384–388. Translated from Doklady Akademii Nauk, Vol. 373, No. 6, 2000, pp. 754–758.

PHYSICS

Experimental Study of Inelastic Collisions of Low-Velocity Electrons with Terbium Atoms

Yu. M. Smirnov

Presented by Academician A.F. Andreev December 30, 1999

Received November 30, 1999

1. The terbium atom is a relatively rare object for study. Restricting ourselves by considering such fields of physics as atomic structure, atomic spectroscopy, and electron-atomic collisions, the latest publication we have found related to this scope of problems is dated 1991 [1]. In that paper, the high-lying excited and self-ionization states of TbI were investigated. The study [2] devoted to determining the oscillator strengths for TbI and TbII appeared almost a decade before. Studies in which the single-charged terbium ion was investigated are almost equally scanty.

It is possible that such a state of research of the terbium atom is one of the principal reasons for extremely restricted usage of this element until now. As an illustration, we can say that in [3], none of examples for using terbium was cited. At the same time, at the moment of publication of the book [3], the laser generation on the single $^5D_4 \longrightarrow {}^7F_5$ transition was already realized for the tricharged Tb^{3+} ion situated in condensed media. We imply the organometallic liquid laser on the basis of trifluor-acetylacetonate and the laser based on $LiYF_4$ crystal sensitized by Gd^{3+} and activated by Tb^{3+} [4]. However, in gas lasers, no generation using terbium-atom transitions was obtained until now [5].

The most complete (unpublished) tables of the terbium spectrum are prepared by Klinkenberg on the basis of spectrograms for an electrode-free discharge, which were obtained in the Argonne National Laboratory (USA). These tables involve approximately 30000 spectral lines for TbI and TbII within the spectral range from 233 to 929 nm. A further analysis of these lines was accomplished in the Zeeman Laboratory (Amsterdam) [6–11]. The results of [6–11] were subjected to critical analysis in the compilation [12] into which the data of [13], published almost simultaneously with [12], were also included.

In [13], the energy structure of the even low-level configuration $4f^85d6s^2$ of the terbium atom was calculated. The energy matrix was parameterized by means of 11 independent parameters taking into account the electrostatic interaction, relativistic effects, and configuration overlapping. The parameters were found on the basis of known experimental positions for 45 levels of TbI by the method of minimization of the mean-square deviation ΔE, $\Delta E = 41$ cm^{-1} being attained in this case. The total number of levels in the configuration under study is 2725. The dimension of the energy matrix attains 377 (for $J = 9/2$). The hyperfine structure of levels was calculated separately. The results of calculation for 57 levels with the parental term $4f^8{}^7F$, namely, positions of levels, weights of three major components, and the g factor are presented. As was indicated in the previous item, these results are included in the compilation [12].

Although there are rather extensive (but not always very reliable) data on the TbI spectrum, information concerning atomic constants of the terbium atom is almost completely absent. In the paper [14] devoted to detailed measurements of radiative constants for atoms and single-charged ions of 70 elements, from several tens to several hundreds of numerical values of these constants were obtained for the majority of the objects. However, only three values were obtained in this study for TbI and none for TbII. There are neither experimental nor theoretical data on the cross sections for the excitation of a terbium atom by slow electrons.

2. In this study, using the method of extended intersecting beams, we investigated inelastic collisions of low-velocity monoenergetic electrons with terbium atoms. The instrumentation and experimental methods were repeatedly described previously; the most detailed information is given elsewhere [15].

We used metallic terbium of the TbM-1 brand with a total impurity content of less than 0.1% (the major impurities were gadolinium, disprosium, and ittrium). Terbium was evaporated from a tantalum boat in the course of electron-beam heating. The usage of a crucible (of the Knudsen-cell type) with a low expense of a metal was impossible because the available electrically conducting constructional materials cannot hold long-term contact with the melted terbium and fail. Temperature of metal at the basic stage of the experiment

Moscow Power Engineering Institute, ul. Krasnokazarmennaya 17, Moscow, 111250 Russia

1028-3358/00/4508-0384$20.00

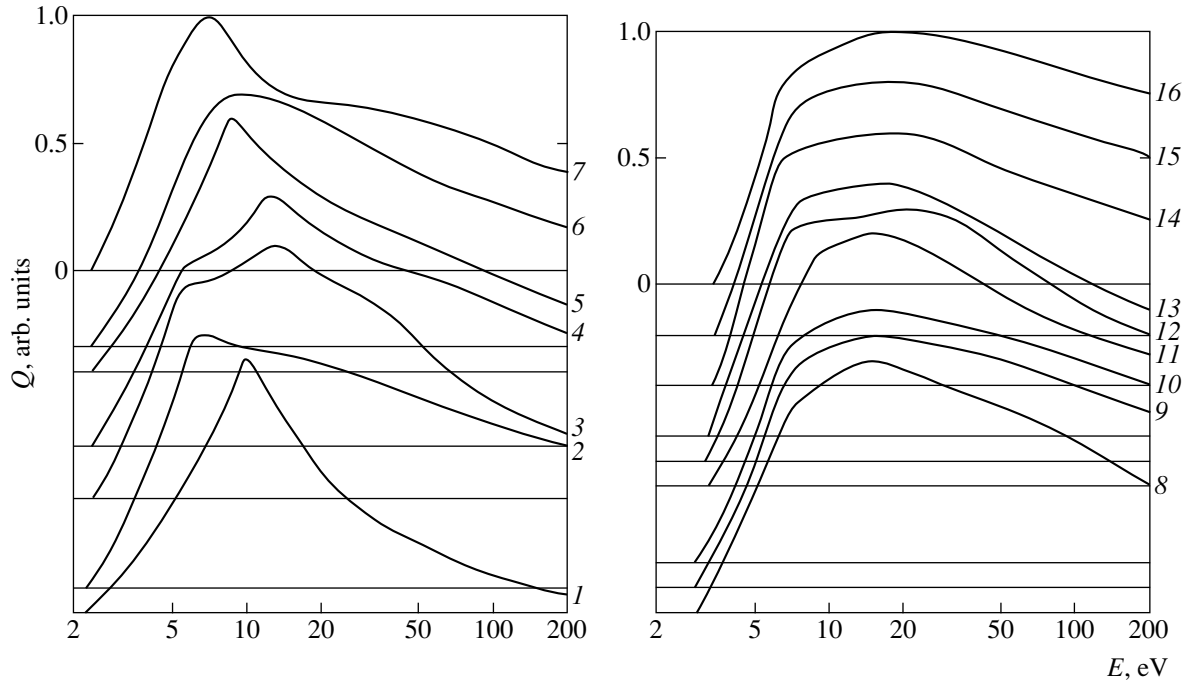

Fig. 1. Optical excitation functions for terbium atom.

attained 1800 K. In this case, the atomic concentration in the region of the intersection of the atomic and electron beams was 7.0×10^9 cm^{-3}. To minimize the reabsorption while investigating the most intense transitions to low-lying levels, the atomic concentration was reduced almost by an order of magnitude.

The evaporation of terbium atoms is inevitably accompanied by the occupation of low-lying levels in TbI as a result of the action of the thermal excitation mechanism. The existing technique renders it impossible to carry out either the selection of atoms excited to one of the low-lying levels or the measurement of their concentration under conditions of this experiment. Estimating the population of these levels under the assumption that the Boltzmann distribution is valid, we find the following values for the total percent concentration of atoms in the beam: 27.8 for $4f^9 6s^2\,{}^6H^\circ_{15/2}$ (0); 19.4 for $4f^8 5d 6s^2\,{}^8G_{13/2}$ (285); 19.2 for $4f^8 5d 6s^2\,{}^8G_{15/2}$ (462); 13.9 for $4f^8 5d 6s^2\,{}^8G_{11/2}$ (510); 5.83 for $4f^8 5d 6s^2_{9/2}$ (1371); 3.31 for $4f^8 5d 6s^2\,{}^8D_{11/2}$ (2310); 2.03 for $4f^8 5d 6s^2\,{}^8G_{7/2}$ (2419); 2.68 for $4f^9 6s^2\,{}^6H^\circ_{13/2}$ (2772); and 1.81 for $4f^8 5d 6s^2\,{}^8G_{9/2}$ (2840). The numbers in the parentheses correspond to the level energies (expressed in cm^{-1}) counted off from the ground level of the terbium atom. Here, all TbI levels below 3000 cm^{-1} are indicated. As follows from these data, the summary population of odd levels amounts to only 30.5%, whereas that of even levels is 65.5% (approximately 4% correspond to high-lying levels). Undoubtedly, the presence of such a distribution must be taken into account when comparing the results of this study with data of theoretical calculations (as only such results will appear).

The width of the electron-beam energy distribution corresponded to 0.9 eV at an energy of 100 eV and to 1.0 eV at 20 and 200 eV (for 90% of electrons). Within the entire working energy range, the current density did not exceed 1.0 mA/cm^2. The spectral resolution of the setup attained approximately 0.1 nm in the short-wave range ($\lambda \le 600$ nm) and approximately 0.2 nm in the yellow–red spectral region. An error in measuring relative values of cross sections was within 3 to 10% depending on the line intensity. An error in determining absolute values of the cross sections was within ±16 to ±23%. Principal error sources and their contribution to the resulting error are analyzed in [15].

3. In spectrograms detected at an exciting-electron energies of 30 eV, we find nearly 630 spectral lines of the terbium atom. Within the electron-energy range 0 to 200 eV, 103 optical excitation functions (OEFs) were detected. For almost all the transitions, the upper and lower levels between which these transitions occur were established. However, for the very majority of the upper levels from the whole set of quantum characteristics, only the parity and the value of the quantum number J are known. That is why transitions with the participation of these levels are essentially inaccessible right now for theoretical analysis. Therefore, we discuss in this study only such transitions for which the upper levels are completely classified (or, at least, the configurations are established), and also, the OEFs are

Excitation cross sections of terbium atom

λ, nm	Transition	J	E_l, cm^{-1}	E_u, cm^{-1}	Q_{30}, 10^{-18} cm^2	Q_{max}, 10^{-18} cm^2	E_{max}, eV	OEF
370.311	$4f^85d6s^2{}^8G$–$4f^85d^26p$?	15/2–17/2	462	27458	12.7	13.1	18	16
371.790	$4f^85d6s^2{}^8G$–$4f^85d^26p$?	11/2–13/2	509	27399	2.59	2.70	15–20	15
390.133	$4f^85d6s^2{}^8G$–$4f^85d^26p$?	15/2–17/2	462	26087	117.0	123.0	18	14
431.883	$4f^96s^2{}^6H°$–$4f^96s6p$ (15/2, 1)	15/2–15/2	0	23147	248.0	261.0	16	10
432.643	$4f^96s^2{}^6H°$–$4f^96s6p$ (15/2, 1)	15/2–17/2	0	23107	331.0	348.0	16	9
433.643	$4f^96s^2{}^6H°$–$4f^96s6p$ (13/2, 1)	13/2–15/2	2771	25825	37.0	40.2	17	13
433.841	$4f^96s^2{}^6H°$–$4f^96s6p$ (15/2, 1)	15/2–13/2	0	23043	224.0	251.0	14	8
435.681	$4f^96s^2{}^6H°$–$4f^96s6p$ (13/2, 1)	13/2–13/2	2771	25717	41.4	42.6	20	12
437.202	$4f^96s^2{}^6H°$–$4f^96s6p$ (13/2, 1)	13/2–11/2	2771	25637	25.7	29.2	14	11
438.245	$4f^85d6s^2{}^8H$–$4f^85d^26p$?	17/2–17/2	4646	27458	19.7	20.3	18	16
466.279	$4f^85d6s^2{}^8H$–$4f^85d6s6p$?	17/2–17/2	4646	26087	12.2	12.8	18	14
489.813	$4f^85d6s^2{}^8H$–$4f^85d^26p$?	11/2–13/2	6988	27399	0.65	0.68	15–20	15
491.523	$4f^85d6s^2{}^6G$–$4f^85d^26p$?	13/2–13/2	7059	27399	1.17	1.22	15–20	15
509.229	$4f^85d6s^2{}^6H$–$4f^85d^26p$?	15/2–13/2	7767	27399	0.81	0.84	15–20	15
518.848	$4f^85d^26s^{10}G$–$4f^85d^26p$?	15/2–17/2	8190	27458	0.96	0.99	18	16
522.199	$4f^85d6s^2{}^8G$–$4f^85d6s6p$?	15/2–13/2	462	19606	3.89	6.06	7.5	7
522.812	$4f^85d^26s^{10}G$–$4f^85d^26p$?	13/2–13/2	8277	27399	3.22	3.35	15–20	15
523.511	$4f^85d6s^2{}^8G$–$4f^85d6s6p$?	11/2–13/2	509	19606	4.81	7.50	7.5	7
524.871	$4f^85d6s^2{}^8G$–$4f^85d6s6p$?	13/2–11/2	285	19332	5.85	7.21	9.5	6
531.923	$4f^85d6s^2{}^8G$–$4f^85d6s6p$?	13/2–15/2	285	19080	12.4	15.5	13	3
533.104	$4f^85d^26s^{10}G$–$4f^85d^26p$?	11/2–13/2	8646	27399	1.38	1.44	15–20	15
534.604	$4f^85d6s^2{}^8G$–$4f^85d6s6p$?	15/2–17/2	462	19162	7.45	12.0	9.0	5
535.488	$4f^85d6s^2{}^8G$–$4f^85d6s6p$?	15/2–17/2	462	19131	12.0	15.8	13	4
536.972	$4f^85d6s^2{}^8G$–$4f^85d6s6p$?	15/2–15/2	462	19080	13.3	16.6	13	3
550.961	$4f^85d6s^2{}^8G$–$4f^85d6s6p$?	15/2–13/2	462	18607	2.68	3.26	6.5	2
552.412	$4f^85d6s^2{}^8G$–$4f^85d6s6p$?	11/2–13/2	509	18607	5.65	6.88	6.5	2
560.058	$4f^85d6s^2{}^8G$–$4f^85d6s6p$?	13/2–13/2	285	18135	1.15	2.87	10.0	1
567.184	$4f^85d6s^2{}^8G$–$4f^85d6s6p$?	11/2–13/2	509	18135	9.90	24.7	10.0	1
613.439	$4f^85d6s^2{}^8D$–$4f^85d6s6p$?	11/2–13/2	2310	18607	2.09	2.55	6.5	2
688.730	$4f^85d6s^2{}^8H$–$4f^85d6s6p$?	17/2–17/2	4646	19162	6.02	9.70	9.0	5
690.198	$4f^85d6s^2{}^8H$–$4f^85d6s6p$?	17/2–17/2	4646	19131	6.31	8.30	13	4
831.706	$4f^85d6s^2{}^6G$–$4f^85d6s6p$?	13/2–15/2	7059	19080	29.9	37.3	13	3
844.397	$4f^85d6s^2{}^6H$–$4f^85d6s6p$?	15/2–13/2	7767	19606	54.4	84.8	7.5	7
848.359	$4f^85d6s^2{}^8H$–$4f^85d6s6p$?	13/2–13/2	6351	18135	46.4	116.0	10.0	1

measured. Moreover, we omit several transitions blended by relatively intense unclassified lines.

The results of the measurements are shown in the table. Here, we present only the wavelength λ, transition notation, inner quantum number J, energies E_l and E_u of the lower and upper levels, and the cross sections Q_{30} and Q_{max} at an electron energy of 30 eV and in the OEF maximum, respectively, and the position E_{max} of this maximum. The enumeration of the OEFs in the table and of the curves in Fig. 1 coincide with each other. Here, we used the logarithmic scale along the abscissa axis and the linear scale along the ordinate axis. In this case, each curve is normalized to unity in its maximum and has an individual zero for counting off along the ordinate axis.

The state diagram for the terbium atom is presented in Fig. 2, where all known TbI configurations are shown. The high-lying levels found in [1] are shown in Fig. 2 by shaded blocks. We have determined positions for 85 even (I) and 135 odd (II) levels. However, the measurement accuracy for the level energies in [1] corresponds to ±0.3 cm^{-1}, and no quantum numbers are known for them by now, including J.

It should be taken into account that only the two lowest terms are established definitely for odd states, namely, the ground term $4f^9 6s^2\,{}^6H^\circ$ and the excited term $4f^8({}^7F_6)6s^2 6p_{1/2}(6, 1/2)^\circ$ nearest to the ground one. In this case, even within the ground term, the two highest levels with $J = 7/2$ and 5/2 are unknown. Almost all the terms and configurations for the levels with an energy higher than that, corresponding to 13 700 cm^{-1}, are established only hypothetically. The mixing parameters are known only for the ground-term levels that involve 93 to 97% of the main component and, thus, are very close to the pure levels in the *LS*-coupling symbolism.

None of the odd configurations was completed. In Fig. 2, this fact is shown by dashed lines closing every configuration from the side of higher energies. The degree of incompleteness can be illustrated by an example contained in Section 1 of this paper: From the total number 2725 levels in the even configuration $4f^8 5d6s^2$, only 57 were calculated in [13]. In the odd configuration $4f^8 5d^2 6p$, only six levels are known; in the higher lying configuration $4f^9 6s7s$, only two levels are known. However, they are cited in [12] as definitely established. According to the data given in [12], the boundary of the highest odd levels is near 35000 cm^{-1}, the first ionization limit of TbI being 47295 cm^{-1}. Here, we imply all the experimental levels independently of the presence or absence of their classification (the levels from [1] are shown separately).

In the even part of the diagram, the situation is somewhat more favorable. For the lowest configuration $4f^8 5d6s^2$, as was noted earlier, we classified 57 levels, the majority of which are related to nine definitely established terms. Moreover, the mixing parameters are known for the levels of these terms. Only four terms from nine remain partially unfilled (1 to 2 levels are deficient). In the next configuration $4f^8 5d^2 6s$, we have definitely established only the lowest term $4f^8({}^7F)5d^2({}^3F)({}^9G)6s\,{}^{10}G$ for which, however, the highest level with $J = 1/2$ is not found. The decuplet level $4f^8({}^7F)5d^2({}^3F)({}^9I)6s\,{}^{10}I_{21/2}$ is also definitely established.

Finally, in the even configuration $4f^9 6s6p$, 11 levels are known. For four of them, the terms are hypothetically established, and an additional six levels belong definitely to two terms written out in denotations of the J_1J_2-coupling: $4f^9({}^6H^\circ)6s6p({}^1P_1^\circ)$ (15/2, 1) and $4f^9({}^6H^\circ_{13/2})6s6p({}^1P_1^\circ)$ (13/2, 1). The data given in the table show that the transitions from the levels of the first of these terms have the largest excitation cross sections among measured ones. The excitation cross sections for the levels of the second of the above terms are also large and attain (3–4) × 10^{-17} cm^2, whereas, for the most frequently appearing level of 27 399 cm^{-1}, the total excitation cross section is only 0.98 × 10^{-17} cm^2 for the 30-eV electron energy. In this case, as can be seen from Fig. 1, the OEFs for the levels related to the same term are very similar in their shape (curves *8*, *9*, *10* and *11*, *12*, *13*, respectively). The most probable reason for the marked difference between the OEF *12* and two neighboring ones is likely the spectral overlapping of the unidentified line. Some other OEFs have also a significant similarity in their shape (*1* and *5*, *3* and *4*, *14* and *15*, or *14* and *16*). However, their belonging to particular terms remains unknown, so that this similarity can be caused by random reasons.

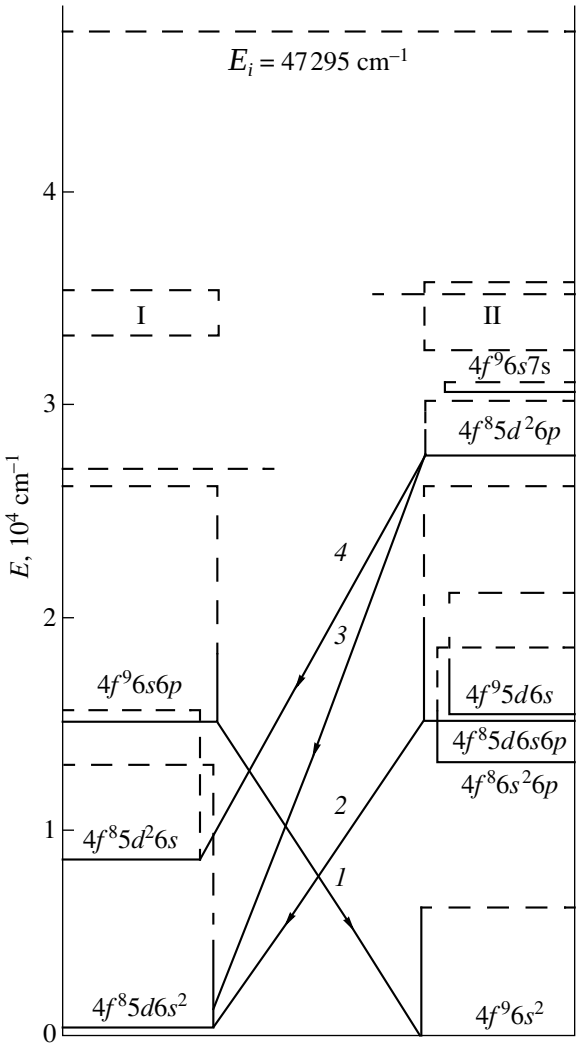

Fig. 2. Diagram for states of terbium atom with transitions investigated.

The group of transitions denoted by arrow *3* in Fig. 2 should be specially mentioned. The group of transitions *1*, *2*, and *4* are quite permissible by the selection rules in the dipole approximation because all of them correspond to the configuration change $6p \longrightarrow 6s$. To the contrary, the transitions of group *3* arise in the case of combining the $4f^8 5d^2 6p$ and $4f^8 5d 6s^2$ configurations, i.e., in the case of a radical reconstruction $5d6p \longrightarrow 6s^2$ of the electron shell. Such a transition cannot be realized in the single-electron approximation and is likely realized only due to the presence of a significant mixing of configurations. Actually, for low-lying levels (the $4f^8 5d 6s^2$ configuration), a significant mixing takes place [12]. For the transitions from high-lying levels of the group *3*, the necessary data are absent.

4. Thus, for the first time, the terbium-atom excitation by low-velocity monoenergetic electrons was investigated, and the excitation cross sections were determined. The results obtained can be used as the reference data in solving problems of physics and chemistry of plasmas, astrophysics, etc. At the same time, information obtained on the atomic constants of terbium atom can provide for progress in the extremely complicated theoretical analysis of the TbI structure and spectrum.

REFERENCES

1. V. N. Fedoseev, V. I. Mishin, D. S. Vedeneev, and A. D. Zuzikov, J. Phys. B **24**, 1575 (1991).
2. V. N. Gorshkov, V. A. Komarovskiĭ, A. L. Osherovich, and N. P. Penkin, Opt. Spektrosk. **52**, 935 (1982) [Opt. Spectrosc. **52**, 562 (1982)].
3. *Popular Library of Chemical Elements*, Ed. by I. V. Petryanov-Sokolov (Nauka, Moscow, 1983), Vol. 2.
4. *Laser Handbook*, Ed. by A. M. Prokhorov (Sov. Radio, Moscow, 1978), Vol. 1.
5. V. A. Gerasimov, Opt. Spektrosk. **87**, 156 (1999) [Opt. Spectrosc. **87**, 144 (1999)].
6. P. F. A. Klinkenberg, Physica (Amsterdam) **32**, 1113 (1966).
7. P. F. A. Klinkenberg and E. Meinders, Physica (Amsterdam) **32**, 1617 (1966).
8. P. F. A. Klinkenberg, Physica (Amsterdam) **37**, 197 (1967).
9. E. Meinders and P. F. A. Klinkenberg, Physica (Amsterdam) **38**, 253 (1968).
10. P. F. A. Klinkenberg and E. Meinders, Physica (Amsterdam) **42**, 213 (1969).
11. P. F. A. Klinkenberg, Physica (Amsterdam) **57**, 594 (1972).
12. W. C. Martin, R. Zalubas, and L. Hagan, *Atomic Energy Levels. The Rare Earths Elements* (National Bureau of Standards, Washington, DC, 1978).
13. C. Bauche-Arnoult, J. Sinzelle, and A. Bachelier, J. Opt. Soc. Am. **68**, 368 (1978).
14. C. H. Corliss and W. R. Bozeman, *Experimental Transition Probabilities for Spectral Lines of Seventy Elements* (National Bureau of Standards, Washington, DC, 1962; Mir, Moscow, 1968).
15. Yu. M. Smirnov, J. Phys. II (France) **4**, 23 (1994).

Translated by V. Bukhanov

Doklady Physics, Vol. 45, No. 8, 2000, pp. 389–391. Translated from Doklady Akademii Nauk, Vol. 373, No. 5, 2000, pp. 615–617.

POWER ENGINEERING

Bifurcation of Vortex Turbulent Flow and Intensification of Heat Transfer in a Hollow

S. A. Isaev*, Academician A. I. Leont'ev, P. A. Baranov*, and A. E. Usachev*****

Received April 27, 2000

Analysis of the mechanisms underlying the vortex-induced intensification of heat transfer accompanying the fluid flow along surfaces consisting of concave elements stimulates studies that reveal both the physical nature of large-scale vortex objects generated in hollows and their relation to the heat transfer from a wall. Experimental works concerning this problem (see, for example, [1]) demonstrate, first of all, that there exist non-steady-state cyclic processes involving the formation of vortex flows. It is usually assumed that the latter are responsible for the high level of heat transfer at comparatively low hydrodynamic losses. However, it is very difficult to control these processes because their manifestation depends on the combination of many factors such as relative values of the hollow depth and a radius of curvature characterizing its sharp edge, the arrangement of hollows at the plane (in the case of their ensemble), the thickness of boundary layer, and the degree of turbulence in the incident flow.

An alternative concept is presented by the vortex-induced intensification based on steady-state asymmetric flows around the hollows related to their asymmetric shapes. Numerical studies of laminar [2, 3] and turbulent [4] flows, which occur around a deep isolated hollow at the plane, show that one-sided transverse deformation of the hollow can substantially change the vortex pattern in its vicinity and intensify the fluid motion in the direction transverse to the incident flow. In addition, the laminar flow in the asymmetric hollow does not change the vortex pattern with two large-scale vortex cells observed in spherical hollows [5–7], whereas in the turbulent regime arising there, the transition to a single-vortex tornado-shaped flow pattern turns out to be possible [2]. In the latter case, the flow becomes much more intense in the direction transverse to the hollow. In general, this fact agrees with similar processes that occur in the near-wall zone when a jet is injected at a finite angle with respect to the incident flow [8]. Then, the transition from a symmetric two-vortex flow pattern to that with one vortex is accompanied by a considerable increase in the velocity of the secondary flow.

In this paper, the main emphasis is placed on the relation between the dynamics of vortex structures in a hollow, the extent of its deformation ε (spherical and elliptic parts of the hollow conjoin with each other), and the relative heat transfer from a surface element containing the hollow. Particular attention is given to the bifurcation occurring in the vortex flow around the spherical hollow, which is accompanied by an abrupt change of the thermal regime near the wall. Similarly to [4], spatial jet–vortex structures were revealed by the computer visualization of the flow based on tracing tagged particles in the fluid. As a basic geometrical configuration, we consider a spherical hollow (0.22 in depth) having rounded edges (of radius 0.1), which supports a steady-state turbulent flow with the developed zone of flow separation.

For the numerical simulation of turbulent flow in the vicinity of curved surface elements, we use an approach based on implementation of multiblock nets. This approach was tested in calculations of two-dimensional flows with vortex cells [6]. The constructed factorized algorithm is based on the implicit finite-volume method of solving the Navier–Stokes equations with the Reynolds averaging, which are closed according the Menter zonal two-parameter model of turbulence [9]. The algorithm involves partitioning of the calculation region and generation of oblique overlapping nets of the H and O types in selected subdomains having essentially different scales. The starting set of equations is written in the divergence form with respect to increments of dependent variables, where the latter include the Cartesian components of velocity. In the source terms appearing in the equations for momentum, the convection-induced flows are approximated using the Leonard one-dimensional counterflux scheme with quadratic interpolation. In the transport equations for turbulent characteristics, these terms are approximated by the UMIST counterflux scheme [10],

* *Academy of Civil Aviation, ul. Pilotov 38, St. Petersburg, 196210 Russia*

** *Bauman State Technical University, Vtoraya Baumanskaya ul. 5, Moscow, 107005 Russia*

*** *State Research Center Zhukovskii Central Institute of Aerohydrodynamics, ul. Radio 17, Moscow, 107005 Russia*

1028-3358/00/4508-0389$20.00

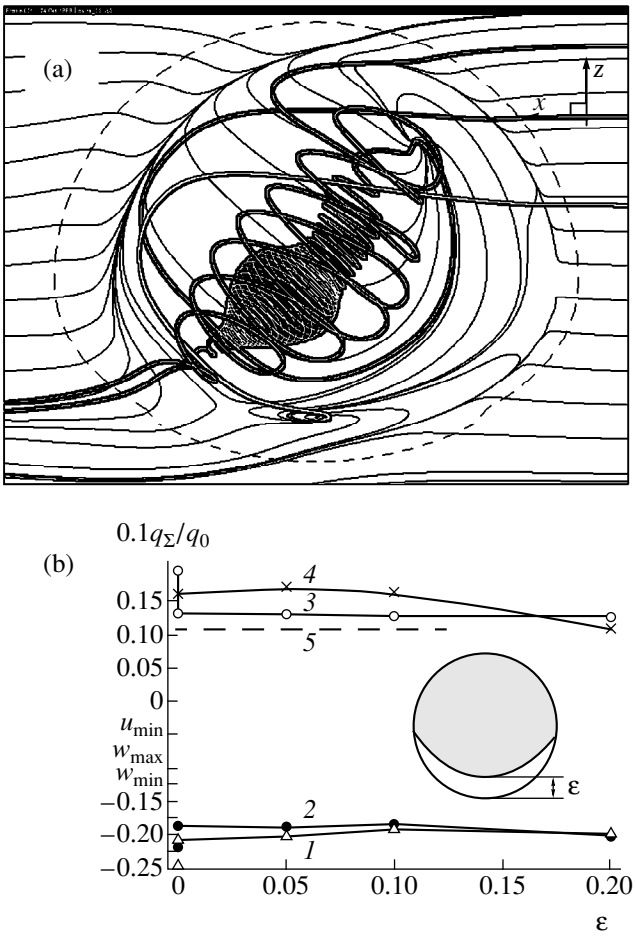

Fig. 1. (a) Computer visualization of jet–vortex objects arising in the asymmetric hollow and (b) the effect of shape asymmetry ε on the minimum values of (*1*) longitudinal (u_{min}) and (*2*) transverse (w_{min}) velocities, (*3*) on the maximum value of the transverse velocity w_{max}, and (*4*) 1/10 of the ratio of the total heat load q_Σ per circular element containing the hollow and the load q_0 per element without the hollow. Dashed line (*5*) corresponds to the calculations corresponding to the symmetric vortex flow pattern in the spherical hollow, which is presented in Fig. 2a.

which is a modification of the TVD scheme. In its main features, our methodology is similar to the one used in [4].

For a more accurate description of structural elements corresponding to the different scales in the turbulent flow around a deep hollow, such as, the shear layer and the backward-flow zone, it is reasonable to separate out a near-wall domain surrounding the hollow. It is the cylindrical ring of the outer radius equal to unity, the inner radius of 0.1, and height 0.175, where all of the linear dimensions are measured in units of the hollow diameter. The domain under study is partitioned by an oblique curved net, which conforms to the surface interacting with the flow. We place 60 uniformly distributed cells along the circle, 45 cells in a vertical direction with higher node concentration near the wall (the minimum near-wall step is equal to 0.0008). In the radial direction, we specify 40 cells concentrating toward the boundary of the hollow (the minimum step is equal to 0.015).

The considered subdomain of the hollow is covered by a large-scale rectangular domain, where the base of the latter coincides partly with the flat wall interacting with the flow. The origin of Cartesian coordinates coincides with the projection of the hollow center onto the plane. The domain length, height, and width are equal to 17, 5, and 10, respectively. It is partitioned by the Cartesian net containing $55 \times 40 \times 45$ cells. Nodes of the net are concentrated in the vicinity of the hollow (the minimum step in the longitudinal and transverse directions is equal to 0.15) and near the wall (the near-wall step is equal to 0.001).

To better resolve the near-wall flow in a vicinity of the axis of the cylindrical subdomain, we introduce the "patch" that passes through this subdomain and has a shape of a curved parallelepiped. The 19×19 net having a uniform node distribution in the longitudinal and transverse directions is constructed inside it. Steps of this net are consistent with the near-boundary step in the neighboring cylindrical domain. In the same manner, the arrangement of the net nodes is adjusted in the vertical direction.

The velocity profile specified at the entrance boundary of the domain corresponds to the 1/7 profile of the turbulent boundary layer, where the thickness (0.175) of the latter is close to the hollow depth. We specify soft boundary conditions (those of continuation of the solution) at the exit boundaries and the nonslip condition at the heated isothermal wall. The velocity of the incident flow outside the boundary layer and the hollow diameter are used as the normalization parameters to reduce the problem to the dimensionless form. The Reynolds number is assumed to be equal to 2.35×10^4. While solving the heat transfer problem, we take the values 0.7 and 0.9 for the laminar and turbulent Prandtl numbers, respectively.

Some numerical results obtained using the TECPLOT computer-based system for visualization of spatial fields are presented in Figs. 1 and 2.

For the asymmetric hollow under study ($\varepsilon = 0.2$), a flow pattern is shown in Fig. 1a. It has a pronounced asymmetric character, where sidewash occurs in the direction of the deformed part of the hollow and the pressure maximum is shifted toward the opposite side. As for the spherical part of this hollow, the pattern is approximately the same as in the case of the symmetric hollow in the laminar flow regime [2, 3]. It is characterized by a focus-type singularity, which is situated at the periphery of the hollow, and the swirling jet flow forms in the vicinity of this singularity. Inside the asymmetric hollow, the large-scale vortex flow has a snail-like structure with a single-vortex tornado. This structure clearly manifests itself at the tracing of tagged particles introduced at different spatial points. Similar to the

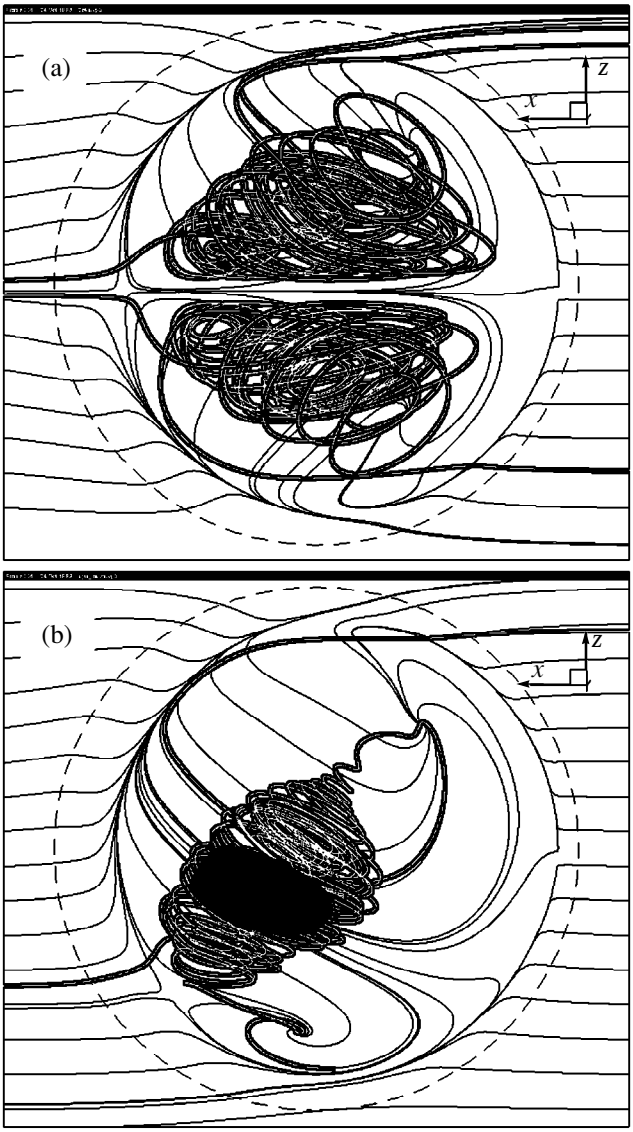

Fig. 2. (a) Symmetric and (b) asymmetric patterns of jet–vortex structures arising in the spherical hollow at the plane in the case of turbulent flow around the hollow.

laminar flow in the asymmetric hollow [2, 3], the separation zone is not closed. As a result, the incident flow penetrates the hollow through the open lateral window from the side of its spherical part. This effect substantially intensifies the vortex motion in the fluid.

When parameter ε characterizing the degree of the hollow deformation varies from 0 to 0.2, both the extremum values of the transverse velocity component and the minimum value of the longitudinal backward-flow velocity in the hollow remain nearly unchanged. Nevertheless, the ratio of the total heat load q_Σ per a circular element of unit radius containing the asymmetric hollow and load q_0 applied to a similar element without a hollow exhibits a pronounced peak with the height exceeding the heat transfer from the flat wall by a factor of 1.7. Relative heat transfer from the element containing a hollow decreases with an increase in the degree of the hollow asymmetry, since the fraction of the hollow area in the area of the chosen element decreases.

The patterns of two steady-state turbulent flows occurring in the spherical hollow are compared in Fig. 1. One of them was obtained in the absence of strong input perturbation caused by initial asymmetry of the hollow, while the other demonstrates the effect of such a perturbation. Symmetric vortex structure, characteristic of laminar flows in the spherical hollow [2] (Fig. 2a), transfers to the single-vortex tornado structure (Fig. 2b); that is, we have the vortex-flow bifurcation. A similar bifurcation arises in the separation flow that occurs in the plane-parallel symmetric channel with an abrupt widening [11]. This bifurcation leads to a significant decrease in the heat transfer in the case of the symmetric vortex pattern.

ACKNOWLEDGMENTS

This work was supported by the Russian Foundation for Basic Research, projects nos. 00-02-81045 and 99-02-16745.

REFERENCES

1. V. V. Alekseev, I. A. Gachechiladze, G. I. Kiknadze, *et al.*, in *Proceedings of the II Russia National Conference on Heat Transfer, Moscow, 1998*, Vol. 6, pp. 33–42.
2. S. A. Isaev, A. I. Leont'ev, A. E. Usachev, *et al.*, in *Proceedings of the II Russia National Conference on Heat Transfer, Moscow, 1998*, Vol. 6, pp. 121–124.
3. S. A. Isaev, A. I. Leont'ev, A. E. Usachev, *et al.*, Izv. Akad. Nauk, Énerg., No. 2, 126 (1999).
4. S. A. Isaev, A. I. Leont'ev, and P. A. Baranov, Pis'ma Zh. Tekh. Fiz. **26** (1), 28 (2000) [Tech. Phys. Lett. **26**, 15 (2000)].
5. S. A. Isaev, A. I. Leont'ev, D. P. Frolov, *et al.*, Pis'ma Zh. Tekh. Fiz. **24** (6), 6 (1998) [Tech. Phys. Lett. **24**, 209 (1998)].
6. S. A. Isaev, P. A. Baranov, A. E. Usachev, *et al.*, in *Proceedings of the IV ECCOMAS CFD Conference, Athens, 1998*, Vol. 1, Part 2, pp. 768–774.
7. S. A. Isaev, in *Problems of Gas Dynamics and Heat and Mass Transfer in Power Engineering: Proceedings of the XII School-Workshop of Young Scientists and Engineers organized by Academician A. I. Leont'ev, Moscow, 1999*, pp. 17–20.
8. F. S. Henry and H. H. Pearcey, AIAA J. **32**, 2415 (1994).
9. F. R. Menter, AIAA J. **32**, 1598 (1994).
10. F. S. Lien, W. L. Chen, and M. A. Leschziner, Int. J. Numer. Methods Fluids **23**, 567 (1996).
11. F. Battaglia, S. J. Tavener, A. K. Kulkarni, *et al.*, AIAA J. **35**, 99 (1997).

Translated by Yu. Verevochkin

Doklady Physics, Vol. 45, No. 8, 2000, pp. 392–394. Translated from Doklady Akademii Nauk, Vol. 373, No. 4, 2000, pp. 474–476.

MECHANICS

A Method of Transferring Boundary Conditions by Cauchy–Krylov Functions for Rigid Linear Ordinary Differential Equations

A. Yu. Vinogradov and Yu. A. Vinogradov

Presented by Academician G.G. Chernyĭ November 12, 1999

Received November 22, 1999

The problem of stable numerical transferring of the boundary conditions for rigid linear ordinary differential equations was first considered in 1961 by Abramov [1] and Godunov [2]. After separation of variables, partial differential equations in deformation mechanics for plates and shells are reduced to these equations. In numerically integrating differential equations by step methods, e.g., in the Godunov method, the orthonormalization procedure is applied for stable calculations.

In this study, we demonstrate a radically new method for improving the efficiency of transferring the boundary conditions to a given point x^* within the integration interval [0, 1]. This method is not time consuming, decreases requirements to the computer RAM, and provides a given error of calculations.

We consider a boundary value problem represented by the system of first-order differential equations in the matrix form

$$\mathbf{Y}' = F\mathbf{Y} + \mathbf{Q}, \tag{1}$$

where $(*)' = d(*)/dx$; $\mathbf{Y} = \{y_1(x), \ldots, y_m(x)\}^{\mathrm{T}}$ is the unknown vector function with the dimension m, $F = \|f_{ij}(x)\|$ is the matrix of variable coefficients $f_{ij}(x)$ with the dimension $m \times m$, and $\mathbf{Q} = \{q_1(x), \ldots, q_m(x)\}^{\mathrm{T}}$ is the vector function with the dimension m standing on the right-hand side of equation (1) and describing an external load. The boundary conditions at the edges of the interval [0, 1] are given by the relations

$$H_L(0)\mathbf{Y}(0) = \mathbf{r}_L(0), \quad H_R(1)\mathbf{Y}(1) = \mathbf{r}_R(1), \tag{2}$$

where H_L and H_R are the matrices of the boundary conditions having dimensions $(m-r) \times m$ and $r \times m$ and the ranks $m - r$ and r, respectively. $\mathbf{r}_L$ and $\mathbf{r}_R$ are vectors with the dimensions $m - r$ and r, respectively.

Institute of Applied Mechanics,
Russian Academy of Sciences,
Leninskiĭ pr. 32a, Moscow, 117312 Russia

We divide the interval [0, 1] into segments of the stable evaluation by the points

$$x_0 = 0,$$

$$x_1, x_2, \ldots, x_{i-1}, x_i, x_{i+1}, \ldots, x_{n-2}, x_{n-1}, x_n = 1.$$

It is well known [3] that the general solution to differential equation (1) for an arbitrary stable-evaluation segment can be written in two forms. When integrating from the left to the right, it is

$$\mathbf{Y}_i = K(x_{i-1}, x_i)\mathbf{Y}_{i-1} + \mathbf{Y}_0(x_{i-1}, x_i), \tag{3}$$

and when integrating from the right to the left, it is

$$\mathbf{Y}_i = K(x_{i+1}, x_i)\mathbf{Y}_{i+1} + \mathbf{Y}_0(x_{i+1}, x_i). \tag{4}$$

Here, $K(x_{i-1}, x_i)$ and $K(x_{i+1}, x_i)$ are the matrices of the numerical values for of fundamental Cauchy–Krylov functions for homogenous differential equation (1), i.e., when $\mathbf{Q} = 0$, and $\mathbf{Y}_0(x_{i-1}, x_i)$ and $\mathbf{Y}_0(x_{i+1}, x_i)$ are columns for the partial solutions to equation (1).

It is worth noting that solutions (3) and (4) to differential equation (1) are derived without allowing for the boundary conditions since the Cauchy–Krylov functions satisfy arbitrary initial conditions of the problem. It is evident that solutions (3) and (4) using matrices K for the values of the Cauchy–Krylov function and the partial solutions $\mathbf{Y}_0$ derived on their basis link the values of the unknown quantities of the columns $\mathbf{Y}_{i-1}$, $\mathbf{Y}_i$ and $\mathbf{Y}_{i+1}$ at edges of an arbitrary chosen stable-evaluation segment. This property is used for successive independent transferring the boundary conditions in each of adjacent segments of the stable evaluation, starting from the edge ones to a given point x^* within the interval [0, 1].

The values of the fundamental Cauchy–Krylov functions for a homogeneous differential equation with the constant coefficients F = const, i.e., the matrix K for the stable-evaluation segment, are determined with the help of the matrix Taylor series

$$K(x_{i-1}, x_i) = \sum_{m=0}^{m=k} (F\Delta x)^m/m!$$

1028-3358/00/4508-0392$20.00

($\Delta x = x_i - x_{i-1}$ = const is the length of the stable-evaluation segment), which is derived by the successive Picard approximation or on the basis of Newton matrix binomial formula

$$K(x_{i-1}, x_i) = (E + F\Delta x_m)^m$$

($\Delta x_m = \Delta x/m$ = const, m is the number of sections, into which the stable-evaluation interval Δx is divided, and E is the identity matrix), which is, by definition, the solution to the Volterra integral.

For differential equations with variable coefficients, the values of the fundamental Cauchy–Krylov functions are calculated, with the multiplicativity of the Volterra integral taken into account, provided that the integration direction coincides with the positive direction of the x-axis. This is obtained by multiplying the matrix Taylor series in the stable-evaluation segment $\Delta x = x_i - x_{i-1}$ by the formula

$$K(x_{i-1}, x_i) = \prod_{j=e}^{j=1} \sum_{m=0}^{m=k} (F_j \Delta x_j)^m / m!.$$

Here, $\Delta x_j = \Delta x/e$ = const is the length of the stable-evaluation segment,

$$x_0, x_1, x_2, \ldots, x_{j-1}, x_j, x_{j+1}, \ldots, x_{e-2}, x_{e-1}, x_e \in \Delta x_j;$$

$$K(x_{i-1}, x_i) = \prod_{j=e}^{j=1} (E + F_j \Delta x_j),$$

where the quantity Δx_j is chosen from the condition for admission of averaging the variable elements of the matrix F in equation (1).

In the case of the opposite direction of integrating, the order of multiplying in the given formulas is reversed.

The values for partial solutions $\mathbf{Y}_0$ of equation (1) are calculated on the basis of the definition of the so-called Cauchy matrix [3].

The iteration process of transferring the boundary conditions to a given point x^* of the integration interval [0, 1] is the following. At each edge, boundary conditions (2) in the form $H\mathbf{Y} = \mathbf{r}$ are transformed to the equivalent ones written out in the form $W\mathbf{Y} = \boldsymbol{\omega}$ in which the rows $\mathbf{w}_i = \{w_{i1}, \ldots, w_{im}\}$ of the rectangular matrices W are derived by orthonormalizing the rows $\mathbf{h}_i = \{h_{i1}, \ldots, h_{im}\}$ of the rectangular matrix H.

The rows $\mathbf{h}_i = \{h_{i1}, \ldots, h_{im}\}$ are orthonormalized in the following way [4]:

From the first equation of the system $H\mathbf{Y} = \mathbf{r}$ for the boundary conditions, we obtain $\mathbf{w}_1 = \{w_{11}, \ldots, w_{1m}\}$ and ω_1, where $w_{1k} = h_{1k}/(h_{11}^2 + \ldots + h_{1m}^2)^{1/2}$, $k = 1, \ldots, m$ and $\omega_1 = r_1/(h_{11}^2 + \ldots + h_{1m}^2)^{1/2}$, $(w_{11}^2, \ldots, w_{1m}^2) = 1$.

From the second equation of the same system, we have $\mathbf{W}_2 = \{w_{21}, \ldots, w_{2m}\}$ and ω_2, where $w_{2k} = w'_{2k}/(w'^2_{11} + \ldots + w'^2_{1m})^{1/2}$, $k = 1, \ldots, m$, and $\omega_2 = \omega'_2/(w'^2_{21} + \ldots + w'^2_{2m})^{1/2}$, where $w'_{2k} = h_{2k} - (h_2, w_1)w_{1k}$ and $\omega'_2 = r_2 - (h_2, w_1)r_1$. Henceforth, $(h_i, w_j) = (h_{i1}w_{j1} + \ldots + h_{1m}w_{jm})$.

From the ith equation, we find $\mathbf{W}_i = \{w_{i1}, \ldots, w_{im}\}$ and ω_i, where $w_{ik} = w'_{ik}/(w'^2_{i1} + \ldots + w'^2_{im})^{1/2}$, $k = 1, \ldots, m$, and $\omega_i = \omega'_i/(w'^2_{i1} + \ldots + w'^2_{im})^{1/2}$, where $w'_{ik} = h_{ik} - (h_i, w_1)w_{1k} - (h_i, w_2)w_{2k} - \ldots - (h_i, w_{i-1})w_{i-1,k}$ and $\omega'_i = r_i - (h_i, w_1)r_1 - (h_i, w_2)r_2 - \ldots - (h_i, w_{i-1})r_{i-1}$.

We now denote the orthonormalization procedure by the operator M. Then,

$$\{W\mathbf{Y} = \boldsymbol{\omega}\} = M\{H\mathbf{Y} = \mathbf{r}\}.$$

Transferring the boundary conditions from the left edge over adjacent segments of the stable evaluation to a given point x^* of the interval [0, 1] consists in the following.

The orthonormalized conditions $H_L(0)\mathbf{Y}(0) = \mathbf{r}_L(0)$ at the left edge or those already transferred to the point x_i, positioned to the left of the point x^* within the interval [0, 1], are transferred to the point x_{i+1}. This is performed using the values of the fundamental Cauchy–Krylov functions by excluding from the conditions

$$W_L(x_i)\mathbf{Y}(x_i) = \boldsymbol{\omega}_L(x_i)$$

the column $\mathbf{Y}(x_i)$. In this case, solution (4) is used, which was obtained by integrating equation (1) in the direction from the right to the left, i.e., in the direction not coincident with the positive direction of the x-axis. As a result, we have the new vector-matrix equation

$$H_L(x_{i+1})\mathbf{Y}(x_{i+1}) = \mathbf{r}_L(x_{i+1}),$$

where

$$H_L(x_{i+1}) = W_L(x_i)K(x_{i+1}, x_i),$$

and

$$\mathbf{r}_L(x_{i+1}) = \boldsymbol{\omega}_L(x_i) - W_L(x_i)\mathbf{Y}_0(x_{i+1}, x_i).$$

Using the operator M, we transform the latter equation to the form

$$W_L(x_{i+1})\mathbf{Y}(x_{i+1}) = \boldsymbol{\omega}_L(x_{i+1}).$$

By repeating the process described above, the conditions for the left edge are transferred to a given point x^* of the integration interval [0, 1]

$$W_L(x^*)\mathbf{Y}(x^*) = \boldsymbol{\omega}_L(x^*). \quad (5)$$

Similarly, the conditions $H_R(1)\mathbf{Y}(1) = \mathbf{r}_R(1)$ for the right edge are transferred to a given point x^* within the interval [0, 1] by using solution (3)

$$W_R(x^*)\mathbf{Y}(x^*) = \boldsymbol{\omega}_R(x^*). \quad (6)$$

Taking into account the fact that expressions (5) and (6) contain the same column $\mathbf{Y}(x^*)$ and introducing the notation

$$W^* = \left\| \frac{W_L(x^*)}{W_R(x^*)} \right\|, \quad \boldsymbol{\omega}^* = \left| \frac{\boldsymbol{\omega}_L(x^*)}{\boldsymbol{\omega}_R(x^*)} \right|,$$

we obtain the system of algebraic equations

$$W^* \mathbf{Y}(x^*) = \boldsymbol{\omega}^*,$$

where W^* and $\boldsymbol{\omega}^*$ are the square matrix and the column with the dimension m, respectively.

Finally, we find the solution to the boundary value problem at an arbitrary point in the form

$$\mathbf{Y}(x^*) = (W^*)^{-1} \boldsymbol{\omega}^*.$$

The significant features of principal novelty for the method described are

(i) transferring the boundary conditions to a given point within the integration interval with their successive orthogonalization at the ends of each stable evaluation segment with preservation of the vector-column of the unknown quantities;

(ii) independent transferring of the boundary conditions from each edge of the stable-evaluation segments to a given point of the integration interval, which is based on using the fundamental Cauchy–Krylov functions of differential equations;

(iii) a possibility to provide a given error in calculation results.

The method proposed is characterized by a simple algorithm. After orthogonalization by the operator M at the edge of each section for the stable evaluation, boundary conditions (2) are transferred to a given point x^* of the interval [0, 1] with the help of solutions (3) and (4) of differential equation (1). The boundary conditions transformed in the equivalent way with the preserved column of the desired quantities are combined at the given point x^* into a system of algebraic equations for determining unknown values.

Among all known methods of transferring boundary conditions, the method described above can be considered as the most adequate since its algorithm using equivalent transformation transfers given boundary conditions to a given point of the integration interval. Such an algorithm has a principal advantage compared, for example, to the Godunov method, in which the orthogonalizion is carried out for columns of the desired solution rather than for the rows of the boundary conditions. The advantage is the absence of the necessity to memorize in calculations the matrices of the orthogonal transformation of the rows for boundary conditions. At the same time, in the Godunov method, we need to conserve the transformation matrices in order to use them again in determining the desired values of the problem. It is evident that this property of the method constructed above makes it possible to significantly reduce the requirements to both the volume of the computer RAM and computer-time expenditures.

Abandoning step methods of integrating differential equation (1) within segments of the stable evaluation and finding the integral on the basis of the convergent matrix Taylor series or according to the Volterra method additionally and significantly reduce computer time expenditures compared to other known methods.

The error in evaluating the integral on the basis of the convergent matrix Taylor series is determined by comparison of its partial sums. In the case of taking the integral by the Volterra method, the error is determined by comparison of products for different divisions into parts of the stable-evaluation segment.

Also taking into account a possibility of estimating the round-off errors inherent in calculations [5] clarifies that the method constructed makes it possible to obtain the solutions to the boundary value problem with the given error.

The efficiency of the method constructed is confirmed by numerical simulations while solving the boundary value problems in mechanics of deformation of shells with various parameters under the action of concentrated and local loads.

REFERENCES

1. A. A. Abramov, Zh. Vychisl. Mat. Mat. Fiz. **1**, 542 (1961).
2. S. K. Godunov, Usp. Mat. Nauk **16** (3), 171 (1961).
3. F. R. Gantmakher, *Matrix Theory* (Nauka, Moscow, 1967).
4. I. S. Berezin and N. P. Zhidkov, in *Calculation Methods* (Fizmatgiz, Moscow, 1962), Vol. 2.
5. A. P. Filin, *Matrices in Statics of Rod Systems* (Stroĭizdat, Moscow/Leningrad, 1966).

Translated by Yu. Vishnyakov

Doklady Physics, Vol. 45, No. 8, 2000, pp. 395–396. Translated from Doklady Akademii Nauk, Vol. 373, No. 4, 2000, pp. 477–478.

MECHANICS

Amplification of a Shock Wave in a Saturated Porous Medium

Academician V. E. Nakoryakov and V. E. Dontsov

Received March 16, 2000

On the basis of numerical calculations describing a collapse of a cavitation-bubble layer near a rigid wall [1], it was found that inertia effects of the collective bubble collapsing can cause a series of high-amplitude pressure pulses. Experimental investigations [2–4] have shown that the shock-wave amplification occurs in a liquid saturated with bubbles of vapors or of an easily soluble gas. The amplification can occur both for a direct wave and after its reflection from a rigid boundary.

In this paper, we experimentally investigate the process of amplification of shock waves in a porous medium saturated with a liquid containing bubbles of a soluble gas, which occurs when the waves are reflected from a rigid boundary. A mechanism governing the shock-wave amplification in saturated porous media is proposed. A setup of the shock-tube type [4] was used to carry out the experiments. Its working space was filled with a porous medium saturated with water containing air bubbles that had a characteristic radius of ~50 μm. As a porous medium, we used either chaotic dumped packing of polyethylene particles having a characteristic size of 3.5 mm (porosity $m_0 = 0.37$) or soft foam plastic ($m_0 = 0.98$). Step pressure waves were generated by breaking off a membrane separating a high-pressure chamber and the working space. Pressure-wave profiles were recorded by piezoelectric pressure sensors situated along the working space. The sensors were not in contact with the porous-medium skeleton and measured pressure in the liquid phase. From the sensors, the signals were transferred to an analog-to-digital converter and then processed by a computer.

As a result of our experiments, it was shown that in the soft foam plastic saturated with water containing air bubbles, the amplitude and velocity of a shock wave reflected from a rigid wall are well described in the isothermal approximation [4, 5]. This is caused by the fact that the thermal-relaxation time of gas in the bubbles is much shorter than the duration of the wave-front time. Due to its low rigidity and high porosity, the porous skeleton does not appreciably affect the reflection of a shock wave from a rigid wall. The role of the skeleton is only technological and consists in retaining gas bubbles in liquid.

However, the situation becomes qualitatively different when a shock wave in the porous medium composed of closely packed polyethylene particles is reflected from a rigid wall. For such a shock wave, experimental values of its amplitude P_2 (dots *1* and *2*) and velocity U_2 (dots *3*) are shown in the figure as a function of the amplitude P_1 of the shock wave impinging a wall (P_0 is the initial static pressure in the liquid). The values of P_2 (curves *4* and *5*) and U_2 (curve *6*) are calculated on the basis of the isothermal model [4, 5]. The values of P_2 (curves *7* and *8*) are calculated for the reflection from a rigid wall of a complete-condensation (gas dissolving) shock wave [4, 5], C_m representing the low-frequency sonic velocity in a porous medium saturated with a liquid without gas bubbles.

It is seen that an increase in the ratio P_1/P_0 for the wave amplitude causes considerable amplification of

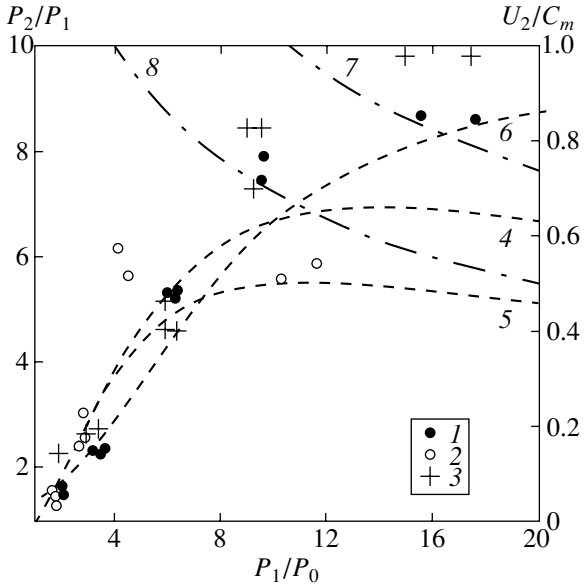

Amplitudes and velocities of a shock wave reflected from a rigid wall in a porous medium ($m_0 = 0.37$) saturated with water containing air bubbles with the initial volume gas content $\varphi_0 = 0.105$ ($P_0 = 0.103$ MPa): (*1*, *3*, *4*, *6*, *7*); and $\varphi_0 = 0.095$ ($P_0 = 0.203$ MPa): (*2*, *5*, *8*).

Kutateladze Institute of Thermal Physics, Siberian Division, Russian Academy of Sciences,
pr. Akademika Lavrent'eva 1, Novosibirsk, 630090 Russia

1028-3358/00/4508-0395$20.00

the reflected shock wave (dots *1* and *2*) compared to the isothermal calculations (curves *4* and *5*), which do not take into account gas dissolving in the liquid behind the wave. With an increase in the amplitude P_1/P_0 of the wave, the experimental data (dots *1* and *2*) approach the corresponding calculated curves (*7* and *8*) taking into account complete gas dissolving in the liquid behind the shock wave that impinges the wall. For higher initial static pressures P_0 in the medium, amplification of the amplitude of the reflected shock wave occurs at lower wave amplitudes P_1/P_0. When amplitudes of the waves grow, experimental values for the velocity of a shock wave reflected from the rigid wall (dots *3*) deviate from the calculated curve *6*. Consequently, gas dissolving occurs in the liquid behind the shock wave impinging the wall. This leads to a decrease in the volume gas content behind the wave and, therefore, to an increase in the velocity of the reflected shock wave. When the shock-wave amplitude is $P_1/P_0 > 10$, experimental values for the velocity of the reflected shock wave deviate considerably from the calculated curve. Thus, the process of dissolving gas in the liquid essentially determines the gas behavior behind the shock wave.

Hence, the availability of a dense porous medium leads to intense dissolving gas behind a shock wave and, therefore, to the amplification of the reflected shock wave. The essence of the amplification mechanism is associated with converting the kinetic energy of the liquid (i.e., the energy of its radial motion arising as a result of collapsing bubbles) into the potential energy of its pressure [1–4]. In order to realize this mechanism, it is necessary that complete dissolving (due to diffusion-caused processes) of gas contained in the bubbles would occur for a time on the order of the shock-wave leading-edge time duration. Otherwise, the regime of accelerating collapse of the bubbles, which leads to the occurrence of pressure spikes in the liquid and, consequently, to the amplification of the reflected shock wave, cannot be observed [2]. We note that the process of amplification of the reflected shock waves is not associated with splitting the bubbles behind the shock waves, as was observed when the waves evolved in a liquid with sufficiently large bubbles [4]. In our experiments, the Weber number, determining the instability and splitting of bubbles in a shock wave, is substantially smaller than its critical value.

In the experiments under consideration, an intense mass exchange behind the shock wave is caused, seemingly, by the turbulent liquid motion occurring behind the shock wave in the dense porous medium. Using both the experimental values for the amplitude and the velocity of a reflected shock wave and the model [4, 5], we have succeeded in calculating the content of the dissolved gas behind a shock wave impinging the wall and, consequently, the mass-transfer coefficient at the gas–liquid interface. It is shown that, in the soft foam plastic saturated with water containing air bubbles, diffusion processes do not noticeably vary the volume gas content behind the shock wave for time intervals under investigation $t \sim 10$ ms. At appropriate parameters of both the dense porous medium and the wave, a considerable increase in the mass exchange is observed behind the wave front. For example, for the wave amplitude $P_1/P_0 = 16.5$ at the initial stage of bubble collapsing, the mass-transfer coefficient exceeds by two orders of magnitude that calculated in the boundary-layer approximation for the diffusion regime of bubble dissolving [6, 7]. The convective mass transfer associated with the relative motion of air bubbles with respect to water is insignificant, because velocities of both phases equalize in tens of microseconds, i.e., much more rapidly than the times under investigation. Such a high increase in the mass exchange can be caused by turbulent pulsations of the velocity of the liquid, which arise in porous medium behind the shock wave. Indeed, being defined by the diameter of solid particles constituting the porous medium and also by the relative velocity of the liquid and solid phases behind the shock wave, the Reynolds number intrinsic to the process Re is rather high ($\mathrm{Re} \gg 100$). Hence, in the porous medium, the liquid flows in the turbulent regime [8]. It is noteworthy that the time of equalizing the velocities of the solid and liquid phases behind the shock wave due to interphase friction is much longer time than the shock-wave durations under investigation.

Thus, we may conclude that, for sufficiently high amplitudes ($P_1/P_0 > 30$) that propagate in a dense porous medium saturated with a liquid containing gas bubbles, the amplification effect caused by the turbulization of the motion of the liquid behind the shock-wave front occurs not only due to the reflection of the shock wave from a rigid wall but also behind the front of the direct shock wave.

REFERENCES

1. V. K. Kedrinskiĭ, Fiz. Goreniya Vzryva, No. 5, 14 (1980).
2. A. A. Borisov, B. E. Gel'fand, R. I. Nigmatulin, *et al.*, Dokl. Akad. Nauk SSSR **263**, 594 (1982) [Sov. Phys. Dokl. **27**, 237 (1982)].
3. V. E. Nakoryakov, E. S. Vasserman, B. G. Pokusaev, and N. A. Pribaturin, Teplofiz. Vys. Temp. **32**, 411 (1994).
4. V. E. Dontsov and B. G. Pokusaev, Teor. Osn. Khim. Tekhnol. **33**, 485 (1999).
5. R. I. Nigmatulin, in *Dynamics of Multiphase Media* (Nauka, Moscow, 1987), Vol. 2.
6. P. S. Epstein and M. S. Plesset, J. Chem. Phys. **18**, 1505 (1950).
7. S. S. Kutateladze and V. E. Nakoryakov, *Heat-and-Mass Exchange and Waves in Gas–Liquid Systems* (Nauka, Novosibirsk, 1984).
8. M. É. Aérov and O. M. Todes, *Hydraulic and Thermal Principles for Operation of Apparatuses with a Steady and Boiling Granular Layer* (Khimiya, Moscow, 1968).

Translated by Yu. Verevochkin

Doklady Physics, Vol. 45, No. 8, 2000, pp. 397–400. Translated from Doklady Akademii Nauk, Vol. 373, No. 4, 2000, pp. 479–482.

MECHANICS

Effect of Oriented Elastic and Strength Characteristics on the Impact Fracture of Anisotropic Materials

A. V. Radchenko and S. V. Kobenko

Presented by Academician V.E. Panin November 15, 1999

Received November 15, 1999

The small quantity of papers concerning the behavior of anisotropic materials under impact loads is an indication of the fact that this problem is far from well understood. At the same time, the anisotropic materials are finding ever-widening application, especially in connection with advanced modern technologies that make it possible to produce materials with specified properties. To ensure an optimum fitting of material properties to various structures, it is necessary to take into account the conditions (loads) under which this material operates and, based on that, to choose the necessary parameters of the material and their dependence on the orientation. Taking into account the directionality of material properties is of special importance for the structures working under extreme conditions and subjected to intense dynamic loads. These are the aircraft and spacecraft equipment, as well as containers for storage and transportation of explosive and toxic substances. In this paper, we present the model of behavior for anisotropic materials undergoing dynamic loads and study the effect of orientation-dependent properties on the impact fracture of orthotropic materials.

1. Formulation of the problem. We consider the interaction between a steel isotropic indenter in the form of a compact cylinder and an orthotropic plate made of the organoplastic material. We solve the three-dimensional problem in the Cartesian *XYZ* coordinate system. The *OZ*-axis coincides with the indenter axis, and it is opposite to the impact direction. The symmetry axes of the orthotropic material of the plate coincide with the coordinate-system axes, while the face surface of the plate coincides with the *XOY* plane at the initial moment of time. The indenter material characterized by the shear modulus, the dynamic yield strength, and the state-equation constants is modeled by an elastoplastic medium [1, 2]. The behavior of the orthotropic plate material is considered in the framework of the phenomenological approach [3–7]. The components of the stress tensor before the fracture are determined according to the generalized Hook law for the orthotropic material [6, 8] expressed through the increments and involving the components of deformation rate tensor e_{ij}. To describe the failure in the orthotropic material of the plate, we use the fourth-order tensor–polynomial strength criterion [4, 5]. It is assumed that the fracture of the anisotropic material under intense dynamic loading occurs as follows [6, 7]:

If the strength criterion [5] is violated under compression ($e_{kk} \le 0$), the material loses its anisotropic properties, and its behavior can be described by the hydrodynamic model and the material retains only the compression strength.

If criterion [5] is violated under tension ($e_{kk} > 0$), the material is considered to be destructed, and the stress-tensor components are assumed to be zero.

2. Discussion of the results. The compact cylinder of steel with dimensions $d_0 = l_0 = 15$ mm (d_0 is the diameter and l_0 is the length) runs symmetrically against the orthotropic organoplastic plate of thickness $h = 15$ mm. Cylinder velocity v_0 ranges from 700 to 1500 m/s. To find a solution, we used the finite element method [9]. The mechanical properties of the original material (material 1) of the plate obey the following relationships: $E_x > E_y > E_z$, $E_x/E_y = 2.28$, $E_x/E_z = 6.8$, $\sigma_{bx} > \sigma_{by} > \sigma_{bz}$, $\sigma_{bx}/\sigma_{by} = 2.26$, $\sigma_{bx}/\sigma_{bz} = 6.8$, where E_x, E_y, and E_z are the elastic modules and σ_{bx}, σ_{by}, and σ_{bz} are the yield strengths in the corresponding directions [5].

We obtain material 2 from the original material by rotation about the *OY*-axis by 90° assuming that there exists an elastic potential for the anisotropic material under consideration, and, thus, the relationships $E_k\nu_{ik} = E_i\nu_{ki}$, where ν_{ki} are the Poisson coefficients; $i, k = x, y, z$, are met. For material 2, in this case, we obtain the following relationships between the characteristics in the initial system of coordinates: $E_x < E_y < E_z$, $E_x/E_y = 0.34$, $E_x/E_z = 0.15$, $\sigma_{bx} < \sigma_{by} < \sigma_{bz}$, $\sigma_{bx}/\sigma_{by} = 0.33$, and $\sigma_{bx}/\sigma_{bz} = 0.15$.

In Fig. 1, we show the calculated configurations of the indenter and the plates made of materials 1 and 2 at various moments of time in the *ZOX* cross section. The regions, in which the material of the plate became

Tomsk Branch of the Institute of Structural Macrokinetics and Materials Science Problems, Russian Academy of Sciences, Tomsk, Russia

1028-3358/00/4508-0397$20.00

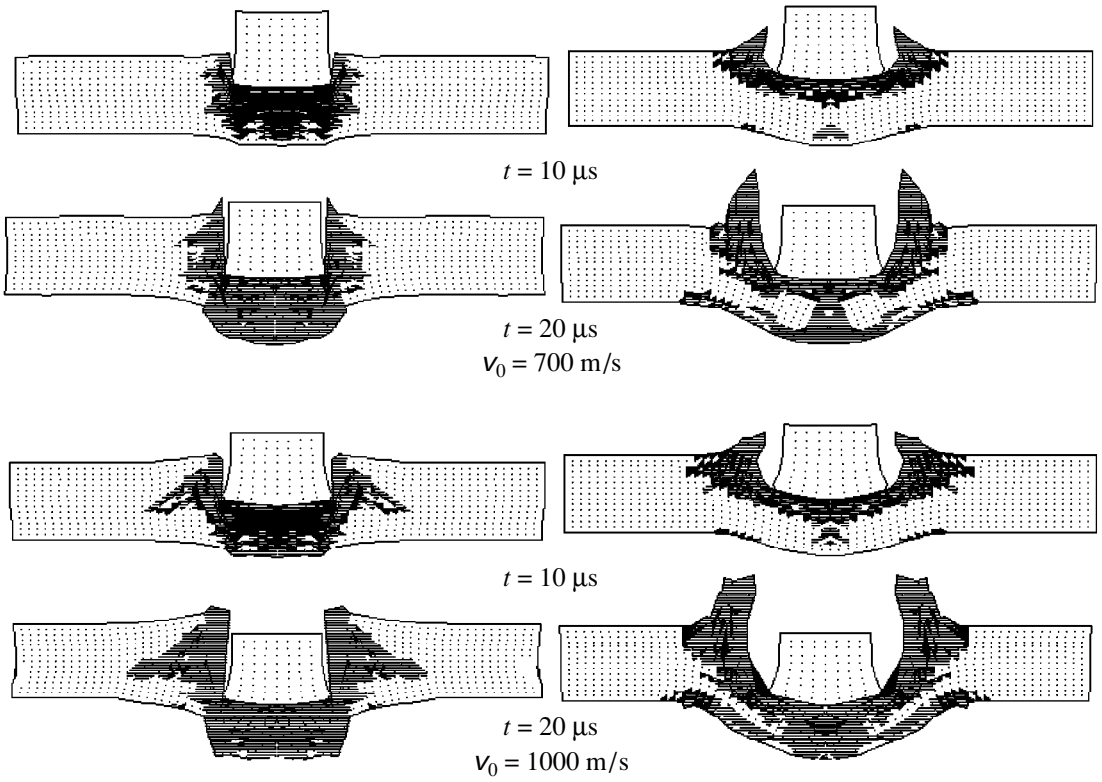

Fig. 1. Configuration of the indentor in the *ZOX* cross section. Material 1 is to the left, and material 2 is to the right.

destructed at $e_{kk} \le 0$ are completely shaded, while the regions where the fracture takes place at $e_{kk} > 0$ are hatched.

The fracture in the material of the plate starts in the compression wave initiated at the time moment corresponding to the impact. In material 1, the failure taking place in the compression wave propagates across the plate through its whole thickness. In material 2, the failure in the compression wave occurs only in the upper half of the plate, but the width of this region in the *ZOX* cross section exceeds by a factor of 1.4–1.7 (depending on the impact rate) the corresponding dimension in material 1. Such a difference can be related not only to the different strength parameters, but also by the different velocities c_i of the wave propagation in materials 1 and 2 along the corresponding directions: $i = x, y, z$.

In material 1, $c_x/c_z = 2.61$; this results in the fact that the rarefaction waves propagating from the lateral surface of the indenter and the face surface of the plate reduce the width of the compression-wave front in material 1 to a greater extent than in material 2, in which $c_x < c_z$. For material 1, the evolution of a narrow fracture zone (crack) propagating from the face surface of the plate at an angle of 45° to the *OZ*-axis is characteristic for the case of increasing impact rate. For the impact velocities to 1000 m/s, this zone does not emerge at the rear surface of the plate. With an increase in the interaction rate, the crack attains the rear surface. In material 2, owing to the fact that $c_x < c_z$, the rarefaction waves have a higher component of velocity along the z direction and, catching up with the compression wave, reduce the level of compressing stresses. The further propagation of the weakened compression wave still does not induce any failures in the material.

The analysis of wave processes in these materials can be performed in more detail using the plots (Fig. 2) of the σ_z-stress distribution over the plate thickness along the *OZ*-axis at various moments of time. The cross section $z = 0$ corresponds to the position of the plate–indenter contact surface at the moment of time $t = 0$. To 1.5 μs, the compression-wave front propagated along the z direction by $2h/3$ in material 2 and by $h/3$ in material 1. At the same time, in material 2, the rarefaction wave formed at the lateral surface of the indenter and the face surface of the plate begins to catch up with the compression wave. At 3 μs after the impact, the rarefaction wave already weakens considerably the compression wave in material 2; the highest stress in this material decreases from –3 GPa to –2.2 GPa as compared with 1.5 μs. Up to this moment in time, the regions beyond the compression-wave front in materials 1 and 2 are fractured. The further propagation of the compression wave in material 2 does not cause any fracture. On the contrary, in material 1, the fracture in the compression wave occurs across the whole thickness of the plate. Up to 4.5 μs, the compression wave in

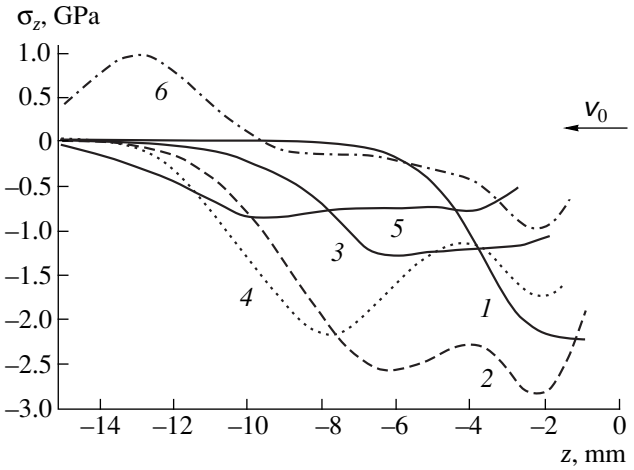

Fig. 2. Profile of the stress σ_z. Curves *1*, *3*, and *5* correspond to material 1, and curves *2*, *4*, and *6*, to material 2 at the moments of time 1.5, 3, and 4.5 μs, respectively, for v_0 = 700 m/s.

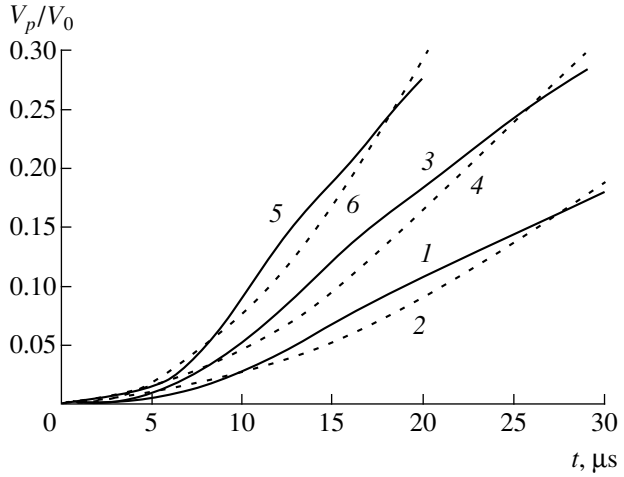

Fig. 3. Time variation of a relative volume of the fractured material for $e_{kk} > 0$. Curves *1*, *3*, and *5* correspond to material 1, and curves *2*, *4*, and *6*, to material 2 for v_0 = 700, 1000, and 1500 m/s, respectively.

material 1 only reaches the rear surface, while the rarefaction wave formed as a result of reflection of the compression wave from the rear surface of the plate already propagates along material 2. The level of compressing stresses in material 2 remaining in the upper half of the plate after the passage of the compression wave is already considerably lower (by a factor of 2–3) than that in material 1. An approximately equal level of compressing stresses in the materials is retained only close to the indenter–plate contact surface. The rarefaction wave reflected from the rear surface propagates in material 1 across the weakened substance fractured by the compression wave across the whole thickness of the plate and having only the compression strength that leads to the complete destruction of the material in front of the penetrating indenter. In material 2, the reflected rarefaction wave propagates across the undestructed substance inducing the failures of the shear-fracture type near the rear surface of the plate. The further failure in material 2 develops already not owing to the wave processes, but as a result of developing the tensile stresses in the course of penetration of the indenter.

The curves in Fig. 3 make it possible to estimate a fraction of the completely fractured material in the plate, which exhibits no resistance to the destruction. During the process of the indenter–plate interaction, a fraction of the complete failures in material 1 exceeds the corresponding value in material 2. A value of residual velocity of the indenter after piercing the plates also demonstrates that material 2 as a higher resistance to the shock fracture and penetration: For all initial impact velocities under study, a more intense deceleration of the indenter is observed during its interaction with the plate of material 2. With a decrease in the interaction rate, the difference in the indenter velocity after piercing the plate from material 1 and material 2 increases: It is 5% for v_0 = 1500 m/s, 12% for v_0 = 1000 m/s, and 20% for v_0 = 700 m/s.

Thus, the fracture of the plate made of material 1 takes place owing to and during the wave processes; it starts in the compression wave and terminates in the reflected rarefaction wave. In the plate of the material with reoriented properties (material 2), the wave processes do not cause any macroscopic fracture. The compression wave destroys the material in the upper half of the plate, while the rarefaction wave induces the shear fractures near the rear surface. The further development of the fracture in material 2 is caused by the penetration of the indenter. The fracture in material 2 demands a higher energy; i.e., only owing to a change in the orientation of properties is it possible to provide more efficient protection against the impact.

Our studies show that the anisotropy of properties is a significant factor that must be taken into account to describe and adequately predict the evolution of the shock-wave processes and the fracture in materials subjected to dynamic loadings. It was found that a change in the orientation of properties results in qualitative changes in the mechanisms of macroscopic fracture of anisotropic materials. The proposed model of fracture using the fourth-order tensor–polynomial criterion provides an opportunity to model the behavior of a wide class of anisotropic materials with various degrees of anisotropy.

ACKNOWLEDGMENTS

This work was supported by the Ministry of Education of Russian Federation according to the grant on Research in the Field of Fundamental Natural Science (item 4.3: Mechanics of Deformable Solids).

REFERENCES

1. M. L. Wilkins, in *Fundamental Methods in Hydrodynamics*, Ed. by B. Alder, S. Fernbach, *et al.* (New York, 1964; Mir, Moscow, 1967).
2. V. A. Gorel'skiĭ, A. V. Radchenko, and I. E. Khorev, Prikl. Mekh. **23** (11), 77 (1987).
3. E. M. Wu, in *Mechanics of Composite Materias*, Ed. by G. P. Sendeckyj (Academic, New York, 1974; Mir Moscow, 1978).
4. E. K. Ashkenazi, *Anisotropic Materials in Mechanical Engineering* (Mashinostroenie, Leningrad, 1969).
5. E. K. Ashkenazi and É. V. Ganov, *Anisotropy of Structural Materials: Reference Book* (Mashinostroenie, Leningrad, 1980).
6. A. V. Radchenko, Mekh. Kompoz. Mater. Konstr. **4** (4), 51 (1998).
7. A. V. Radchenko, S. V. Kobenko, I. N. Marzenyuk, *et al.*, Int. J. Impact Eng. **23**, 745 (1999).
8. S. G. Lekhnitskiĭ, *Theory of Elasticity for Anisotropic Materials* (Nauka, Moscow, 1977).
9. G. R. Johnson, J. Appl. Mech. **44** (1), 95 (1977).

Translated by V. Bukhanov

Doklady Physics, Vol. 45, No. 8, 2000, pp. 401–404. Translated from Doklady Akademii Nauk, Vol. 373, No. 4, 2000, pp. 483–486.

MECHANICS

Solving the Boltzmann Equation in the Case of Passing to the Hydrodynamic Flow Regime

F. G. Cheremisin

Presented by Academician V.V. Rumyantsev October 19, 1999

Received October 21, 1999

As the hydrodynamic regime is approached, the gas flow is usually accompanied by the formation of narrow highly nonequilibrium zones (Knudsen layers) with the characteristic size on the order of the mean free path λ for molecules. The structure of these zones is determined by fast kinetic processes. In unsteady flows, an initial layer with the time scale on the order of the mean free time $\tau_0 = \lambda/v_T$ (here, v_T is the molecular thermal velocity) occurs as well. In the macroscopic scale $l_0 \gg \lambda$, the flow parameters vary smoothly beyond these zones [1]. From a computational standpoint, solving the Boltzmann equation with steps $h_x < \lambda$ and $\tau < \tau_0$ is inefficient everywhere over the calculation domain. Moreover, it can result in the early cessation of the iterative process as soon as the error of the numerical method becomes equal to the small difference of two successive approximations. When passing to the macroscopic steps $\lambda \ll h_x < l_0$, $\tau_0 \ll \tau < t_0$, where $t_0 = l_0/v_T$, the problem of a large factor standing ahead the collision integral arises [2]. In terms of the dimensionless variables $t = t^*/t_0$, $x = x^*/l_0$, $\xi = \xi^*/v_T$ (here, the asterisk denotes dimensional variables), the Boltzmann equation takes the form

$$\frac{\partial f}{\partial t} + \xi\frac{\partial f}{\partial \mathbf{x}} = \mathrm{K}^{-1} I(f, f). \tag{1}$$

For the Knudsen numbers $\mathrm{K} \ll 1$, the equation acquires a rigid nature, and specific methods [3–5] should be used for its numerical solving.

According to the Enskog–Chapman theory, for $\mathrm{K} \ll 1$, the solution to equation (1) takes the form

$$f = f_M + \mathrm{K} f^{(1)} + \ldots, \tag{2}$$

where f_M is the Maxwell function determined by the gas density $n(x, t)$, temperature $T(x, t)$, and velocity $u(x, t)$, while

$$f_M = n(2\pi T)^{-3/2}\exp\left(-\frac{(\xi - \mathbf{u})^2}{2T}\right). \tag{3}$$

The substitution of (3) into (1), with the property $I(f_M, f_M) = 0$ taken into account, eliminates the term on the order of K^{-1} in the right-hand side of equation (2). The idea of the method proposed is to provide for the fulfillment of the indicated properties in the discrete approximation of the Boltzmann equation. In accordance with the general theory developed in [4, 5] for solving rigid equations of form (1), the solution to the difference equations obtained is constructed in such a manner that the asymptotic solution to the difference problem is of form (3) as $\tau \longrightarrow \infty$.

We write out the Boltzmann collision integral for monoatomic gas in the form

$$I(f, f) = \int_{-\infty}^{\infty}\int_{0}^{2\pi}\int_{0}^{b_m}(f' f_1' - f f_1) g b\, db\, d\varepsilon\, d\xi_1,$$

where the conventional notation of [1] is used. The velocity arguments ξ and ξ_1 of the functions f and f_1 are related to the arguments ξ' and ξ_1' of the functions f' and f_1' by the relations

$$\xi' = \xi + \mathbf{n}(\mathbf{ng}), \quad \xi_1' = \xi_1 - \mathbf{n}(\mathbf{ng}). \tag{4}$$

Here, $\mathbf{n}$ is the unit vector aligned with the centerline of the colliding molecules, and $\mathbf{g} = \xi - \xi_1$ is their relative velocity.

We consider the integral operator

$$Q(\phi) = \frac{1}{4}\int_{-\infty}^{\infty}\int_{-\infty}^{\infty}\int_{0}^{2\pi}\int_{0}^{b_m}(\phi(\xi) + \phi(\xi_1) - \phi(\xi') - \phi(\xi_1'))$$
$$\times (f' f_1' - f f_1) g b db d\varepsilon d\xi d\xi_1. \tag{5}$$

Taking the three-dimensional δ-function $\delta(\xi - \xi_\beta)$ for $\phi(\xi)$, we obtain

$$I_\beta = Q(\delta(\xi - \xi_\beta)). \tag{6}$$

The laws of conservation for mass (density), momentum, and energy $Q(\psi) = 0$ follow from (5) for the additive collision invariants $\psi = (1, \xi, \xi^2)$.

We bound the space of the ξ-variable by the region Ω with a volume V and introduce in this region a net

Computer Center, Russian Academy of Sciences, ul. Vavilova 30/6, Moscow, 117900 Russia

1028-3358/00/4508-0401$20.00

consisting of N_0 equidistant nodes ξ_β with a step $\mathbf{h} = (h_1, h_2, h_3)$. Furthermore, the following notation is used: $f_\beta \equiv f(\xi_\beta, x, t)$, $I_\beta \equiv I(\xi_\beta, x, t)$. Here, only the node of the velocity net is indicated at which a given value is calculated. Equation (1) will be approximated by a system of N_0 equations in terms of the functions f_β. From (6) and (5), a cubature formula for calculating the integral I_β is constructed, which satisfies, as in the method [6, 7], the conservation laws

$$\sum_\beta \psi_\beta I_\beta = 0, \quad \psi_\beta = (1, \xi_\beta, \xi_\beta^2), \tag{7}$$

as well as the condition

$$I_\beta(f_{M,\beta}, f_{M,\alpha}) = 0 \tag{8}$$

at any node ξ_β of the velocity net. Here, $f_{M,\beta}$ is the magnitude of function (3) at the node ξ_β.

We employ a uniform cubature net ξ_{α_ν}, ξ_{β_ν}, b_ν, ε_ν with N_ν nodes, such that ξ_{α_ν} and ξ_{β_ν} belong to the velocity net. Then, we exclude those values of the integration variables b, ε that remove the velocities ξ'_{α_ν} and ξ'_{β_ν} after the collision beyond the region $\Omega \times \Omega$. Since the arguments ξ'_{α_ν} and ξ'_{β_ν} of the δ-functions appearing in (5) with negative sign, in general, do not coincide with the net nodes, these functions will be approximated by the sum of δ-functions with arguments taken at nodes nearest to ξ'_{α_ν} and ξ'_{β_ν}.

We assume that ξ_{λ_ν} and ξ_{μ_ν} are the nearest nodes to ξ'_{α_ν} and ξ'_{β_ν}, respectively; $\Delta_{\lambda_\nu} = \xi'_{\alpha_\nu} - \xi_{\lambda_\nu}$ and $\Delta_{\mu_\nu} = \xi'_{\beta_\nu} - \xi_{\mu_\nu}$. From (4), it follows that the points ξ'_{α_ν} and ξ'_{β_ν} are situated antisymmetrically in the corresponding cells: $\Delta_{\lambda_\nu} = -\Delta_{\mu_\nu}$. We denote $\Delta = \Delta_{\lambda_\nu}/h = (\Delta_1, \Delta_2, \Delta_3)$, $|\Delta_i| \le 1/2$, $i = 1, 2, 3$, and introduce a displacement vector on the net $\mathbf{s} = (s_1, s_2, s_3)$, $s_i = 0$, or $s_i = \mathrm{sgn}(\Delta_i)$, $i = 1, 2, 3$. Then, the vertices of the cells, inside of which the points ξ'_{α_ν} and ξ'_{β_ν} fall, can be represented as $\xi_{\lambda_\nu + s}$ and $\xi_{\mu_\nu - s}$.

We replace the off-net δ-functions in (5) by the expansions

$$\delta(\xi_\beta - \xi'_{\alpha_\nu}) = \sum_s p_s \delta(\xi_\beta - \xi_{\lambda_\nu + s}),$$

$$\delta(\xi_\beta - \xi'_{\beta_\nu}) = \sum_s p_s \delta(\xi_\beta - \xi_{\mu_\nu - s}).$$

Substituting these expansions into (5) and using (6), we obtain

$$I_\beta = B\sum_\nu^{N_\nu}\left(-j_\nu^{(1)} + j_\nu^{(2)} + \sum_s p_{\nu,s}(j_\nu^{(3)} + j_\nu^{(4)})\right), \tag{9}$$

where $B = V\pi b_m/4N_\beta$, $N_\beta = N_\nu/N_0$, $j_\nu^{(1)} = f_{\alpha_\nu} f_{\beta_\nu} g_\nu b_\nu$, $j_\nu^{(2)} = f'_{\alpha_\nu} f'_{\beta_\nu} g_\nu b_\nu$ for $\alpha_\nu = \beta$ or $\beta_\nu = \beta$, and $j_\nu^{(3)} = f_{\alpha_\nu} f_{\beta_\nu} g_\nu b_\nu$, $j_\nu^{(4)} = f'_{\alpha_\nu} f'_{\beta_\nu} g_\nu b_\nu$ for $\lambda_\nu + s = \beta$ or $\mu_\nu - s = \beta$.

We determine the coefficients p_s from conservation laws (7). To this end, we substitute (9) into (7), change the order of summation, and require each term with the index ν in the external sum to vanish. Thus, we arrive at the same system of equations that has been obtained in [6] when constructing a conservative method for the collision integral with "inverse collisions" ignored, i.e., without the term $f'_{\alpha_\nu} f'_{\beta_\nu}$ in (5), namely,

$$1 - \sum_s p_{\nu,s} = 0, \tag{10a}$$

$$\xi_{\alpha_\nu} + \xi_{\beta_\nu} - \sum_s p_{\nu,s}(\xi_{\lambda_\nu + s} + \xi_{\mu_\nu - s}) = 0, \tag{10b}$$

$$\xi_{\alpha_\nu}^2 + \xi_{\beta_\nu}^2 - \sum_s p_{\nu,s}(\xi_{\lambda_\nu + s}^2 + \xi_{\mu_\nu - s}^2) = 0. \tag{10c}$$

System (10) of equations has a particular solution containing only two nonzero coefficients: The first is $1 - p_\nu$ and corresponds to $\mathbf{s} = 0$. The second is p_ν and corresponds to a certain value $\mathbf{s} \neq 0$, which depends on a combination of parameters entering into the energy equation. Thus, we arrive at the approximation

$$\begin{aligned} I_\beta = B\sum_\nu^{N_\nu}(&-j_\nu^{(2)} + j_\nu^{(1)} + p_\nu(j_{\nu,0}^{(3)} - j_{\nu,0}^{(4)}) \\ &+ (1 - p_\nu)(j_{\nu,s}^{(3)} - j_{\nu,s}^{(4)})). \end{aligned} \tag{11}$$

The value of $f'_{\alpha_\nu} f'_{\beta_\nu}$ entering into $j_\nu^{(2)}$, $j_{\nu,0}^{(4)}$, and $j_{\nu,s}^{(4)}$ should be found from interpolation of the nearest values $f_{\lambda_\nu + s}$, $f_{\mu_\nu - s}$. From (10c), it follows that the formula

$$\begin{aligned} \ln(f'_{\alpha_\nu} f'_{\beta_\nu}) = &(1 - p_\nu)\ln(f_{\lambda_\nu} f_{\mu_\nu}) \\ &+ p_\nu \ln(f_{\lambda_\nu + s} f_{\mu_\nu - s}) \end{aligned} \tag{12}$$

is exact for a net function of the type (3), and it makes each term of sum (11) vanish.

Formulas (11) and (12) specify the method to calculate the collision integral ensuring the rigorous fulfillment of conditions (7) and (8).

Equation (1) is solved on the basis of the decomposition method. In the interval $[t^j, t^{j+1}]$, the following

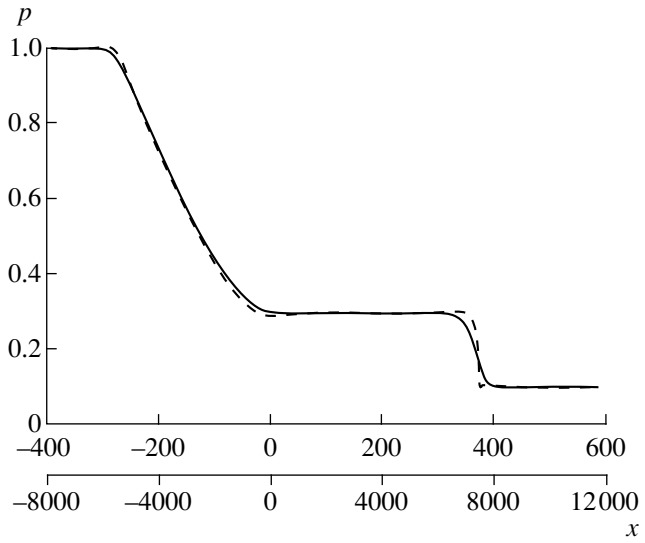

Fig. 1.

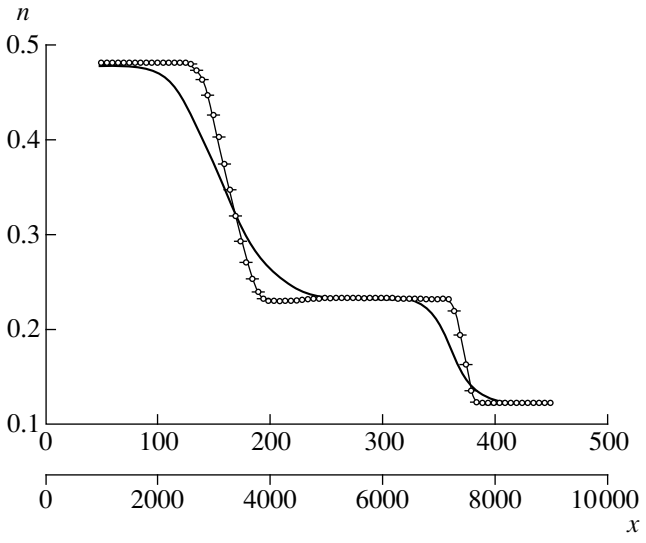

Fig. 2.

equations are sequentially solved

$$\frac{\partial f_\beta^*}{\partial t} + \xi_\beta \frac{\partial f_\beta^*}{\partial x} = 0, \quad f_\beta^{*,j} = f_\beta^j, \tag{13}$$

$$\frac{\partial f_\beta}{\partial t} = \mathrm{K}^{-1} I_\beta, \quad f_\beta^j = f_\beta^{*,j+1}. \tag{14}$$

The system of equations (13) is approximated by the scheme [8] having the second order of accuracy in h_x, which is well adapted to calculating discontinuous flows. For solving the system of nonlinear equations (14), we introduce the discrete variable $t_\nu = \tau\nu/N_\nu$, $\tau = t^{j+1} - t^j$ and the intermediate values of the solution $f_\beta^{j+\nu/N_\nu}$; then, we employ the explicit Euler method

$$f_\beta^{j+\nu/N_\nu} = f_\beta^{j+(\nu-1)/N_\nu} + \tau\mathrm{K}^{-1}B(-j_{\nu-1}^{(1)} + j_{\nu-1}^{(2)} + (1-p_{\nu,0})(j_{\nu-1,0}^{(3)} - j_{\nu-1,0}^{(4)}) + p_{\nu,s}(j_{\nu-1,s}^{(3)} - j_{\nu-1,s}^{(4)})). \tag{15}$$

Here, the values $j_{\nu-1}^{(1)}, j_{\nu-1}^{(2)}, \ldots$ are calculated from the functions $f_\beta^{j+(\nu-1)/N_\nu}$. Method (15) is conservative and enables the verification of the positive value of the solution. The solution to system (14) is attained for $\nu = N_\nu$. It is correct at arbitrary values of τ and tends to (3) as $\tau \longrightarrow \infty$. On substituting the net function in form (3), equation (13) becomes equivalent to the kinetic approach for solving equations of gas dynamics [5].

The method proposed allows us to solve the Boltzmann equation with both the separation of the Knudsen layers (that must be calculated with steps $\tau < \mathrm{K}^{-1}$, $h_x < \mathrm{K}^{-1}$) and without such a separation (with steps $\tau > \mathrm{K}^{-1}$, $h_x > \mathrm{K}^{-1}$) over the entire calculation domain. In the latter case, as for calculating hydrodynamic equations, highly nonequilibrium zones manifest themselves as discontinuities of hydrodynamic parameters, which are spread by the scheme viscosity.

As the first example, the well-known one-dimensional nonstationary problem of propagation of an arbitrary initial-data discontinuity was considered, which is often used as a test for numerical methods of gas dynamics. The initial data (at $t = 0$) are the following: To the left of the discontinuity point $x = x_0$, gas is characterized by the parameters $n_1 = 1$, $T_1 = 1$, $U_1 = 0$. To the right of the discontinuity point, it has the parameters $n_2 = 0.125$, $T_2 = 0.8$, $U_2 = 0$. The Boltzmann equation was solved for the hard-sphere molecule model with the following values for discretization parameters in the ξ-variable: $N_0 = 3604$, $N_\nu = 36000$, $h_1 = h_2 = h_3 = 0.3v_T$, and with various values of h_x and τ.

Figure 1 shows the pressure plots for the cases $h_x = 5\lambda_1$, $\tau = 0.2\tau_1$ and $h_x = 100\lambda_1$, $\tau = 3\tau_1$. Here, λ_1 is the mean free path and τ_1 is the mean free time to the left of the initial discontinuity. The number of nodes for both cases is equal to $k_x = 200$. The initial discontinuity is located at x_0. The solution corresponds to $t = 200\tau_1$ and $t = 4000\tau_1$ for the first and second cases, respectively. Since the solution to the gas-dynamic problem is invariant with respect to the transformation $x' = cx$, $t' = ct$, the plots are rather close. However, in the first case, a shock-wave structure is visible, whereas it is a discontinuity for the second case. The solutions in the case of the rarefaction wave are close, and they essentially coincide in the contact region. Figure 2 shows the density plots to the right of the rarefaction wave in an enlarged scale. In the first calculation (solid line), the contact discontinuity and the shock wave are spread out by molecular viscosity. The shock-wave thickness is approximately equal to $5\lambda_2$, where λ_2 is the mean free path to the right of the initial discontinuity; this magnitude corresponds to the actual value for the given Mach

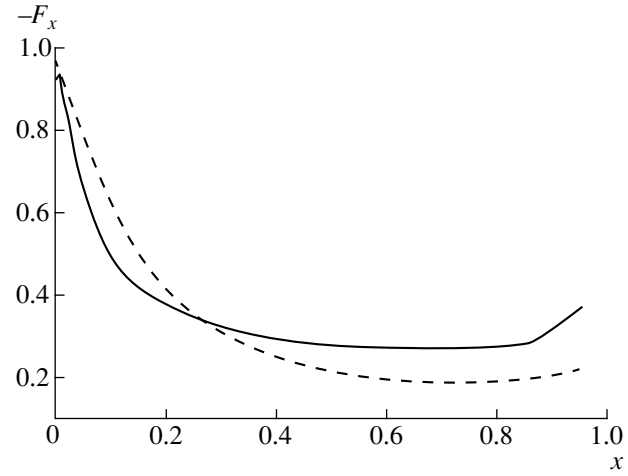

Fig. 3.

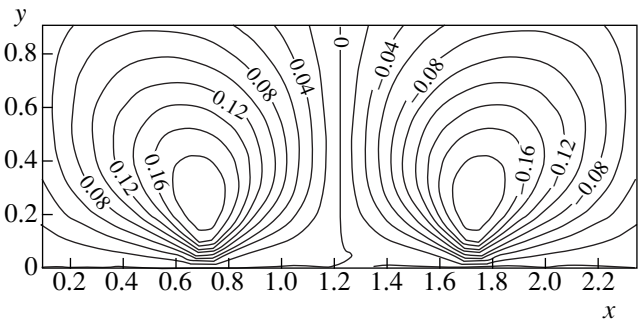

Fig. 4.

number M = 1.62. In the second case (shown by circles), gas-dynamic discontinuities are spread by the viscosity over a few cells.

As for the second example, we consider a longitudinal flow around a plane-parallel plate of the infinite swing for M = 2 and K = 0.01 in the case of the surface temperature equal to that of the approach stream and diffuse reflection of molecules from the surface at the condition of total accommodation. For such flow parameters, the Knudsen layer with the thickness on the order of λ is known [1] to be formed near the plate surface. At the same time, a region with abrupt longitudinal flow changes at a distance on the order of λ is formed near the leading edge. Accurate calculation of the flow requires that the steps of a three-dimensional net in the regions indicated would be smaller than λ. These conditions are met in the first calculation, where the varied net in x and y with the steps $h_x = 0.6\lambda$ and $h_y = 0.6\lambda$ was used near the leading edge and surface, respectively. The numbers of nodes in x and y were $k_x = 54$ and $k_y = 32$, respectively; the steps h_x and h_y attained 20λ at the periphery of the calculation region. The other discretization parameters are the following: $\tau = 0.35\tau_0$, $N_0 = 3604$, $N_v = 36000$, and $h_1 = h_2 = h_3 = 0.32v_T$. Here, λ is the mean free path, and τ_0 is the mean free time in an unperturbed flow. In the second calculation, the Knudsen layers were not separated, and a net with a constant step $h_x = h_y = 5\lambda$, $k_x = 43$, $k_y = 22$ was employed, the other parameters being the same as before. In both cases, the calculations were carried out up to $t = 200\tau_0$, and the attainment of the steady-state solution was controlled. Figure 3 shows the plots for the friction along the plate obtained in the first case (solid line) and in the second one (dashed line). The separation of the Knudsen layers is seen to play a significant role.

The third example shows the efficiency of the method for calculating slow flows. A flow similar to that of the second example is considered but with M = 0.001 and K = 0.1. The parameters of the calculation are the following: $h_x = 0.5\lambda$, $h_y = 0.333\lambda$, $k_x = 40$, $k_y = 20$, $\tau = 0.1$, $N_0 = 3604$, $N_v = 36000$, and $h_1 = h_2 = h_3 = 0.26v_T$. In this case, the deviation from the equilibrium is determined by the parameter $K_{eff} = M \times K = 10^{-4}$, and an especially high accuracy is required. Isolines of the gas-velocity component normal to the plate (in the 1000-fold scale) are shown in Fig 4. The plate is situated between $x_1 = 0.7$ and $x_2 = 1.7$. In the case of using the method of [6, 7], attempts to calculate these small deviations from the equilibrium even for M = 0.01 and with a tenfold increase in the parameter N_v turned out unsuccessful.

The examples given above show that the method proposed allows the gas flows with the Knudsen numbers $K \ll 1$ to be efficiently calculated.

ACKNOWLEDGMENTS

This study was supported by the Russian Foundation for Basic Research, project no. 98-01-00443.

REFERENCES

1. M. D. Kogan, *Dynamics of Rarefied Gas* (Nauka, Moscow, 1967).
2. V. A. Rykov, in *Modern Problems in Computational Aerodynamics* (Mir, Moscow, 1991), pp. 377–395.
3. F. Coron and B. Perthame, SIAM (Soc. Ind. Appl. Math.) J. Numer. Anal. **28**, 26 (1991).
4. S. Jin, J. Comput. Phys. **122**, 51 (1995).
5. R. Gaflisch, S. Jin, and G. Russo, SIAM (Soc. Ind. Appl. Math.) J. Numer. Anal. **34** (1), 246 (1997).
6. F. G. Cheremisin, Dokl. Akad. Nauk **357**, 53 (1997) [Phys.–Dokl. **42**, 607 (1997)].
7. F. G. Tcheremissine, in *Proceedings of the XX International Symposium on Rarefied-Gas Dynamics* (Peking Univ. Press, Beijing, 1997), pp. 297–302.
8. J. P. Boris and D. L. Book, J. Comput. Phys. **11**, 38 (1973).

Translated by V. Tsarev

Doklady Physics, Vol. 45, No. 8, 2000, pp. 405–409. Translated from Doklady Akademii Nauk, Vol. 373, No. 5, 2000, pp. 618–622.

MECHANICS

An Isobaric–Isothermal Ensemble in Statistical Mechanics

K. M. Magomedov

Presented by Academician I.I. Novikov November 10, 1999

Received July 6, 1999

The isobaric–isothermal ensemble is rarely used in statistical mechanics and thermodynamics due to difficulties with integration and some other computational problems [1–4]. Nevertheless, this ensemble provides certain advantages related to rapid convergence with respect to the number of particles [5]. The canonical and grand canonical distributions are the most popular, since they ensure exact solutions for ideal gas and harmonic oscillators.

At first glance, it seems that the problem could be solved by means of the expansion of thermodynamic potential $\Omega = -pV$ in terms of chemical potential μ and the group integrals for interacting particles [1, 2]. However, the mathematical formalism of such a type does not provide an opportunity to explicitly obtain a final result. First, it is possible to calculate only about ten first terms in the series expansion without any proofs of its convergence. Second, this approach is based on model potentials for two-particle interactions with the parameters refined by fitting to experimental data. Third, we also need to derive the inverse function by expressing μ through measured temperature T and pressure p.

In this paper, we demonstrate that precisely the ensemble corresponding to constant pressure underlying the Gibbs free-energy distribution turns out to be free of many disadvantages inherent in other ensembles. Our approach starts from clear basic principles: The mathematical models considered in statistical mechanics serve as approximations to real physical systems [1], and the actual accuracy of the models is determined by phenomenological thermodynamics in the broad understanding of the term [6]. The latter enables us, in particular, to extrapolate the available experimental data using the theory of similarity.

Here, we suggest a new approach for interpreting the constant-pressure ensemble based on the quantum-mechanical concepts. In the one-particle approximation, we derive an expression for the Gibbs free energy depending on the number of particles, temperature, pressure, and on several typical values of enthalpy. The limiting cases correspond to the Debye theory for heat capacity of solids and to the chemical potential of ideal gas. Note that in the latter case, the mean volume per particle tends at $T \longrightarrow 0$ to its value in the condensed state. This equation of state is in good agreement with the experimental data.

1. **The modified constant pressure ensemble** can be obtained directly from the Meyer definition of probability [1]

$$W(\mathcal{H}) = e^{\beta[G - NpV(\mathcal{H}) - E(N, V, \mathcal{H})]}, \quad (1)$$

where $\beta = (kT)^{-1}$; E and V are the energy and the volume, respectively; $G = G(\beta, p, N)$ is the Gibbs free energy; and $\mathcal{H}$ are the characteristic quantum numbers of the system.

The conventional approach involving the summation over possible $\mathcal{H}$ and the integration over volume leads to the relationship

$$-\beta G = \ln\int_0^\infty Z(\beta, N, V)d\left(\frac{V}{V_*}\right), \quad (2)$$

where Z is the partition function of the canonical ensemble. The physical meaning of small volume V_* is not quite clear, and it is possible to eliminate it using the following expression (see [1]):

$$-\beta G = \ln\int_0^\infty Z(\beta, N, V)d(\beta pV). \quad (3)$$

Nevertheless, expressions (2) and (3) imply a physical paradox: We need to know $Z(\beta, N, V)$ for the case of $N \sim 10^{24}$ particles confined within a small volume of the order of 10^{-24} cm^3. On the other hand, even for ideal gas occupying a macroscopic volume, partition function Z calculated in the usual way is valid under conditions

Institute of Geothermal Problems,
Dagestan Scientific Center, Russian Academy of Sciences,
pr. Kalinina 39a, Makhachkala, 367003 Russia

1028-3358/00/4508-0405$20.00

$$v^{1/3} \ll l = \frac{1}{n\sigma} = \frac{V}{N\sigma}, \quad N \ll \frac{V^{2/3}}{\sigma} \sim 10^{16},$$

where l is the mean free path and σ is the cross section for collisions between particles. Note that $N \sim 10^{19}$ for ideal gas under normal conditions. However, with account taken for particle collisions, we obtain quite a different picture. Let us perform a Gedanken experiment by tracing the motion of a chosen particle in the gas of hard spheres of the radius $\sigma^{1/2}$ during a macroscopic time interval. Let n_1 be the number of particles with the free path $\sigma^{1/2}$, n_2 being that with a free path twice as large, etc. Similar results could be obtained if we use the ergodicity postulate to calculate the number of particles with free paths equal to $\sigma^{1/2}, 2\sigma^{1/2}, 3\sigma^{1/2}, \ldots$. This implies that, even in classical mechanics, we can pass to the statistical description of a system with discrete values of volume treating $n_1, n_2, n_3, \ldots$ as mean numbers of particles in volumes $\sigma^{3/2}, 2\sigma^{3/2}, 3\sigma^{3/2}, \ldots$.

The above discussion becomes more evident and clearer if we start *a priori* from the quantum-mechanical approach, where the state of a system (subsystem) is described by a wave function parametrically dependent on the volume. For example, for a free particle confined within the volume v_ν, we have

$$\mathcal{E}_n = \frac{\pi^2\hbar^2 n^2}{2m v_\nu^{2/3}}.$$

Now, let us consider a set of weakly interacting subsystems, with a large number of particles in each of them. If the long-range forces are absent and the surface effects are negligible, the system as a whole can be described by wave function $\Psi = \prod_\nu \psi_\nu$ and by the corresponding relationships $N = \sum N_\nu$, $V = \sum N_\nu v_\nu$, $H_\nu = \sum [pN_\nu v_\nu + E(N_\nu, V_\nu, \mathcal{H})]$. Performing the summation over $\mathcal{H}$ in (1), we get

$$W(N_\nu) = e^{\beta\left(G - p\sum_\nu N_\nu v_\nu\right)} Z(\beta, N_\nu, v_\nu).$$

Then, summing over $N_\nu = 0, 1, 2$, etc., and taking into account that the sum over all probabilities is equal to unity, we obtain

$$e^{-\beta G} = \sum_{\sum N_\nu = N} \cdots \sum e^{-\beta p \sum N_\nu v_\nu} Z(\beta, N_\nu, v_\nu) = \sum \cdots \sum Y(\beta, p, N_\nu). \quad (4)$$

It should be emphasized that N_ν is the mean number of particles occupying volume $V_\nu = N_\nu v_\nu$; $Z(\beta, N_\nu, V_\nu)$ is the partition function of canonical ensemble, whereas $Y(\beta, p, N_\nu)$ is the constant-pressure partition function. The latter is evidently related to the Gibbs free energy and enthalpy. Note that $H = \frac{\partial \beta G}{\partial \beta}$, and the similar formula relates the Helmholtz free energy and internal energy.

Relationship (4) refines (1) by eliminating physically improbable and nonessential states. To simplify the problem further on, we assume

$$Z(\beta, N_\nu, V_\nu) = z_\nu^{N_\nu}, \quad Y(\beta, p, N_\nu) = y_\nu^{N_\nu},$$

where $z_\nu = z_\nu(\beta, v_\nu)$ and $y_\nu = y_\nu(\beta, p)$. Actually, this means that we consider only the normal systems [8]. Below, we present a method allowing us to calculate z_ν and y_ν. Here, we use the one-particle approximation to determine statistical weights for identical particles distributed over volumes V_ν. Let M_ν be the maximum number of particles occupying the νth spatial subset in such a way that N_ν cells contain one particle and the remaining $M_\nu - N_\nu$ cells are empty. As a whole, there exist $M_\nu!$ ways to distribute these particles, but the exchange of particles between the occupied cells and the rearrangement of empty cells do not affect the value of energy (enthalpy) determined by the summation in (4). Hence, the weight factor for the νth layer is $W_\nu = M_\nu!(N_\nu!(M_\nu - N_\nu)!)$. To determine M_ν and the common weight factor, we can imagine the following experiment. Let us assume that all N particles are in the ground state at $T = 0$ and each of them occupies a volume v_0. The system is heated at $p = \text{const}$ (under a movable piston). Then, some of the particles would leave the ground state and occupy other levels. It is possible to consider the state where N particles leave the ground state and occupy a single νth layer. Then, it is evident that $M_\nu = N$. While additional conditions are not specified, all layers are independent and the total weight is $W = \prod_{\nu=1} W_\nu$. The special role of the ground state is taken into account by condition $W_0 = 1$. In the case of $N_2 = N_3 = \ldots = 0$, this corresponds to the well-known examples of solving similar problems in statistical physics [8]. The physical meaning of this condition is the absence of additional contribution to entropy related to N_0 particles.

Thus, it is necessary to calculate the sum

$$e^{-\beta G} = \sum_{\sum N_\nu = N} \cdots \sum e^{N_0 y_0} \prod_{\nu=1} \frac{M_\nu!}{N_\nu!(M_\nu - N_\nu)} e^{N_\nu \ln y_\nu}. \quad (5)$$

Let us employ the well-known method of statistical physics that allows us to calculate similar sums based on the maximum term [1]. We add condition $C(N - \sum N_\nu)$ to (5) and find variations δN_ν using the Stirling formula for factorials. Then, we find

$$\ln y_0 + C = 0,$$
$$\ln y_\nu - \ln N_\nu + (N - N_\nu)\ln(N - N_\nu) + C = 0.$$

Unfortunately, in the literature, insufficient attention is payed to the ground state, i.e., to the first condition. As a result, parameter C corresponding to the particle number conservation is not eliminated from the distribution. This makes the problem much more complicated and changes the distribution type. For example, if we retain C (actually, the chemical potential), we would deal with the so-called generalized ensemble [2].

Eliminating C, we obtain the desired distribution

$$\frac{N_\nu}{M_\nu} \equiv \frac{N_\nu}{N} = \frac{y_\nu}{y_0 + y_\nu}, \quad \nu = 1, 2, 3, \ldots,$$
$$\frac{N_0}{N} = 1 - \sum_{\nu=1} \frac{y_\nu}{y_0 + y_\nu}. \tag{6}$$

Taking (6) into account, the maximum exponent in (5) has the form

$$N_\nu \ln\frac{y_\nu}{y_0} + N\ln\frac{N}{N - N_\nu} + N_\nu \ln\frac{N - N_\nu}{N_\nu} = N\ln\left(1 + \frac{y_\nu}{y_0}\right).$$

Thus, the desired expression for the Gibbs potential is

$$-\beta G = N\left[\ln y_0 + \ln\prod_{\nu=1}\left(1 + \frac{y_\nu}{y_0}\right)\right]. \tag{7}$$

2. Partial statistical sums in (7). If we take ψ_ν as a sum of symmetrized products of one-particle wave functions, then the enthalpy of the system with particles occupying volumes v_ν can be written in the form

$$H_\nu = \sum_i (pv_i + \varepsilon_i^\nu) n_i^\nu, \quad \sum_i n_i^\nu = N_\nu.$$

Then, for bosons, we have [9]

$$Y_\nu = \sum_{M_i^\nu} \cdots \sum \prod_i \frac{(n_i^\nu + g_i^\nu - 1)!}{n_i^\nu!(g_i^\nu - 1)!} e^{-\beta(pv_\nu + \varepsilon_i^\nu)n_i^\nu}, \tag{8}$$

where ε_i^ν are the one-particle energy levels, numbers n_i^ν specify the quantum state of the system, and g_i^ν is the number of states at the ith level, with $g_0^\nu = N_\nu$. We estimate the sum based on the maximum term approximation. Repeating exactly the same procedure as in Section 1, we obtain

$$Y_\nu = e^{-\beta(pv_\nu + \varepsilon_0^\nu)N_\nu} e^{-N_\nu \sum_i \bar{g}_i^\nu \ln(1 - e - \beta\bar{\varepsilon}_i^\nu)}$$
$$= e^{-\beta h_\nu^0 N_\nu} Z_\nu(\beta, N_\nu),$$

or, in terms of y_ν (z_ν),

$$y_\nu = e^{-\beta h_\nu^0} z_\nu, \quad z_\nu = e^{-\sum_i \bar{g}_i^\nu \ln\left(1 - e^{-\beta\bar{\varepsilon}_i^\nu}\right)},$$
$$\bar{\varepsilon}_i^\nu = \varepsilon_i^\nu - \varepsilon_0^\nu. \tag{9}$$

Since each particle moves inside its own volume v_ν, the phase volume can be calculated for one particle and multiplied by N_ν: $g_i^\nu = N_\nu \bar{g}_i^\nu$. For free particles, we have by definition [1, 9]

$$\bar{g}_i^\nu = \sum_{v_\nu \le v \le v_{\nu+1};\ \varepsilon_i \le \varepsilon \le \varepsilon_{i+1}} 1 = (v_{\nu+1} - v_\nu)\frac{4\pi}{h^3} P^2 dP.$$

Correspondingly, keeping the linear terms in z_ν, we obtain

$$z_\nu = \prod_i \left(1 - e^{-\beta\bar{\varepsilon}_i^\nu}\right)^{-\bar{g}_i^\nu} = \sum_i \bar{g}_i^\nu e^{-\beta\varepsilon_i^\nu}$$
$$= \frac{(v_{\nu+1} - v_\nu)}{h^3} Y\pi \int_0^\infty P^2 e^{-\beta P^2/2m} dP = \frac{v_{\nu+1} - v_\nu}{\Lambda^3}, \tag{10}$$
$$\Lambda = \left(\frac{h^2}{2\pi m k T}\right)^{1/2},$$

where Λ is the thermal de Broglie wavelength. In the general case, when a particle moves in effective potential field $u(r)$, and $P = \sqrt{2m(\varepsilon - u)}$, we find

$$\bar{g}_i^\nu = \frac{4\pi m \Delta\varepsilon}{h^3} \int_{v_\nu}^{v_{\nu+1}} r^2 \sqrt{2m(\varepsilon - u)}\, dr. \tag{11}$$

For the harmonic oscillator ($u = m\omega^2 r^2/2$, $\bar{\varepsilon}_i = \omega\hbar i$), simple calculations give $\bar{g}_i^\nu = i^2/2$. At large i, it coincides with the exact quantum-mechanical result $(i + 1)(i + 2)/2$. This example demonstrates that, in the general case, we should use expression (11) to determine z_ν.

Measuring energies ε_i^ν from ε_0^0 and the volume from v_0, we divide (7) by N and find the expression for chemical potential taking into account (9),

$$\mu = h_0^0(p) - kT\left[\ln z_0 + \ln\prod_{\nu=1}(1 + e^{-\beta h_\nu^0 z_\nu / z_0})\right], \tag{12}$$
$$h_\nu^0 = p(v_\nu - v_0) + \varepsilon_\nu^0.$$

Differentiating (12) with respect to p, we obtain the

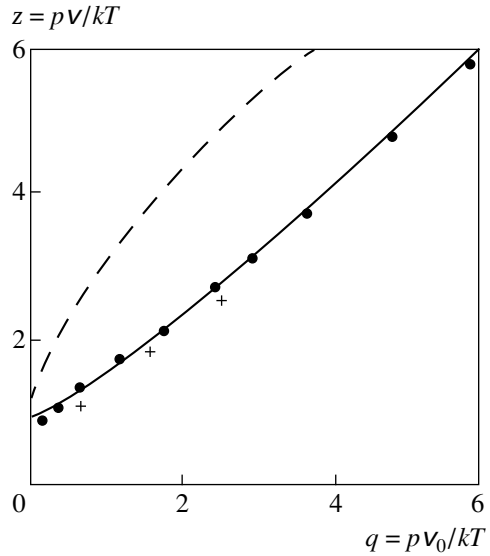

Figure.

mean volume per particle,

$$\bar{v} = v_0 + \sum_{\nu=1} \frac{v_\nu - v_0}{e^{\beta h_\nu^0 - \ln(z_\nu/z_0)} + 1} = v_0 + \sum_\nu \frac{N_\nu}{N}(v_\nu - v_0). \quad (13)$$

As should be expected, this expression demonstrates that $\bar{v} = v_0(p)$ at $\beta \longrightarrow \infty$. Thus, we get the equation for a zero isothermal curve, which can be derived based on the method of differential virial relationships [10]. In addition, a stepwise change of $\bar{v}$ occurs at temperatures corresponding to a zero argument of exponentials in the denominator of (13) (this recalls the behavior of the well-known Fermi–Dirac distribution) [1, 8]. This is an indication of phase transitions, and the summation in (12) and (13) demands certain care and calls for further analysis.

Distribution (12) cannot be treated as closed while h_ν^0 and v_ν are unspecified. To begin with, we consider three examples.

The first example is the heat capacity of solids. Let us assume that $N_\nu/N \ll 1, \nu = 1, 2, 3, \ldots$. Then, according to (9) and (12), we have

$$\mu = h_0^0(p) + kT \sum_{n=0} \frac{n^2}{2} \ln(1 - e^{-\beta\omega\hbar n}). \quad (14)$$

Differentiating (14) with respect to T, we obtain s. After subsequent differentiation with respect to $\ln T$ and replacing the summation by integration, we find the following expression for the heat capacity of a solid with $\bar{v} = v_0$:

$$c_p = \frac{k}{2} b^2 \int_0^{n_*} \frac{n^4 e^{bn} dn}{(e^{bn} - 1)^2}, \quad b = \frac{\hbar\omega}{kT} = \frac{\vartheta_D}{T}. \quad (15)$$

At $n_* = (24)^{1/3} = 2.884$, expression (15) coincides exactly with the well-known Debye formula [1], but not with the Einstein formula, as one could expect. This can be simply explained: Einstein considered the vibrations in the whole $N\bar{v}_0$ volume, rather than vibrations within each elementary volume v_0 occupied by one particle. Thus, we take into account the interaction of energy levels in the framework of statistical analysis.

The second example is an ideal gas with a characteristic volume $v_\nu \gg v_0$ meeting condition $\mathscr{E}_\nu^0 \beta \ll 1$. In this case, we can retain only the first-order terms in the product entering the logarithm argument. Then, assuming that $v_{\nu+1} - v_\nu = v_\infty$, $v_\nu = \nu v_\infty$, we obtain the expression for μ ($z_\nu \gg z_0$):

$$\mu = h_0^0 - kT \ln \sum_{\nu=0} \frac{v_0}{\Lambda^3} e^{-\beta p v_\infty \nu} = h_0^0 - kT \ln \frac{v_0}{\Lambda^3} (1 - e^{-\beta p v_\infty})^{-1}. \quad (16)$$

At $\beta \longrightarrow 0$, we find the well-known expression for the chemical potential of ideal gas: $\mu - h_0^0 = kT\ln(p\Lambda^3/kT)$. At the same time, expression (16) provides an opportunity to obtain a more general equation of state by differentiating it with respect to p:

$$\bar{v} - v_0 = \frac{v_\infty}{e^{\beta p v_\infty} - 1}.$$

Assuming that $v_0 \equiv v_\infty$, we can write the following expression for compressibility factor z:

$$z = \frac{pv}{kT} = \frac{q}{1 - e^{-q}}, \quad q = \frac{\rho v_0}{kT}. \quad (17)$$

In Fig. 1, the curve calculated according to (17) is compared with the experimental data for argon at $T = 300$ K (dots). In the same figure, we present the calculations in the framework of the Kirkwood method [2], using the pair interaction function and the model Lennard-Jones potential (crosses). The dashed line corresponds to the free volume theory [2]. It is clear that our approach provides a rather simple way to obtain results that agree well with experimental data.

The third example is sublimation. Keeping in (12) the z_0 value for the solid phase, we relate z_ν summed according to (16) with the gas phase. Then, measuring

the energy from the lowest level z_0 and introducing notation $\mathscr{E}_1^0 = u$, we obtain

$$\mu = h_0^0 - kT\ln\left[z_0 + e^{-\beta u}\frac{v_0}{\Lambda^3}(1-e^{-q})^{-1}\right]. \quad (18)$$

Let us define the phase transition point as that where the contributions from both phases to μ become equal:

$$z_0 = e^{-\beta u}\frac{v_0}{\Lambda^3}(1-e^{-q})^{-1}. \quad (19)$$

Solving (19) with respect to q, we get

$$q \equiv \beta p v_0 = -\ln\left(1 - \frac{v_0}{\Lambda^3 z_0}e^{-\beta u}\right). \quad (20)$$

In the case of $v_0 \longrightarrow 0$, this expression coincides with the well-known expression for equilibrium vapor [8]

$$P(T) = \frac{kT}{\Lambda^3 z_0}e^{-\beta u}. \quad (21)$$

In these expressions, z_0 is given by the Debye formula (9), (14). It is clear that more general expression (20) remains valid up to the triple point. When we use the Gibbs function, the phase transition turns out to be continuous, but it manifests itself in the steep volume change from v_0 to V. At the phase transition point itself, we have $\bar{v} = V/2$. This could be demonstrated by differentiating (18) with respect to p and using (19).

Note that a number of problems considered in [8] based on other distributions can be solved rather simply by means of the Gibbs potential (12).

The last examples demonstrate that we can use relationship $v_\nu = \nu\bar{v}$ for the gas phase. The clearest description can be attained if $v_1 = 2v_0$, i.e., when the particle hopping to neighboring sites (corresponding to the Shottky defects) is taken into account. In this case, we can choose two characteristic values of the activation energy, $\mathscr{E}_1^0$ and $\mathscr{E}_2^0$. A more accurate partition can be performed assuming that $v_\nu = v_0/2$ for both solid and liquid phases (the Frenkel' defects).

However, a direct approach is expected to provide the most accurate results. Let us specify an appropriate effective potential for a particle. Then, we can calculate $\mathscr{E}_n$ by using, e.g., the Bohr–Sommerfeld quantization conditions [7]

$$\int_{r_0}^{r_\nu}\sqrt{2m(\mathscr{E}_n - u(r)) - \frac{\hbar^2(l+1/2)^2}{r^2}}\,dr = \hbar\pi(M_r + 1/2);$$

hence, we can choose v_ν and $\mathscr{E}_\nu^0$.

In any case, the distributions over T, p, and N corresponding to the Gibbs potential (12) provide an opportunity to construct rather good models for the thermal and calorific equations of state.

REFERENCES

1. J. E. Mayer and M. G. Mayer, *Statistical Mechanics* (Wiley, New York, 1977; Mir, Moscow, 1980).
2. T. L. Hill, *Statistical Mechanics: Principles and Selected Applications* (McGraw-Hill, New York, 1956; Inostrannaya Literatura, Moscow, 1960).
3. P. Lloyd and J. J. O'Dwyer, Mol. Phys. **6**, 573 (1963).
4. D. R. Cruise, J. Phys. Rev. **74**, 405 (1970).
5. W. Kohn and J. R. Onffroy, J. Phys. Chem. B **8**, 2485 (1973).
6. M. P. Vukalovich and I. I. Novikov, *Thermodynamics* (Mashinostroenie, Moscow, 1972).
7. L. D. Landau and E. M. Lifshitz, *Quantum Mechanics: Non-Relativistic Theory* (Nauka, Moscow, 1989, 4th ed.; Pergamon, Oxford, 1977, 3rd ed.).
8. R. Kubo, *Statistical Mechanics: An Advanced Course with Problems and Solutions* (North-Holland, Amsterdam, 1965; Mir, Moscow, 1967).
9. Yu. B. Rumer and M. Sh. Ryvkin, *Thermodynamics, Statistical Physics, and Kinetics* (Nauka, Moscow, 1977).
10. K. M. Magomedov, Dokl. Akad. Nauk **368**, 189 (1999) [Dokl. Phys. **44**, 615 (1999)].

Translated by O. Chernavskaya

Doklady Physics, Vol. 45, No. 8, 2000, pp. 410–414. Translated from Doklady Akademii Nauk, Vol. 373, No. 5, 2000, pp. 623–627.

MECHANICS

On Singularities of Boundaries for Parametric Resonance

A. A. Maĭlybaev and A. P. Seĭranyan

Presented by Academician V.V. Rumyantsev November 23, 1999

Received November 30, 1999

The theory of parametric resonance has broad applications in science and technology [1]. The basic issue of this theory is constructing stability domains in the space of parameters. The boundary of the stability domain may possess singularities, whose occurrence causes computational problems and affects the physical properties of a system.

In this study, a classification of generic-position singularities of stability-domain boundaries is performed for systems of general-form linear differential equations with coefficients periodic in time and dependent on two or three parameters. A constructive approach is proposed allowing the stability domain in the vicinity of a point of its boundary to be found in the first approximation. This approach is based on information available at that point, namely, the values of multipliers, the eigenvectors and adjoint vectors of the monodromy matrix, and the first derivatives of the system operator with respect to parameters. It is worth noting that, unlike some previous studies [1], the closeness of a periodic system to a stationary one was not assumed in the present paper. Singularities of stability-domain boundaries for stationary systems have been studied in [2–4].

1. We consider a system of linear homogeneous differential equations with periodic coefficients

$$\dot{\mathbf{x}} = \mathbf{G}\mathbf{x}, \tag{1}$$

where $\mathbf{x}$ is the real vector of the dimension m, and $\mathbf{G} = \mathbf{G}(t)$ is a real-valued matrix function of the dimension $m \times m$, which is continuous in time t and periodic with minimum period T, i.e., $\mathbf{G}(t + T) = \mathbf{G}(t)$.

A matrix-valued function $\mathbf{X}(t)$ obeying the equation $\dot{\mathbf{X}} = \mathbf{G}\mathbf{X}$, $\mathbf{X}(0) = \mathbf{I}$, where $\mathbf{I}$ is the unit matrix, is referred to as a matriciant, with its value $\mathbf{F} = \mathbf{X}(T)$ being the monodromy matrix [1]. The eigenvalues of the monodromy matrix $\mathbf{F}$ are said to be multipliers.

The stability of system (1) is determined by the following conditions imposed on the multipliers $\rho_1, \ldots, \rho_m$ [1]: If all multipliers lie inside the unit circle $|\rho_j| < 1$, $j = 1, \ldots, m$, system (1) is asymptotically stable. If at least one multiplier lies outside the unit circle $|\rho_j| > 1$, system (1) will be unstable (parametric resonance).

The matrix $\mathbf{G}$ in (1) and period T will be considered to depend smoothly on the vector $\mathbf{p} = (p_1, \ldots, p_n)$ of real parameters. Then, the monodromy matrix is a smooth function of parameters $\mathbf{F}(\mathbf{p})$, and its first derivatives are of the form [5]

$$\frac{\partial \mathbf{F}}{\partial p_k} = \mathbf{F}\int_0^T \mathbf{Y}^T \frac{\partial \mathbf{G}}{\partial p_k}\mathbf{X}\,dt + \mathbf{G}(T)\mathbf{F}\frac{\partial T}{\partial p_k}, \tag{2}$$

where $\mathbf{Y}(t)$ is the matriciant of the conjugate system $\dot{\mathbf{Y}} = -\mathbf{G}^T\mathbf{Y}$, $\mathbf{Y}(0) = \mathbf{I}$. The matriciants $\mathbf{X}(t)$ and $\mathbf{Y}(t)$ are bound by the relation $\mathbf{X}(t)^T\mathbf{Y}(t) = \mathbf{I}$.

2. The asymptotic-stability condition divides the space of parameters R^n into a stability region and instability one (the region of parametric resonance). The transition from the stability region to the instability one is accompanied by the emergence of certain multipliers from the unit circle. In particular, when real multipliers go through the points 1 and –1, it is said to be the primary resonance; the emergence of a complex-conjugate pair through the unit circle at the points $\exp(\pm i\omega)$ ($\omega \neq \pi k$, $k \in Z$) is spoken of as a combinative resonance. Thus, the stability-domain boundary is determined by the presence of multipliers in the unit circle, providing the rest of the multipliers to lie inside the unit circle. Generally, the stability-domain boundary is a smooth hypersurface in a parameter space with certain singularities (points where the smoothness is lost). Singularities of the generic position (typical singularities) are of particular interest. The emergence of such singularities is always expected in studies of particular systems. As for the singularities of the nongeneric position, they are a consequence of a certain degeneracy or a symmetry of a system and disappear if the system is subjected to a perturbation as small as is wished [2].

We denote the types of the boundary points using the product of multipliers located in the unit circle, with exponents equal to the dimensions of the corresponding Jordan boxes. For example, $1^2\exp(\pm i\omega_1)\exp(\pm i\omega_2)$ implies that the monodromy matrix $\mathbf{F}$ has twofold $\rho = 1$ with the Jordan box of the second order and two pairs

Institute of Mechanics, Moscow State University, Michurinskiĭ pr. 1, Moscow, 117192 Russia

1028-3358/00/4508-0410$20.00

of simple multipliers $\rho = \exp(\pm i\omega_1)$, $\exp(\pm i\omega_2)$, such that $\omega_1, \omega_2 \in (0, \pi)$, $\omega_1 \neq \omega_2$.

For convenience, we introduce a concise notation for certain types of boundary points

$$B_1(1), \quad B_2(-1), \quad B_3(\exp(\pm i\omega)), \tag{3}$$

$$C_1(1^2), \quad C_2((-1)^2), \tag{4}$$

$$D_1(1^3), \quad D_2((-1)^3), \quad D_3((\exp(\pm i\omega))^2), \tag{5}$$

and for their combinations as well

$$\begin{gathered} B_{12}(1(-1)), \quad B_{13}(1\exp(\pm i\omega)), \quad B_{23}((-1)\exp(\pm i\omega)), \\ B_{33}(\exp(\pm i\omega_1)\exp(\pm i\omega_2)), \end{gathered} \tag{6}$$

$$\begin{gathered} B_{123}(1(-1)\exp(\pm i\omega)), \\ B_{133}(1\exp(\pm i\omega_1)\exp(\pm i\omega_2)), \\ B_{233}((-1)\exp(\pm i\omega_1)\exp(\pm i\omega_2)), \\ B_{333}(\exp(\pm i\omega_1)\exp(\pm i\omega_2)\exp(\pm i\omega_3)), \\ C_1B_2(1^2(-1)), \\ C_2B_1((-1)^21), \quad C_1B_3(1^2\exp(\pm i\omega)), \\ C_2B_3((-1)^2\exp(\pm i\omega)). \end{gathered} \tag{7}$$

Qualitative analysis of the stability domain in the vicinity of its boundary point is carried out on the basis of the theory of versal deformations [2, 6]. The result obtained is stated in the form of a theorem.

Theorem 1. *In the generic-position case, the stability-domain boundary for system* (1) *consists of* (a) *isolated points of B_1-, B_2-, and B_3-types* [*see* (3)] *corresponding to the primary resonance and combinative one in the case of one parameter*; (b) *smooth curves of type* (3) *intersecting each other transversally* (*at nonzero angle*) *at break points of types* (4), (6) *in the case of two parameters*; (c) *smooth surfaces of type* (3), *whose singularities are curves of types* (4), (6) (*i.e., the dihedral angle*) *and separate points of type* (5) D_1, D_2 (*i.e., the edge break*), D_3 (*i.e., dead end in the edge*), *and* (7), (*i.e., trihedral angle*) *in the case of three parameters.*

The stability domains in the vicinity of singular points of the above-listed types, up to the nondegenerate smooth change of parameters (diffeomorphism), are of the form presented in Figs. 1 and 2 (the stability domain is denoted by the letter *S*).

3. Consider a point of the stability-domain boundary $\mathbf{p} = \mathbf{p}_0$.

(a) Let ρ_0 be a simple multiplier of the matrix $\mathbf{F}_0 = \mathbf{F}(\mathbf{p}_0)$ and $\mathbf{u}_0$, $\mathbf{v}_0$ be the right and left eigenvectors, respectively, corresponding to the multiplier

$$\mathbf{F}_0\mathbf{u}_0 = \rho_0\mathbf{u}_0, \quad \mathbf{v}_0^T\mathbf{F}_0 = \rho_0\mathbf{v}_0^T. \tag{8}$$

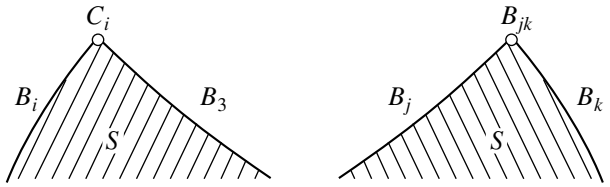

Fig. 1.

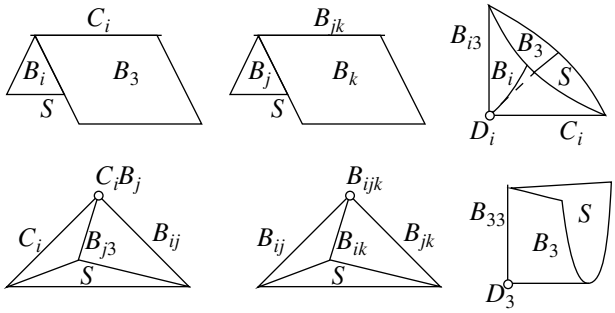

Fig. 2.

We introduce the real *n*-dimensional vectors **r** and **k** with the components

$$r^s + ik^s = \frac{\mathbf{v}_0^T\dfrac{\partial\mathbf{F}}{\partial p_s}\mathbf{u}_0}{\mathbf{v}_0^T\mathbf{u}_0}, \quad s = 1, \ldots, n, \tag{9}$$

where *i* is the imaginary unit. If ρ_0 is a real number, then $\mathbf{k} = 0$.

(b) We now consider the case of the twofold multiplier ρ_0 with the second-order Jordan box. Jordan chains for right and left eigenvectors and adjoint vectors are of the form

$$\begin{aligned} &\mathbf{F}_0\mathbf{u}_0 = \rho_0\mathbf{u}_0, \quad \mathbf{F}_0\mathbf{u}_1 = \rho_0\mathbf{u}_1 + \mathbf{u}_0; \\ &\mathbf{v}_0^T\mathbf{F}_0 = \rho_0\mathbf{v}_0^T, \quad \mathbf{v}_1^T\mathbf{F}_0 = \rho_0\mathbf{v}_1^T + \mathbf{v}_0^T. \end{aligned} \tag{10}$$

We consider the vectors $\mathbf{u}_0$ and $\mathbf{u}_1$ as fixed and introduce the normalization $\mathbf{v}_0^T\mathbf{u}_1 = 1$, $\mathbf{v}_1^T\mathbf{u}_1 = 0$ unambiguously defining the vectors $\mathbf{v}_0$, $\mathbf{v}_1$. We define the real vectors $\mathbf{f}_1$, $\mathbf{f}_2$, $\mathbf{q}_1$, and $\mathbf{q}_2$ with the components

$$\begin{aligned} f_1^s + if_2^s &= \mathbf{v}_0^T\frac{\partial\mathbf{F}}{\partial p_s}\mathbf{u}_0, \\ q_1^s + iq_2^s &= \mathbf{v}_0^T\frac{\partial\mathbf{F}}{\partial p_s}\mathbf{u}_1 + \mathbf{v}_1^T\frac{\partial\mathbf{F}}{\partial p_s}\mathbf{u}_0, \quad s = 1, \ldots, n. \end{aligned} \tag{11}$$

If ρ_0 is a real number, then $\mathbf{f}_2 = \mathbf{q}_2 = 0$.

(c) Next, we consider the case of the threefold real multiplier ρ_0 with the third-order Jordan box. The Jor-

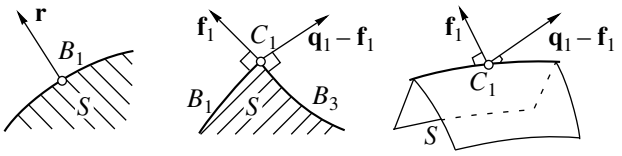

Fig. 3.

dan chains for 1 and left eigenvectors and adjoint vectors are of the form

$$\mathbf{F}_0\mathbf{u}_0 = \rho_0\mathbf{u}_0, \quad \mathbf{F}_0\mathbf{u}_1 = \rho_0\mathbf{u}_1 + \mathbf{u}_0,$$
$$\mathbf{F}_0\mathbf{u}_2 = \rho_0\mathbf{u}_2 + \mathbf{u}_1, \quad \mathbf{v}_0^T\mathbf{F}_0 = \rho_0\mathbf{v}_0^T, \qquad (12)$$
$$\mathbf{v}_1^T\mathbf{F}_0 = \rho_0\mathbf{v}_1^T + \mathbf{v}_0^T, \quad \mathbf{v}_2^T\mathbf{F}_0 = \rho_0\mathbf{v}_2^T + \mathbf{v}_1^T.$$

Considering the vectors $\mathbf{u}_0$, $\mathbf{u}_1$, and $\mathbf{u}_2$ as fixed, we impose the normalization conditions $\mathbf{v}_0^T\mathbf{u}_2 = 1$, $\mathbf{v}_1^T\mathbf{u}_2 = 0$, and $\mathbf{v}_2^T\mathbf{u}_2 = 0$ on $\mathbf{v}_0$, $\mathbf{v}_1$, and $\mathbf{v}_2$. Since ρ_0 is a real number, the vectors $\mathbf{u}_i$ and $\mathbf{v}_i$ can be chosen to be real. We introduce the n-dimensional vectors $\mathbf{g}$, $\mathbf{h}$, and $\mathbf{t}$ and a matrix $\mathbf{R}$ with the dimension $n \times n$ of the form

$$g^s = \mathbf{v}_0^T\frac{\partial}{\partial p_s}(\mathbf{F})\mathbf{u}_0, \quad h^s = \mathbf{v}_0^T\frac{\partial}{\partial p_s}(\mathbf{F})\mathbf{u}_1 + \mathbf{v}_1^T\frac{\partial}{\partial p_s}(\mathbf{F})\mathbf{u}_0,$$
$$t^s = \mathbf{v}_0^T\frac{\partial}{\partial p_s}(\mathbf{F})\mathbf{u}_2 + \mathbf{v}_1^T\frac{\partial}{\partial p_s}(\mathbf{F})\mathbf{u}_1 + \mathbf{v}_2^T\frac{\partial}{\partial p_s}(\mathbf{F})\mathbf{u}_0, \ s = 1, \ldots, n,$$
$$\mathbf{R} = \left[\mathbf{v}_0^T\frac{\partial}{\partial p_i}(\mathbf{F})[\mathbf{F}_0 - \rho_0\mathbf{I} - \mathbf{v}_0\mathbf{v}_2^T]^{-1}\frac{\partial\mathbf{F}}{\partial p_j}\mathbf{u}_0 - \mathbf{v}_0^T\frac{\partial^2\mathbf{F}}{\partial p_i\partial p_j}\mathbf{u}_0\right], \qquad (13)$$
$$i, j = 1, \ldots, n.$$

Expressions for the second derivatives of the matrix $\mathbf{F}$ are presented in [5].

4. We draw a smooth curve $\mathbf{p} = \mathbf{p}(\varepsilon)$ from the point of the boundary of a parametric resonance [$\mathbf{p}_0 = \mathbf{p}(0)$, $\varepsilon \geq 0$]. In this case, some curves will lie (for small $\varepsilon > 0$) in the stability domain and others, in the instability one. We select a direction $\mathbf{e} = \left.\frac{d\mathbf{p}}{d\varepsilon}\right|_{\varepsilon = 0}$ of the curves lying in the stability domain. The set of such directions forms a cone tangent to the stability domain at the point of its boundary $\mathbf{p} = \mathbf{p}_0$. The tangent cone is an approximation for the stability domain in the vicinity of point of its boundary.

Theorem 2. *Cones tangent to the stability domain at its boundary points of the type* (3)–(5) *are determined by the relations*

$$K_{B_1} = \{\mathbf{e}: (\mathbf{r}, \mathbf{e}) \leq 0\}, \quad K_{B_2} = \{\mathbf{e}: (\mathbf{r}, \mathbf{e}) \geq 0\},$$
$$K_{B_3} = \{\mathbf{e}: (\mathbf{r}\cos\omega + \mathbf{k}\sin\omega, \mathbf{e}) \leq 0\},$$
$$K_{C_1} = \{\mathbf{e}: (\mathbf{f}_1, \mathbf{e}) \leq 0, (\mathbf{q}_1 - \mathbf{f}_1, \mathbf{e}) \leq 0\},$$
$$K_{C_2} = \{\mathbf{e}: (\mathbf{f}_1, \mathbf{e}) \leq 0, (\mathbf{q}_1 + \mathbf{f}_1, \mathbf{e}) \geq 0\},$$
$$K_{D_1} = \{\mathbf{e}: (\mathbf{g}, \mathbf{e}) = 0, (\mathbf{h}, \mathbf{e}) \leq 0, (\mathbf{t} - \mathbf{h}, \mathbf{e}) \leq 0\}, \qquad (14)$$
$$K_{D_2} = \{\mathbf{e}: (\mathbf{g}, \mathbf{e}) = 0, (\mathbf{h}, \mathbf{e}) \leq 0, (\mathbf{t} + \mathbf{h}, \mathbf{e}) \geq 0\},$$
$$K_{D_3} = \{\mathbf{e}: (\mathbf{f}_2\cos 2\omega - \mathbf{f}_1\sin 2\omega, \mathbf{e}) = 0,$$
$$(\mathbf{f}_1\cos 2\omega + \mathbf{f}_2\sin 2\omega, \mathbf{e}) \leq 0,$$
$$(\mathbf{q}_1\cos\omega + \mathbf{q}_2\sin\omega - \mathbf{f}_1\cos 2\omega - \mathbf{f}_2\sin 2\omega, \mathbf{e}) \leq 0\},$$

where vectors are calculated for the multiplier determining the type of a boundary point. The tangent cones for the combined types (6), (7) *are produced by the intersection of tangent cones found for each of the subtypes. For example, in the case C_1B_2, we have $K_{C_1B_2} = K_{C_1} \cap K_{B_2}$.*

In the cases B_1, B_2, B_3, C_1, C_2, and D_3, all smooth curves drawn in $\mathbf{e}$-direction satisfying rigorous inequalities (14) lie in the stability domain for sufficiently small $\varepsilon > 0$. In the cases D_1 and D_2, curves satisfying additional conditions

$$(\mathbf{Re}, \mathbf{e}) - (\mathbf{t} - \mathbf{h}, \mathbf{e})(\mathbf{h}, \mathbf{e}) < (\mathbf{g}, \mathbf{d}) < (\mathbf{Re}, \mathbf{e})$$

and

$$(\mathbf{Re}, \mathbf{e}) < (\mathbf{g}, \mathbf{d}) < (\mathbf{Re}, \mathbf{e}) - (\mathbf{t} + \mathbf{h}, \mathbf{e})(\mathbf{h}, \mathbf{e})$$

respectively, $\left(\text{where } \mathbf{d} = \frac{1}{2}\left(\frac{d^2\mathbf{p}}{d\varepsilon^2}\right)\Big|_{\varepsilon = 0}\right)$ lie in the stability domain. It is worth noting that the tangent cones K_{D_1}, K_{D_2}, and K_{D_3} are degenerate (are two-dimensional angles in the three-dimensional parameter space).

Theorem 2 enables us to find, in the first approximation, the stability domain in the vicinity of a point of the stability-domain boundary from information at this point [using first derivatives of the operator $\mathbf{G}$ from (1) with respect to parameters and values of multipliers and corresponding eigenvectors and adjoint vectors calculated for $\mathbf{p} = \mathbf{p}_0$]. Relations (14) provide a clear idea of the stability domain. For example, in the case of non-

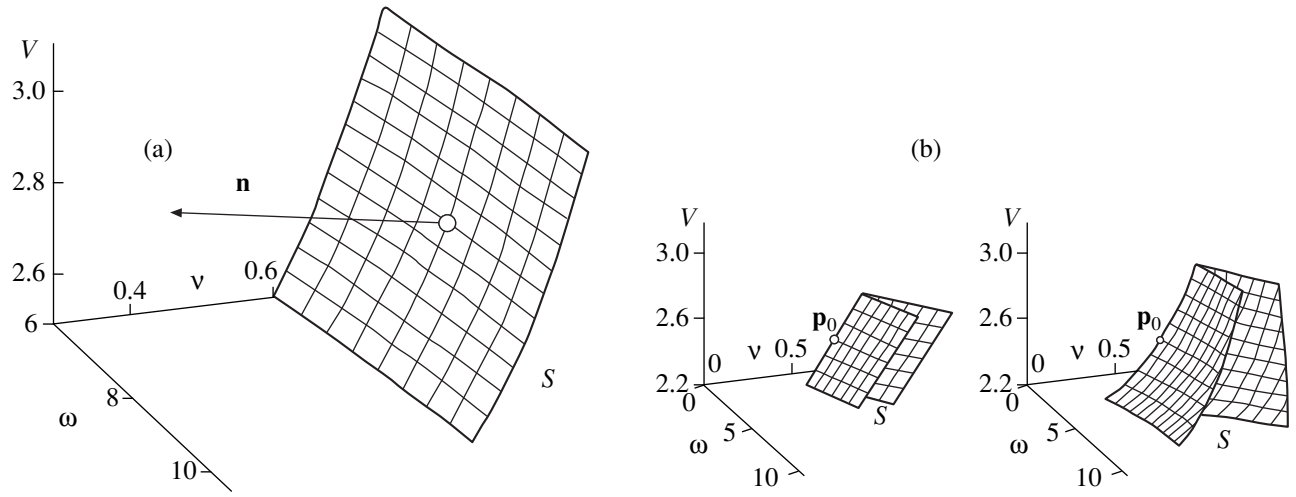

Fig. 4.

singular point B_1, a tangent cone is determined by the inequality $(\mathbf{r}, \mathbf{e}) \le 0$. Therefore, a plane tangent to the stability-domain boundary is specified by the equation $(\mathbf{r}, \mathbf{e}) = 0$, and the vector $\mathbf{r}$ is a normal to the boundary lying in the region of a parametric resonance (see Fig. 3). For the case of the singular point C_1, the tangent cone is the intersection of the half planes (half spaces) $(\mathbf{f}_1, \mathbf{e}) \le 0$ and $(\mathbf{q}_1 - \mathbf{f}_1, \mathbf{e}) \le 0$. These inequalities determine a two-dimensional (dihedral) angle in a space of two (three) parameters, which is the first approximation to the stability domain (Fig. 3).

5. As an example, we consider two-dimensional vibrations of a two-link pipe, along which a fluid with the linear mass m and pulsating velocity

$$u(t) = U(1 + \nu\sin\omega t)$$

flows. The pipe parts are connected by elastic hinges having the rigidity coefficients equal to c; they have the length l and linear mass $M = 2m$. The right end is free. We choose the angles φ and ψ of the deviation of the pipe parts from a horizontal axis as generalized coordinates. The linearized equations for the motion of the system in terms of dimensionless variables are of the form [7]

$$\dot{\mathbf{x}} = \mathbf{G}\mathbf{x}, \quad \mathbf{x} = (\varphi, \psi, \dot{\varphi}, \dot{\psi})^T,$$

$$\mathbf{G}(\tau) = \begin{pmatrix} \mathbf{O} & \mathbf{I} \\ -\mathbf{M}^{-1}\mathbf{C} & -\mathbf{M}^{-1}\mathbf{B} \end{pmatrix}, \quad \mathbf{M} = \begin{pmatrix} 4 & 1.5 \\ 1.5 & 1 \end{pmatrix}, \quad (15)$$

$$\mathbf{B} = v(\tau)\begin{pmatrix} 1 & 2 \\ 0 & 1 \end{pmatrix}, \quad \mathbf{C} = \begin{pmatrix} 2 - f(\tau) & -1 + f(\tau) \\ -1 & 1 \end{pmatrix},$$

where $\mathbf{O}$ is the zero matrix of the dimension 2×2, and differentiation with respect to the dimensionless time τ is denoted by a dot. The following notation is used:

$$\tau = \alpha t, \quad f(\tau) = \dot{v}(\tau) + v^2(\tau),$$

$$v(\tau) = V(1 + \nu\sin w\tau), \quad w = \frac{\omega}{\alpha},$$

$$V = \frac{U}{\alpha l}, \text{ and } \alpha^2 = \frac{c}{ml^3}.$$

The matrix operator $\mathbf{G}(\tau)$ with the period $T = 2\pi/w$ smoothly depends on the dimensionless parameters $\mathbf{p} = (w, \nu, V)$.

We consider the point $\mathbf{p}_0 = (8, 0.737, 2.8)$ in the parameter space. We calculate the monodromy matrix $\mathbf{F}_0$ at this point and find the multipliers of the matrix:

$$\rho_{1,2} = \exp(\pm 0.882i), \quad \rho_3 = 0.535, \quad \rho_4 = 0.152.$$

Since ordinary complex-conjugate multipliers lie in the unit circumference $|\rho_{1,2}| = 1$, and the other multipliers are inside the unit circle, the point $\mathbf{p}_0$ is the regular point of the stability-domain boundary of the B_3-type. According to (14), the K_{B_3} cone tangent to the stability domain at the point $\mathbf{p}_0$ is described by the expression $(\mathbf{r}\cos\omega + \mathbf{k}\sin\omega, \mathbf{e}) \le 0$, where $\omega = \arg\rho_1$; the vectors $\mathbf{r}$ and $\mathbf{k}$ are calculated according to (2), (9). The vector $\mathbf{n} = \mathbf{r}\cos\omega + \mathbf{k}\sin\omega = (0.03, -2.05, 0.51)$ is the normal to the stability-domain boundary and lies in the parametric-resonance region. The numerically calculated boundary of the stability domain and the vector $\mathbf{n}$ are shown in Fig 4a.

Finally, we consider the point $\mathbf{p}_0 = (3.643, 0.5555, 2.6)$, at which the monodromy matrix $\mathbf{F}_0$ has the multipliers $\rho_1 = \rho_2 = -1$, $\rho_3 = 0.225$, $\rho_4 = 0.026$, second-order Jordan chains (10) being relevant to a twofold multiplier (we denote it by $\rho_0 = -1$). Since the twofold multiplier $\rho_0 = -1$ belongs to the boundary, and two others

lie inside the unit circle, from Theorem 1, a singularity of the stability-domain boundary of the C_2 type (i.e., of the dihedral-angle type) is realized at the point $\mathbf{p}_0$. According to (2), (11), we find the vectors $\mathbf{f}_1 = (-5.15, 45.2, -7.77)$, $\mathbf{q}_1 = (4.49, -31.1, 3.16)$. From Theorem 2, these vectors define the cone tangent to the stability domain

$$K_{C_2} = \{\mathbf{e}: (\mathbf{f}_1, \mathbf{e}) \le 0, (\mathbf{q}_1 + \mathbf{f}_1, \mathbf{e}) \ge 0\}.$$

The vectors $\mathbf{f}_1$ and $-(\mathbf{q}_1 + \mathbf{f}_1)$ are normals to the sides of the dihedral angle, and they lie in the region of the parametric resonance. The vector $\mathbf{e}_\tau$ tangent to the edge of the dihedral angle is equal to $\mathbf{e}_\tau = (\mathbf{q}_1 + \mathbf{f}_1) \times \mathbf{f}_1$. In Fig. 4b (to the left), a dihedral angle is shown, which is an approximation for the stability-domain boundary in the vicinity of the point $\mathbf{p}_0$. For comparison, at the right of Fig. 4b, the numerically calculated stability-domain boundary is shown confirming the presence of the singularity and reasonable agreement of the results obtained.

Our results can be employed in solving various problems of stabilization of parameter-dependent periodic systems with the use of gradient methods.

REFERENCES

1. V. A. Yakubovich and V. M. Starzhinskiĭ, *Parametric Resonance in Linear Systems* (Nauka, Moscow, 1987).
2. V. I. Arnol'd, *Complementary Chapters in the Theory of Ordinary Linear Equations* (Nauka, Moscow, 1978).
3. A. A. Mailybaev and A. P. Seyranian, SIAM J. Matrix Anal. Appl. **20** (4) (1999).
4. A. A. Maĭlybaev and A. P. Seĭranyan, Prikl. Mat. Mekh. **63**, 568 (1999).
5. A. P. Seyranian, F. Solem, and P. Pedersen, Arch. Appl. Mech. **69**, 160 (1999).
6. D. M. Galin, Usp. Mat. Nauk **27**, 241 (1972).
7. Z. Szabo, S. C. Sinha, and G. Stepan, in *Proceedings of the European Nonlinear Oscillation Conference, EUROMECH II, Prague, 1996*, Vol. 1, pp. 439–442.

Translated by V. Tsarev

Doklady Physics, Vol. 45, No. 8, 2000, pp. 415–418. Translated from Doklady Akademii Nauk, Vol. 373, No. 5, 2000, pp. 628–631.

MECHANICS

Structure of Solutions to Linear Unsteady Boundary Value Problems in Mechanics and Mathematical Physics

A. D. Polyanin

Presented by Academician D.M. Klimov December 16, 1999

Received December 17, 1999

We consider unidimensional and multidimensional linear unsteady nonhomogeneous boundary value problems for equations of the parabolic and hyperbolic types with coefficients being arbitrary functions of spatial coordinates and time. We derive general formulas allowing solutions to these problems to be expressed in terms of the Green's functions in the case of boundary conditions of all basic types. These results can be used in the theory of heat transfer and mass transfer, in wave theory, and in other branches of mechanics and theoretical physics.

The formulas obtained generalize results of a large number of studies (e.g., [1–7]) in which special unsteady boundary value problems were considered.

1. Parabolic equations with one spatial variable. We consider a linear nonhomogeneous differential parabolic equation of the general form with variable coefficients

$$\frac{\partial w}{\partial t} - L_{x,t}[w] = \Phi(x, t), \tag{1}$$

where

$$L_{x,t}[w] \equiv a(x, t)\frac{\partial^2 w}{\partial x^2} + b(x, t)\frac{\partial w}{\partial x} + c(x, t)w, \qquad a(x, t) > 0. \tag{2}$$

Hereafter, subscripts in the operator L indicate that its coefficients depend on x and t.

In the domain $\{t \geq 0, x_1 \leq x \leq x_2\}$, the solution to the boundary value problem for equation (1) under arbitrary nonhomogeneous initial conditions and boundary conditions

$$w = f(x) \text{ for } t = 0, \tag{3}$$

$$s_1\partial_x w + k_1 w = g_1(t) \text{ for } x = x_1, \tag{4}$$

$$s_2\partial_x w + k_2 w = g_2(t) \text{ for } x = x_2, \tag{5}$$

can be represented as the sum

$$\begin{aligned} w(x, t) = {} & \int_0^t \int_{x_1}^{x_2} \Phi(y, \tau)G(x, y, t, \tau)dyd\tau \\ & + \int_{x_1}^{x_2} f(y)G(x, y, t, 0)dy \\ & + \int_0^t g_1(\tau)a(x_1, \tau)\Lambda_1(x, t, \tau)d\tau \\ & + \int_0^t g_2(\tau)a(x_2, \tau)\Lambda_2(x, t, \tau)d\tau, \end{aligned} \tag{6}$$

where $\partial_x w$ is the partial derivative with respect to x. Here, $G(x, y, t, \tau)$ is the Green's function that, for arbitrary $t > \tau \geq 0$, satisfies the homogeneous equation

$$\frac{\partial G}{\partial t} - L_{x,t}[G] = 0 \tag{7}$$

with the special nonhomogeneous initial condition and homogeneous boundary conditions

$$G = \delta(x - y) \text{ for } t = \tau, \tag{8}$$

$$s_1\partial_x G + k_1 G = 0 \text{ for } x = x_1, \tag{9}$$

$$s_2\partial_x G + k_2 G = 0 \text{ for } x = x_2. \tag{10}$$

Here, the quantities y and τ enter into problem (7)–(10) as free parameters ($x_1 \leq y \leq x_2$), and $\delta(x)$ is the Dirac delta function.

The functions $\Lambda_1(x, t, \tau)$ and $\Lambda_2(x, t, \tau)$ in the integrands of two last terms in solution (6) are expressed in terms of the Green's function $G(x, y, t, \tau)$. For the boundary value problems of basic types, the corresponding formulas for $\Lambda_m(x, t, \tau)$ ($m = 1, 2$) are listed in Table 1.

It is important to emphasize that both the Green's function G and functions Λ_m are independent of the

Institute of Problems in Mechanics, Russian Academy of Sciences, pr. Vernadskogo 101, Moscow, 117526 Russia

1028-3358/00/4508-0415$20.00

Table 1

Type of the boundary value problem	Form of the boundary conditions	Functions $\Lambda_m(x, t, \tau)$
First ($s_1 = s_2 = 0$, $k_1 = k_2 = 1$)	$w = g_1(t)$ at $x = x_1$	$\Lambda_1(x, t, \tau) = \partial_y G(x, y, t, \tau)\big\|_{y = x_1}$
	$w = g_2(t)$ at $x = x_2$	$\Lambda_2(x, t, \tau) = -\partial_y G(x, y, t, \tau)\big\|_{y = x_2}$
Second ($s_1 = s_2 = 1$, $k_1 = k_2 = 0$)	$\partial_x w = g_1(t)$ at $x = x_1$	$\Lambda_1(x, t, \tau) = -G(x, x_1, t, \tau)$
	$\partial_x w = g_2(t)$ at $x = x_2$	$\Lambda_2(x, t, \tau) = G(x, x_2, t, \tau)$
Third ($s_1 = s_2 = 1$, $k_1 < 0$, $k_2 > 0$)	$\partial_x w + k_1 w = g_1(t)$ at $x = x_1$	$\Lambda_1(x, t, \tau) = -G(x, x_1, t, \tau)$
	$\partial_x w + k_2 w = g_2(t)$ at $x = x_2$	$\Lambda_2(x, t, \tau) = G(x, x_2, t, \tau)$
Mixed ($s_1 = k_2 = 0$, $s_2 = k_1 = 1$)	$w = g_1(t)$ at $x = x_1$	$\Lambda_1(x, t, \tau) = \partial_y G(x, y, t, \tau)\big\|_{y = x_1}$
	$\partial_x w = g_2(t)$ at $x = x_2$	$\Lambda_2(x, t, \tau) = G(x, x_2, t, \tau)$
Mixed ($s_1 = k_2 = 1$, $s_2 = k_1 = 0$)	$\partial_x w = g_1(t)$ at $x = x_1$	$\Lambda_1(x, t, \tau) = -G(x, x_1, t, \tau)$
	$w = g_2(t)$ at $x = x_2$	$\Lambda_2(x, t, \tau) = -\partial_y G(x, y, t, \tau)\big\|_{y = x_2}$

functions Φ, f, g_1, and g_2 that define nonhomogeneous terms in the boundary value problem. If the coefficients of operator (2) are independent of time t, then the Green's function depends only on three arguments: $G(x, y, t, \tau) = G(x, y, t - \tau)$.

Formula (6) also holds true for this problem with the boundary conditions of the third kind provided that $k_1 = k_1(t)$ and $k_2 = k_2(t)$. In this case, the relations between the functions Λ_m ($m = 1, 2$) and the Green's function G are the same as in the case of the constant coefficients k_1 and k_2 (although the Green's function in itself is different).

The solutions to the first, second, and third boundary value problems in the semi-infinite interval $x_1 \le x < \infty$ are often required to vanish at infinity ($w \longrightarrow 0$ as $x \longrightarrow \infty$). In this case, the solution can be found by formula (6) with $\Lambda_2 = 0$ and with the expression for the function Λ_1 given in Table 1.

It is worth noting that the Green's function for various unsteady boundary value problems can be found, for example, in the books [1, 2, 5–8].

2. Hyperbolic equations with one spatial variable. We consider a linear nonhomogeneous hyperbolic equation of the general form with variable coefficients

$$\frac{\partial^2 w}{\partial t^2} + \varphi(x, t)\frac{\partial w}{\partial t} - L_{x,t}[w] = \Phi(x, t), \qquad (11)$$

where the form of the operator $L_{x,t}[w]$ is given by formula (2).

The solution to equation (11), which satisfies the nonhomogeneous initial conditions

$$w = f_0(x) \text{ at } t = 0, \qquad (12)$$

$$\partial_t w = f_1(x) \text{ at } t = 0 \qquad (13)$$

and arbitrary nonhomogeneous boundary conditions (4) and (5), can be represented as the sum

$$w(x, t) = \int_0^t \int_{x_1}^{x_2} \Phi(y, \tau) G(x, y, t, \tau)\, dy\, d\tau$$

$$- \int_{x_1}^{x_2} f_0(y)\left[\frac{\partial}{\partial \tau} G(x, y, t, \tau)\right]_{\tau = 0} dy$$

$$+ \int_{x_1}^{x_2} [f_1(y) + f_0(y)\varphi(y, 0)] G(x, y, t, 0)\, dy \qquad (14)$$

$$+ \int_0^t g_1(\tau) a(x_1, \tau) \Lambda_1(x, t, \tau)\, d\tau$$

$$+ \int_0^t g_2(\tau) a(x_2, \tau) \Lambda_2(x, t, \tau)\, d\tau.$$

Here, $G(x, y, t, \tau)$ is the Green's function that satisfies the homogeneous equation

$$\frac{\partial^2 G}{\partial t^2} + \varphi(x, t)\frac{\partial G}{\partial t} - L_{x,t}[G] = 0 \qquad (15)$$

with the semi-homogeneous initial conditions

$$G = 0 \text{ at } t = \tau, \qquad (16)$$

$$\partial_t G = \delta(x - y) \text{ at } t = \tau \qquad (17)$$

and homogeneous boundary conditions (9) and (10).

The functions $\Lambda_1(x, t, \tau)$ and $\Lambda_2(x, t, \tau)$ in the integrands of two last terms in solution (14) are expressed

Table 2

Type of the boundary value problem	Form of the boundary conditions (21)	Function $U(\mathbf{x}, \mathbf{y}, t, \tau)$
First	$w = g(\mathbf{x}, t)$ at $\mathbf{x} \in S$	$U(\mathbf{x}, \mathbf{y}, t, \tau) = -\frac{\partial G}{\partial M_y}(\mathbf{x}, \mathbf{y}, t, \tau)$
Second	$\frac{\partial w}{\partial M_x} = g(\mathbf{x}, t)$ at $\mathbf{x} \in S$	$U(\mathbf{x}, \mathbf{y}, t, \tau) = G(\mathbf{x}, \mathbf{y}, t, \tau)$
Third	$\frac{\partial w}{\partial M_x} + kw = g(\mathbf{x}, t)$ at $\mathbf{x} \in S$	$U(\mathbf{x}, \mathbf{y}, t, \tau) = G(\mathbf{x}, \mathbf{y}, t, \tau)$

in terms of the Green's function $G(x, y, t, \tau)$. For the boundary value problems of basic types, the corresponding formulas for $\Lambda_m(x, t, \tau)$ are listed in Table 1.

Formula (14) also holds true for this problem for the boundary conditions of the third kind with $k_1 = k_1(t)$ and $k_2 = k_2(t)$.

3. Parabolic equations with many variables. We consider a linear nonhomogeneous differential parabolic equation in n spatial variables, which takes the general form

$$\frac{\partial w}{\partial t} - L_{\mathbf{x}, t}[w] = \Phi(\mathbf{x}, t), \tag{18}$$

where

$$L_{\mathbf{x}, t}[w] \equiv \sum_{i, j = 1}^{n} a_{ij}(\mathbf{x}, t)\frac{\partial^2 w}{\partial x_i \partial x_j} + \sum_{i = 1}^{n} b_i(\mathbf{x}, t)\frac{\partial w}{\partial x_i} + c(\mathbf{x}, t)w, \tag{19}$$

$$\mathbf{x} = \{x_1, \ldots, x_n\}, \quad \sum_{i, j = 1}^{n} a_{ij}(\mathbf{x}, t)\xi_i\xi_j \geq \sigma\sum_{i = 1}^{n}\xi_i^2, \quad \sigma > 0.$$

Equations of this type, with $n = 1, 2, 3$, are the basis of the mathematical theory for the mass-and-heat transfer [1, 7, 8].

Let V be a closed domain in the space $\mathcal{R}^n$ having a sufficiently smooth indivisible surface $S = \partial V$. The solution to the linear boundary value problem in the domain V for equation (18) with arbitrary nonhomogeneous initial and boundary conditions

$$w = f(\mathbf{x}) \text{ at } t = 0, \tag{20}$$

$$\Gamma_{\mathbf{x}, t}[w] = g(\mathbf{x}, t) \text{ at } \mathbf{x} \in S \tag{21}$$

can be represented as a sum

$$w(\mathbf{x}, t) = \int_0^t\int_V \Phi(\mathbf{y}, \tau)G(\mathbf{x}, \mathbf{y}, t, \tau)dV_y d\tau + \int_V f(\mathbf{y})G(\mathbf{x}, \mathbf{y}, t, 0)dV_y + \int_0^t\int_S g(\mathbf{y}, \tau)U(\mathbf{x}, \mathbf{y}, t, \tau)dS_y d\tau. \tag{22}$$

Here, $G(\mathbf{x}, \mathbf{y}, t, \tau)$ is the Green's function that, for all $t > \tau \geq 0$, satisfies the homogeneous equation

$$\frac{\partial G}{\partial t} - L_{\mathbf{x}, t}[G] = 0 \tag{23}$$

with the special nonhomogeneous initial conditions and homogeneous boundary condition

$$G = \delta(\mathbf{x} - \mathbf{y}) \text{ at } t = \tau, \tag{24}$$

$$\Gamma_{\mathbf{x}, t}[G] = 0 \text{ at } \mathbf{x} \in S. \tag{25}$$

The quantity $\mathbf{y} = \{y_1, \ldots, y_n\}$ enters into problem (23)–(25) as an n-dimensional free parameter ($\mathbf{y} \in V$), and

$$\delta(\mathbf{x} - \mathbf{y}) = \delta(x_1 - y_1)\delta(x_2 - y_2)\ldots\delta(x_n - y_n).$$

The Green's function is independent of the functions Φ, f, and g defining nonhomogeneous terms in the boundary value problem. The integration in solution (22) is carried out over the parameter $\mathbf{y}$, with $dV_y = dy_1 dy_2 \ldots dy_n$.

The function $U(\mathbf{x}, \mathbf{y}, t, \tau)$ in the integrand of the last term of solution (22) is expressed in terms of the Green's function $G(\mathbf{x}, \mathbf{y}, t, \tau)$. For the boundary value problems of three basic types, the corresponding formulas for $U(\mathbf{x}, \mathbf{y}, t, \tau)$ are listed in Table 2 (in the case of the third boundary value problem, the coefficient k can depend on $\mathbf{x}$ and t). The operators of differentiation along the conormal of operator (19), which enter into the boundary conditions of the second and third kinds and in the solution to the first boundary value problem,

are defined by the relations [4]

$$\frac{\partial G}{\partial M_x} \equiv \sum_{i,\,j\,=\,1}^{n} a_{ij}(\mathbf{x},\,t)N_j\frac{\partial G}{\partial x_i},$$
$$\frac{\partial G}{\partial M_y} \equiv \sum_{i,\,j\,=\,1}^{n} a_{ij}(\mathbf{y},\,\tau)N_j\frac{\partial G}{\partial y_i}, \qquad (26)$$

where $\mathbf{N} = \{N_1, \ldots, N_n\}$ is the unit outward normal to the surface S. In the special case when $a_{i,i}(\mathbf{x}, t) = 1$ and $a_{i,j}(\mathbf{x}, t) = 0$ for $i \neq j$, operator (26) coincides with the usual operator of differentiation along the normal to the surface S.

If the coefficients of equation (23) and boundary condition (25) are independent of time t, then the Green's function takes the form $G(\mathbf{x}, \mathbf{y}, t, \tau) = G(\mathbf{x}, \mathbf{y}, t - \tau)$.

Remark. If boundary conditions of different types are imposed in certain domains of the surface $S = \sum_i S_i$, i.e.,

$$\Gamma^{(i)}_{\mathbf{x},\,t}[w] \;=\; g_i(\mathbf{x},\,t) \;\text{ for } \mathbf{x} \in S_i,$$

then the last term in solution (22) should be replaced by the sum

$$\sum_i \int_0^t \iint_{S_i} g_i(\mathbf{y},\,\tau)U_i(\mathbf{x},\,\mathbf{y},\,t,\,\tau)\,dS_y\,d\tau.$$

4. Hyperbolic equations with many variables. We consider a linear nonhomogeneous hyperbolic equation in n spatial variables which takes the general form

$$\frac{\partial^2 w}{\partial t^2} + \varphi(\mathbf{x},\,t)\frac{\partial w}{\partial t} - L_{\mathbf{x},\,t}[w] \;=\; \Phi(\mathbf{x},\,t), \qquad (27)$$

where the operator $L_{\mathbf{x},\,t}[w]$ is explicitly given by formula (19).

The solution to the boundary value problem in the domain V for equation (27) under the arbitrary nonhomogeneous initial conditions

$$w = f_0(\mathbf{x}) \text{ at } t = 0, \qquad (28)$$
$$\partial_t w \;=\; f_1(\mathbf{x}) \;\text{ at } t = 0 \qquad (29)$$

and arbitrary linear boundary condition (21) takes the form

$$w(\mathbf{x},\,t) \;=\; \int_0^t \iint_V \Phi(\mathbf{y},\,\tau)G(\mathbf{x},\,\mathbf{y},\,t,\,\tau)\,dV_y\,d\tau$$
$$- \int_V f_0(\mathbf{y})\left[\frac{\partial}{\partial\tau}G(x,\,y,\,t,\,\tau)\right]_{\tau\,=\,0} dV_y$$
$$+ \int_V [\,f_1(\mathbf{y}) + f_0(\mathbf{y})\varphi(\mathbf{y},\,0)\,]G(\mathbf{x},\,\mathbf{y},\,t,\,0)\,dV_y \qquad (30)$$
$$+ \int_0^t \iint_S g(\mathbf{y},\,\tau)U(\mathbf{x},\,\mathbf{y},\,t,\,\tau)\,dS_y\,d\tau.$$

Here, $G(\mathbf{x}, \mathbf{y}, t, \tau)$ is the Green's function satisfying both the homogeneous equation

$$\frac{\partial^2 G}{\partial t^2} + \varphi(\mathbf{x},\,t)\frac{\partial G}{\partial t} - L_{\mathbf{x},\,t}[G] \;=\; 0 \qquad (31)$$

with the semihomogeneous initial conditions

$$G = 0 \text{ at } t = \tau,$$
$$\partial_t G \;=\; \delta(\mathbf{x} - \mathbf{y}) \;\text{ at } t = \tau$$

and homogeneous boundary condition (25).

If the coefficients entering into equations (31) and boundary condition (25) are independent of time t, then the Green's function takes the form $G(\mathbf{x}, \mathbf{y}, t, \tau) = G(\mathbf{x}, \mathbf{y}, t - \tau)$.

The function $U = U(\mathbf{x}, \mathbf{y}, t, \tau)$ in the integrand of the last term in solution (30) is expressed in terms of the Green's function $G(\mathbf{x}, \mathbf{y}, t, \tau)$. For the boundary value problems of principal types, the corresponding formulas for U are listed in Table 2 (in the case of the third boundary value problem, the coefficient can depend on $\mathbf{x}$ and t). It is worth noting that the relation between the function U and the Green's function in the case of the boundary value problem for parabolic equation (18) is the same as that for hyperbolic equation (27) provided that the boundary conditions imposed are identical (naturally, the Green's functions for these problems are different).

ACKNOWLEDGMENTS

This work was supported by the Russian Foundation for Basic Research, projects nos. 00-02-18033 and 00-03-32055.

REFERENCES

1. H. S. Carslaw and J. C. Jaeger, *Conduction of Heat in Solids* (Clarendon Press, Oxford, 1959; Nauka, Moscow, 1964).
2. *Linear Equations of Mathematical Physics*, Ed. by S. G. Mikhlin (Nauka, Moscow, 1964; Holt, Rinehart and Winston, New York, 1967).
3. G. E. Shilov, *Mathematical Analysis: The Second Special Course* (Nauka, Moscow, 1965).
4. *Mathematical Éncyclopedia* (Sov. Éntsiklopediya, Moscow, 1977), Vol. 1, p. 1130.
5. A. G. Butkovskiĭ, *Green's Functions and Transfer Functions Handbook* (Nauka, Moscow, 1979; Horwood, Chichester, 1982).
6. V. F. Zaĭtsev and A. D. Polyanin, *Handbook on Partial Differential Equations: Exact Solutions* (Moscow, 1996).
7. A. D. Polyanin, A. V. Vyaz'min, A. I. Zhurov, and D. A. Kazenin, *Handbook on Exact Solutions to Equations of Heat-and-Mass Transfer* (Faktorial, Moscow, 1996).
8. A. N. Tikhonov and A. A. Samarskii, *Equations of Mathematical Physics* (Nauka, Moscow, 1972; Pergamon, Oxford, 1964).

Translated by V. Chechin

Doklady Physics, Vol. 45, No. 8, 2000, pp. 419–421. Translated from Doklady Akademii Nauk, Vol. 373, No. 5, 2000, pp. 632–634.

MECHANICS

On Invariants of the Stress–Strain State in Mathematical Models for Mechanics of Continua

Academician E. I. Shemyakin

Received March 14, 2000

In the mechanics of continua, it is usual practice to adopt the following standard set of invariants for a symmetric second-rank stress-state tensor regardless of the medium type (solid body, viscous fluid, etc.):

$$I_1 = \sigma_1 + \sigma_2 + \sigma_3,\ I_2 = \sigma_1\sigma_2 + \sigma_2\sigma_3 + \sigma_3\sigma_1,\quad I_3 = \sigma_1\sigma_2\sigma_3. \tag{1}$$

Here, the principal values of the stress tensor

$$\sigma_1, \sigma_2, \sigma_3 \tag{2}$$

and the trihedron for the principal directions of tensor σ_{ij} $(i, j = x, y, z)$ determine the stress state in a small volume of a continuous medium; and $\sigma_{ij} = \sigma_{ji}$ [1, 2].

It is generally believed in models that a change only in the second invariant is essential; effects of the first one for incompressible media and the third one associated with the type of a stress state are often ignored. As a result, the information on the principal-direction trihedron is lost. Thus, choosing the first and second invariants (for the stress deviator) does not call for information on principal directions.

A representation of invariants, which is similar to (1), is also used for the symmetric strain tensor or the strain rate tensor. In this case, a similarity of the stress tensor and strain (strain rate) one is adopted to relate invariants of a stress state to those of a strain (strain rate) state. Note that deviations from the similarity are both possible and natural in actual situations [3–5] (Fig. 1).

Taking into account these facts and proceeding from physical interpretation of the energy dissipation processes in models of plastic and viscous media, we propose to introduce another set of invariants related to areas of the maximum tangential stresses T and principal shears Γ (shear-strain rate). Data from solid-state physics and recent results obtained in mesomechanics [6] indicate these directions of investigation [7, 8].

In this case, in performing identity transformations, it is easy to pass from (2) to substantiating this new set of invariants:

$$\sigma_1 \geq \sigma_2 \geq \sigma_3,\ \sigma_n + T \geq \sigma_2 \geq \sigma_n - T,\quad T \geq \sigma_2 - \sigma_n \geq -T,\ 1 \geq \mu_\sigma \geq -1, \tag{3}$$

where

$$T = \frac{\sigma_1 - \sigma_3}{2},\ \sigma_n = \frac{\sigma_1 + \sigma_3}{2},$$

$$\mu_\sigma = \frac{\sigma_2 - \sigma_n}{T} = \frac{2\sigma_2 - \sigma_1 - \sigma_3}{T}\ (T \neq 0).$$

It is rather probable that the Lode–Nadai parameter μ_σ characterizing a type of the stress state was introduced in exactly the same manner.

We now make two comments concerning the new invariant set

$$T = \frac{\sigma_1 - \sigma_3}{2},\ \sigma_n = \frac{\sigma_1 + \sigma_3}{2},\ \mu_\sigma, \tag{4}$$

which completely specifies the stress state in an elementary volume of the medium. In other words, the following statement is valid: Three invariants (4) are necessary and sufficient to specify the stress state in an elementary volume of a continuum.

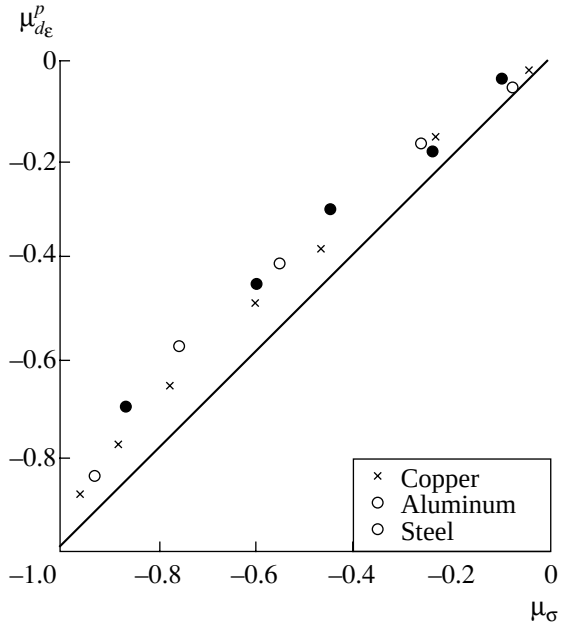

Fig. 1. Lode parameter of the plastic-strain increment tensor as a function of the same parameter for the stress tensor.

1028-3358/00/4508-0419$20.00

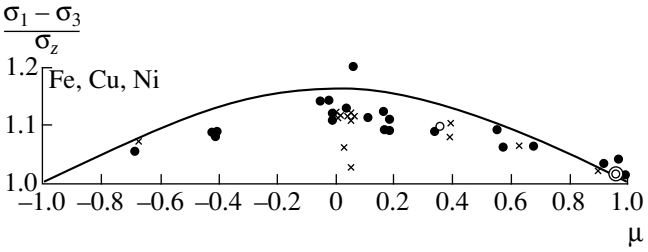

Fig. 2. Relative value of the maximum tangential stress as a function of the Lode parameter (σ_z is the ultimate strength at the uniaxial tension).

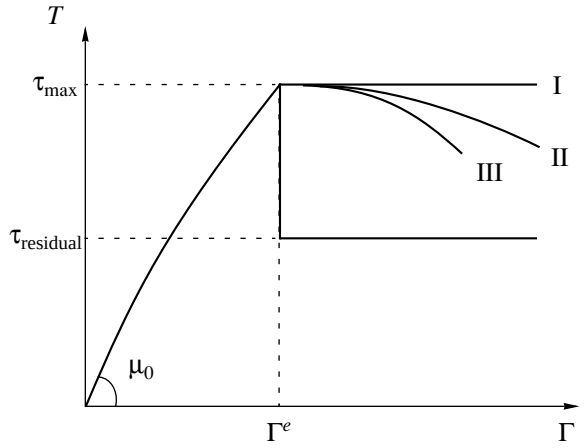

Fig. 3. Illustration of the descending branch of the maximum tangential stress on the principal strain diagram (at the uniaxial tension).

The first comment is associated with the fact that the condition of isotropy for set (1), which is understood that it does not depend on directions of the principal axes, was never discussed while introducing invariants (except for rare cases when the third invariant should be taken into account). Actually, allowing for the first and second invariants did not require an account for the orientation of the principal-direction trihedron of the stress tensor.

In contrast to this, introducing set (4) definitely indicates such a dependence, because the invariant T is related to area elements for maximum tangential stresses, which bisect angles between the first and the third principal directions. The invariant σ_n is independent of principal directions, while the invariant μ_σ, as well as T, is closely related to the orientation of the principal axis and indicates the influence of other (two) extreme tangential stresses

$$T_{23} = \frac{\sigma_2 - \sigma_3}{2}, \quad T_{12} = \frac{\sigma_1 - \sigma_2}{2}, \tag{5}$$

because

$$\mu_\sigma = \frac{T_{23} - T_{12}}{T}.$$

It is well known that for a uniaxial tension (biaxial compression)

$$\mu_\sigma = 1,$$

while in the case of a torsion,

$$\mu_\sigma = 0.$$

This implies that the role of areas with tangential stresses (5) increases at $\mu_\sigma \neq 1$ compared to the case $\mu_\sigma = 0$. Considering the data of [4] (Fig. 2) in this context, we emphasize that the necessity of introducing the smooth plasticity conditions of the Huber–Mises type does not follow from these Lode–Nadai data. However, allowance for the Lode–Nadai parameter, i.e., for the type of the stress state, turns out to be necessary ($1 \geq \mu_\sigma \geq -1$).

Thus, it is stated that introducing these three invariants, T, σ_n, and μ_σ enables us to describe anisotropy of the resistance to shears, which arises at irreversible strains and failure. Moreover, owing to this, we are able to construct a mathematical model for the deformation of solid bodies, which is adequate to physical processes [6–8]. In the case under consideration, principal facts used as the basis for the construction of this model are the experimental relationship between the maximum tangential stress and principal torsional shear (for $\mu_\sigma = 0$) and attraction to the consideration (in accordance with the data of Fig. 2) of other area elements with extreme tangential stresses in accordance with the values of the Lode–Nadai parameter. Note, that the same experimental law $T = T(\Gamma)$ valid for principal elementary areas manifests itself for these areas (Fig. 3).

In recent years, wide attention was attracted in geophysics and geomechanics to studying ordered block structures in massifs, and the hierarchy of these structures was revealed [7, 8]. Thus, they establish the existence and development of blocks that are closely related with areas of maximum tangential stresses and principal shears, which were mentioned above. In this connection, it should be pointed out that, from the physical standpoint, the set of invariants proposed describes most closely the deformation of a massif under the action of technogenic and tectonic loads. Apparently, as is shown by investigations in the strength of solid bodies conducted by the School of Academician V.E. Panin, it is also reasonable to follow this route in the mechanics of deformable solid body.

The proposed model allows us to confidently trace a certain important phenomenon, namely, the behavior of a material in the supercritical state. In fact, after the maximum value of the tangential stress has been attained for a material, a practically new material arises, whose behavior calls for different description [10, 11, 13]. Nevertheless, the laws of mechanics (laws of mass, momentum, and energy conservation) remain valid. It is these laws that determine the material properties in the post-ultimate (post-peak) state. When the extreme (for a given body) value of the principal shear

($\Gamma = \Gamma_e$) is attained, this shear value is preserved in an elementary volume, and the growth of the domain of irreversible deformations (and failures) occurs only at the expense of an increase in an amount of such elements. The fact that other extreme area elements come into play, in accordance with Fig. 2 and in correspondence to the same law [$T = T(\Gamma)$], determines the residual strength of the material.

In order to illustrate the proposed synthetic model, we present the system of basic equations for the problem of the plane deformation of a solid body [10, 13]. Papers [10, 11] contain the preliminary results concerning the statement of new boundary value problems on the basis of the models developed. For example, new equations describing irreversible deformation can be derived on the basis of the model proposed for the case of the plane deformation of an elastoplastic body (here, the usual notation is used):

$$\begin{aligned} \frac{\partial\hat{\omega}}{\partial x} - \cos 2\psi\frac{\partial\psi}{\partial x} + \sin 2\psi\frac{\partial\psi}{\partial y} &= 0, \\ \frac{\partial\hat{\omega}}{\partial y} + \sin 2\psi\frac{\partial\psi}{\partial x} + \cos 2\psi\frac{\partial\psi}{\partial y} &= 0, \end{aligned} \tag{6}$$

where

$$\omega = \frac{1}{2}\left(\frac{\partial v}{\partial x} - \frac{\partial u}{\partial y}\right), \quad \tan 2\psi = \frac{\varepsilon_{xy}}{\varepsilon_y - \varepsilon_x}, \quad \frac{2\omega}{\Gamma_e} = \hat{\omega}.$$

This system is of the hyperbolic type and has two families of real characteristics

$$\frac{dy}{dx} = -\tan\psi, \quad \frac{dy}{dx} = \cot\psi \tag{7}$$

with the following relationships for them:

$$\omega + \psi = \alpha = \text{const}, \quad \omega - \psi = \beta = \text{const}. \tag{8}$$

It is easy to see a close analogy between the new system for strains and the classical Saint-Venant system for stresses. Apparently, it is this analogy that was indicated by Academician S.A. Christianovich in his famous paper [12].

From the practical standpoint, the results presented, including new equations for the plane problem (6) and (7), (8), allow us to consider from a new standpoint the boundary value problem for the brittle failure [10, 11, 13] and for a press tool on a compliant (with allowance for irreversible strains) base.

REFERENCES

1. A. A. Il'yushin, Uch. Zap. Mos. Gos. Univ. **39** (1940).
2. V. V. Novozhilov, Prikl. Mat. Mekh. **15** (2) (1951).
3. L. M. Kachanov, *Principles of Plasticity Theory* (Nauka, Moscow, 1969).
4. A. Nadai, *Plasticity; Mechanics of the Plastic State of Materials* (McGraw-Hill, New York, 1931; ONTI SSSR, Moscow, 1936).
5. S. A. Khristianovich and E. I. Shemyakin, Izv. Akad. Nauk SSSR, Mekh. Tverd. Tela, No. 4, 87 (1967); No. 5, 138 (1969).
6. *Physical Mesomechanics and Computer Designing Materials*, Ed. by V. E. Panin (Nauka, Novosibirsk, 1995).
7. A. F. Revuzhenko, S. B. Stazhevskiĭ, and E. I. Shemyakin, Fiz. Tekh. Probl. Razrab. Polezn. Iskop., No. 3, 130 (1974).
8. A. F. Revuzhenko, Fiz. Tekh. Probl. Razrab. Polezn. Iskop., No. 2, 9 (1974).
9. Yu. I. Yagn, Vestn. Inzh. Tekh., No. 6 (1931).
10. E. I. Shemyakin, Izv. Akad. Nauk, Mekh. Tverd. Tela **32** (2), 145 (1997).
11. A. F. Revuzhenko and E. I. Shemyakin, Prikl. Mekh. Tekh. Fiz., No. 2, 128 (1979).
12. S. A. Khristianovich, Mat. Sb. **1** (4), 512 (1936).
13. E. I. Shemyakin, Fiz. Mezomekh. **2** (6) (1999).

Translated by V. Devitsyn

Doklady Physics, Vol. 45, No. 8, 2000, pp. 422–424. Translated from Doklady Akademii Nauk, Vol. 373, No. 6, 2000, pp. 759–761.

MECHANICS

Undular Bore in the Counterflow

V. I. Bukreev

Presented by Academician V.M. Titov December 5, 1999

Received December 20, 1999

In this paper, we call an *undular bore* a free plane (as a rule, nonlinear) gravity wave, whose free surface level passes from its lower to higher value executing gradually convergent oscillations, rather than monotonically or by a jump. The term *undular wave* has a broader meaning and includes the case of stimulated waves. An undular wave may be smooth, with the collapsing first crest or several collapsing first crests. An example of recording a smooth undular bore, which was performed by a stationary wavemeter, is presented in Fig. 1.

We have not managed to obtain adequate analytical representations for undular waves due to their nonlinearity and unsteadiness. Incomplete available information on undular waves is based on physical and numerical experiments. The majority of investigations are devoted to the undulating hydraulic jump [1]. Detailed experiments with free undular waves in a channel were conducted in [2]. An example of numerical experiments based on the Navier–Stokes equations is represented by the paper [3]. Mathematical models yielding solutions of the undular-bore type with the collapsing leading edge were proposed in [4].

Below, we present some results of a physical experiment, which are useful to qualitively compare the inner structure of the undular bore with the results of numerical calculations based on different mathematical models. Here, by the term *inner structure*, we imply a random ensemble of trajectories (limited in time) of labeled particles.

The statement of the problem is clarified in Fig. 1. A steady nonuniform turbulent flow with the constant volumetric rate Q was created in a rectangular channel with the length of 3.8 m and the width $B = 6$ cm with the plane horizontal bottom. The following notation is used therewith: $h(x, t)$ is the depth of the undisturbed flow, h_0 is the depth ahead of the leading edge, x is the longitudinal coordinate, Δz is the deviation of the free surface from the equilibrium position, t is time, Δt is the exposition time per one frame at photographing, and $V = Q/Bh$. In the examples presented below, the flow was subcritical, h decreased monotonically, and V increased downstream.

At $t = 0$, the flow was stopped in the cross section $x = 0$ by a rapidly dropping gate. Trajectories of labeled micron-size particles (i.e., particles of aluminum powder) were recorded with a photographic camera and video camera. In contrast to the PIV-method [5] that has recently become popular, the time of exposure for each frame was taken on purpose greater: It ranged from 1/60 to 1/2 s. This made it possible to trace trajectories of individual particles for a sufficiently long time, although the shape of the free surface was strongly distorted. Information on the shape of the free surface was obtained by the video recording, which determined $\Delta z(x)$ at a fixed t, and also by stationary wavemeters recording $\Delta z(t)$ for fixed x. The velocity of the longitudinal displacement c for the height-averaged point of the wave leading edge was calculated according to signals of two wavemeters spaced by $\Delta x = 30$ cm apart. Henceforth, this quantity is referred to as the bore propagation velocity.

One new interesting result of measurements with wavemeters is the following. Previously, in experiments with initially stagnant fluid, it was found [6] that, in contrast to predictions of the first approximation of the shallow-water theory, undular waves retained their smoothness, while passing by the first critical velocity

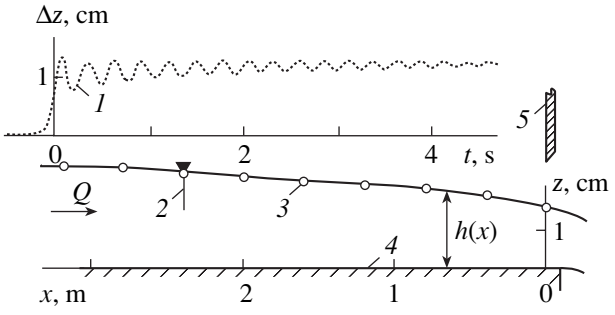

Fig. 1. Unperturbed flow and undular bore for $Q = 0.323$ l/s: (*1*) $\Delta z(t)$ at $x = 210$ cm; (*2*) wavemeter; (*3*) unperturbed free surface; (*4*) channel bottom; (*5*) gate; for (*1*), $h_0 = 2.8$ cm; $c_{1*} = 33.2$ cm/s; $c = 40$ cm/s; and $c_{2*} = 48.9$ cm/s.

Lavrent'ev Institute of Hydrodynamics, Siberian Division, Russian Academy of Sciences, pr. Akademika Lavrent'eva 15, Novosibirsk, 630090 Russia

1028-3358/00/4508-0422$20.00 © 2000 MAIK "Nauka/Interperiodica"

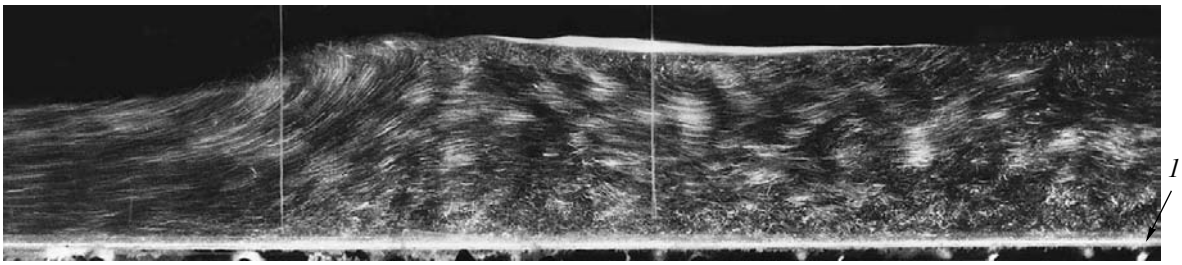

Fig. 2. Bore structure for $Q = 0.648$ l/s (the bore propagates leftwards). In Figs. 2–4, *1* is the channel bottom. For scale lines $x = 230$ and 240 cm, $h_0 \simeq 3.55$ cm; $\Delta t = 1/15$ s; $V = 30.5$ cm/s; $c = 44 \pm 1.5$ cm/s; $c_{1*} = 28.5$ cm/s; $c_{2*} = 46.2$ cm/s.

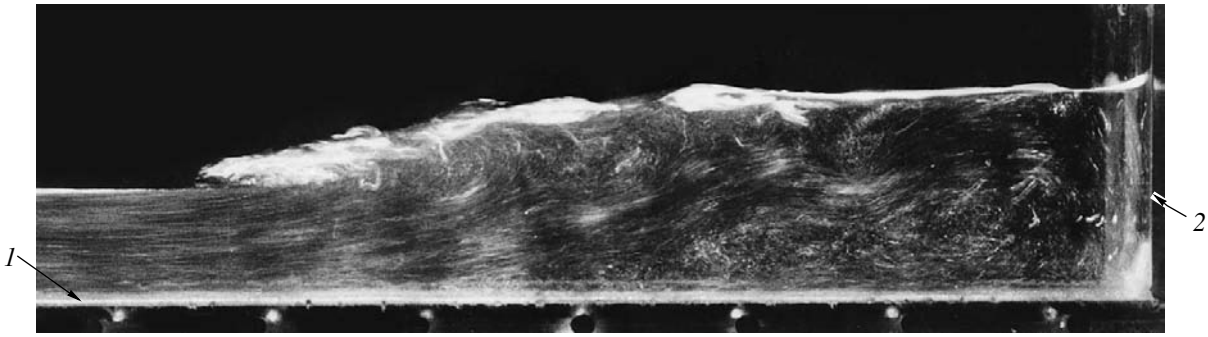

Fig. 3. Initial stage of developing the bore presented in Fig. 2: (*1*) channel bottom; (*2*) the gate. For the middle of the leading edge, $x = 18$ cm and $\Delta t = 1/15$ s.

$c_1 = \sqrt{gh}$ and began to collapse at the greater second critical velocity. A good quantitative measure of the latter is the ultimate propagation velocity of solitary waves, $c_2 = 1.294\sqrt{gh}$, which was derived in [7] from the complete system of equations for the potential motion. These experiments confirmed the result for waves across the counterflow as well. Note that, in the first approximation, the first and second critical velocities can be defined as $c_{1*} = \sqrt{gh} - V$ and $c_{2*} = 1.3\sqrt{gh} - V$, respectively. For example, the condition $c_{1*} < c < c_{2*}$ is valid for the plot *1* in Fig. 1, and a wave retained its smoothness.

The most important result obtained by photographing consists in the following. In the counterflow, the severe vertical stratification of the particle-motion velocity occurs in the fluid under the undular bore. A sufficiently thick boundary layer of the damped fluid is formed near the bottom. Above this layer, particles continue to move in the previous direction with velocities on the order of V forming a twisting jet. In a collapsing wave, damping of the incoming flow also takes place in the near-surface layer. The unsteadiness and collapsing result in the fact that the separation into domains of damped and moving fluid has an alternating character in both time and space. Photographs (Figs. 2, 3) are presented as illustrations.

In Fig. 2, a wave is shown in the transition state between the smooth and collapsing forms. The wave leading edge has collapsed at $x < 210$ cm. Then, it became smooth but the *corner point*, characteristic for the critical state, retained on its frontal slope rather than on the wave crest, as is the case in the theory of standing or solitary waves with the ultimate amplitude. The comparison of the values of c, c_{1*}, c_{2*} placed underneath the photograph confirms the aforesaid about the conditions for the transition from collapsing waves to smooth undular ones.

At the initial stage of the bore evolution (Fig. 3), apart from the clearly defined stratification into the jet and the stagnant zone, the formation of vortices near the free surface and collapsing of the leading edge, which are accompanied by an intense involvement of air into water, do occur.

A photograph of the head part of the undular bore propagating in the fluid stagnant ahead of it is presented for comparison in Fig. 4. A perturbance was introduced by removing a partition creating the level difference Δh. In this example, the condition $c_1 < c < c_2$ was fulfilled, and the wave was smooth. Its inner structure is considerably simpler than in the case of the propagation across the counterflow. In particular, particle trajectories under the wave first crest are quite similar to those for a solitary wave [8]. The structure of a collapsing undular wave propagating in stagnant fluid is con-

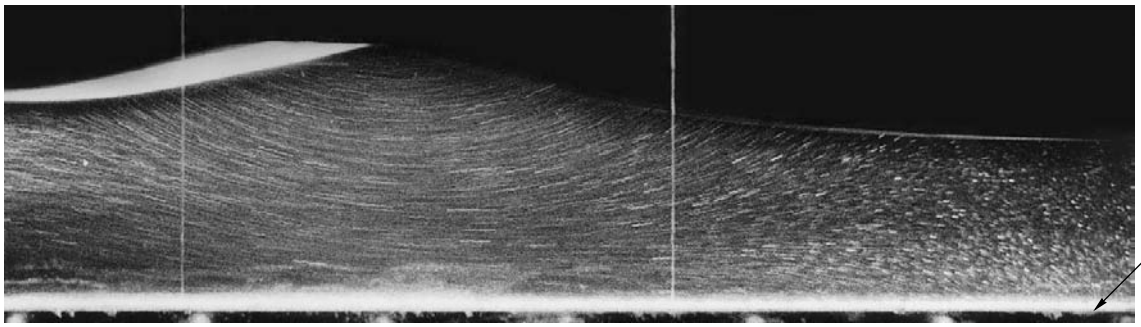

Fig. 4. Bore structure for the stagnant fluid (the bore propagates rightwards): *1* is the channel bottom. For the scale lines $x = 210$ and 220 cm, $\Delta t = 1/30$ s; $h_0 = 3.5$ cm; $\Delta h = 3.2$ cm; $c = 71.5$ cm/s; $c_1 = 58.6$ cm/s; and $c_2 = 76.2$ cm/s.

siderably simpler than in the presence of the counterflow.

ACKNOWLEDGMENTS

The author is grateful to A.V. Gusev for his assistance in photographing.

This study was supported by the Russian Foundation for Basic Research, project no.98-01-00750.

REFERENCES

1. Ven Te Chow, *Open-Channel Hydraulics* (McGraw Hill, New York, 1959).
2. H. Favre, *Ondes de translation dans les canaux decoverts* (Dunod, Paris, 1935).
3. C. M. Lemos, Int. J. Numer. Meth. Fluids **23**, 545 (1996).
4. V. Yu. Lyapidevskiĭ, Prikl. Mekh. Tekh. Fiz. **39** (2), 40 (1998).
5. R. J. Adrian, Ann. Rev. Fluid Mech. **23**, 261 (1991).
6. V. I. Bukreev and A. V. Gusev, Izv. Akad. Nauk, Mekh. Zhidk. Gaza, No. 1, 82 (1999).
7. M. S. Longuet-Higgins and J. D. Fenton, Proc. R. Soc. London, Ser. A **340**, 471 (1974).
8. J. W. Daily and S. C. Stephan, Jr., in *Proceedings of the III Conference on Coastial Engineering* (Univ. of California, Berkley, 1952), p. 13.

Translated by V. Devitsyn

Doklady Physics, Vol. 45, No. 8, 2000, pp. 425–429. Translated from Doklady Akademii Nauk, Vol. 373, No. 6, 2000, pp. 762–766.

MECHANICS

Integration of Equations for Long Waves in the Drozdova–Kulikovskiĭ Form

A. G. Petrov

Presented by Academician G.G. Chernyĭ December 23, 1999

Received December 27, 1999

1. The Drozdova–Kulikovskiĭ equations for long-wave approximation. While deriving the Boussinesq equations, two small parameters are usually assumed to exist: the depth-to-wavelength ratio and the amplitude-to-depth one [2]. The derivation of the Boussinesq equations for fluid flow in channels [1] does not assume the smallness of the second parameter and is as follows.

The mass and momentum conservation laws for the potential flow of perfect incompressible fluid in a horizontal channel of an arbitrary cross section are written out as

$$\frac{\partial S}{\partial t} + \frac{\partial Su}{\partial x} = 0, \quad S\left(\frac{\partial u}{\partial t} + u\frac{\partial u}{\partial x}\right) = -\frac{\partial P}{\partial x}. \qquad (1.1)$$

Here, t is time; x is the coordinate along the bed axis; u is the velocity along the bed axis, which is averaged over the cross section; P is the sum (divided by the density) of the pressure forces in the cross section; and S is the flow cross-section area.

The function P is determined in [1] by application of the Lagrange generalized coordinates to a certain fluid volume. We isolate a fluid element $x_0 - l/2 \le x \le x_0 + l/2$ of a small width l and with the cross section S (see Fig. 1). This fluid element moves in the flow being deformed. The element deformation is ignored, so that the lateral faces of the element remain parallel. S is taken as the generalized coordinate of the element, and the Lagrange equation is written out:

$$\frac{\delta L}{\delta S} = -Q_S, \quad \frac{\delta L}{\delta S} = \frac{\partial L}{\partial S} - \frac{d}{dt}\frac{\partial L}{\partial \dot S} + \frac{d^2}{dt^2}\frac{\partial L}{\partial \ddot S} - \ldots.$$

On the left-hand side, there is the variational derivative of the Lagrange function. This function $L = T - U$ is equal to the difference between the kinetic and potential energies of the fluid element and depends on S and time derivatives $\dot S$, $\ddot S$. The function L depends also on the size l, which is expressed in terms of S by the relation $Sl = V$ = const. The pressure is calculated by considering the work $\rho P\delta l = -Q_S\delta S$ under the transverse tension of the element filled with incompressible fluid

$$P = \frac{SQ_S}{\rho l} = -\frac{S}{\rho l}\frac{\delta L}{\delta S}. \qquad (1.2)$$

Equations (1.1) and (1.2) with the additional condition $Sl = V$ = const have been obtained in [1]. In the case of the calculated function $L(\ddot S, \dot S, S)$, they form the desired closed system of the Boussinesq equations for determining u and S.

Taking into account the constant value of the volume V, it is more convenient to express the total pressure in terms of the variational derivative for the function $L/(\rho V)$, the layer width l not entering into this derivative. As a result, we obtain the closed system of two equations

$$\frac{\partial S}{\partial t} + \frac{\partial Su}{\partial x} = 0,$$
$$S\left(\frac{\partial u}{\partial t} + u\frac{\partial u}{\partial x}\right) = \frac{\partial}{\partial x}\left[S^2\frac{\delta}{\delta S}\left(\frac{L}{\rho V}\right)\right]. \qquad (1.3)$$

Approximation (1.3) can be shown to be the first term of the asymptotic series in the derivatives S, $\dot S$, $\ddot S$, …. The second term of the series is obtained by introduc-

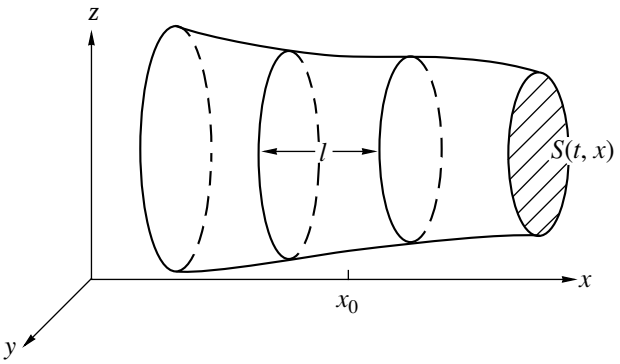

Fig. 1.

Institute of Problems in Mechanics,
Russian Academy of Sciences,
pr. Vernadskogo 101, Moscow, 117526 Russia

1028-3358/00/4508-0425$20.00 © 2000 MAIK “Nauka/Interperiodica”

ing the second generalized coordinate determining the fluid-element deformation, etc.

2. An integral of steady motion. If the function $L/(\rho V)$ does not explicitly depend on t and x, three integrals of system (1.3) can be found for a steady motion. Two of them are the constant flow rate and the Bernoulli integral:

$$Su = Q, \quad -\frac{Q^2}{S} + S^2\frac{\delta}{\delta S}\left(\frac{L}{\rho V}\right) = A_1.$$

The Bernoulli integral can be written out in the form of the Lagrange equations or of the Hamilton principle, which is equivalent to these equations:

$$\frac{\delta}{\delta S}\left(\frac{L}{\rho V} + \frac{Q^2}{2S^2} + \frac{A_1}{S} + A_2\right)$$

$$= 0 \Rightarrow \delta\int_{-\infty}^{\infty}\left(\frac{L}{\rho V} + \frac{Q^2}{2S^2} + \frac{A_1}{S} + A_2\right)dt = 0.$$

Since the Lagrange function depends only on the generalized coordinate S and its derivatives and does not depend explicitly on time, the Lagrange equations obtained have a third energy integral. It is more convenient to express this integral in terms of x-dependent functions. To do this, we make use of the substitution $dt = (S/Q)dx$, $\dot{S} = QS'/S$ (the prime denotes the derivative with respect to x) in the action integral. Then, the Hamilton principle transforms to the form

$$\delta\int_{-\infty}^{\infty}\Lambda dx = 0, \quad \Lambda = \Lambda_0 + \frac{Q^2}{2S} + A_1 + A_2S,$$
$$\Lambda_0(S'', S', S) = \frac{L}{\rho l}. \tag{2.1}$$

The Euler–Lagrange equations corresponding to principle (2.1) have the energy integral

$$-S'\frac{d}{dx}\frac{\partial\Lambda_0}{\partial S''} + S''\frac{\partial\Lambda_0}{\partial S''} + S'\frac{\partial\Lambda_0}{\partial S'} - \Lambda_0$$
$$= \frac{Q^2}{2S} + A_1 + A_2S, \tag{2.2}$$

in which all three arbitrary constants Q, A_1, and A_2 are transferred to the right-hand side. For periodic waves, these three constants are expressed in terms of wave parameters, such that the amplitude a, wavelength λ, and mean depth H. Furthermore, the dependence of the wave-propagation velocity on the wave parameters is found from the relation between the flow rate and a, λ, and H.

Examples of exact solutions to steady-state equations (1.3) obtained with general integral (2.2) are presented below.

3. Solitary waves in channels. Methods for calculating the kinetic energy

$$\frac{T}{\rho l} = \frac{1}{2}\int_S (v_y^2 + v_z^2)dy\,dz$$

in a channel cross section of an arbitrary form are presented in [1]. Here, y and z are the Cartesian coordinates in the channel cross section; the z-coordinate being directed vertically upwards; and v_y, v_z are the corresponding components of the velocity for fluid particles. The integration is carried out over the wetted area of the cross section.

The velocity field has a potential φ, which is determined from the solution of the boundary value problem for the Poisson equation

$$\frac{\partial^2\varphi}{\partial z^2} + \frac{\partial^2\varphi}{\partial y^2} = \frac{\dot{S}}{S} = \frac{QS'(x)}{S^2}.$$

The kinetic energy was calculated exactly in [1] for channels of the rectangular and triangular shapes. For shallow and narrow channels, approximate asymptotic formulas were obtained.

The potential energy U includes the energy U_g of the gravity force and may contain, in addition, the surface tension energy U_σ or the energy U_E of elastic film at the fluid surface:

$$U = U_g + U_\sigma + U_E, \quad \frac{U_g}{\rho l} = Sgz_c,$$

$$\frac{U_\sigma}{\rho l} = \frac{b\sigma(\sqrt{1+h'^2} - 1)}{\rho} \approx \frac{b\sigma}{2\rho}(h')^2, \tag{3.1}$$

$$\frac{U_E}{\rho l} = \frac{bEI}{2\rho}(h'')^2.$$

Here, z_c is the vertical coordinate of the geometric center for the wetted cross section; S is the cross-section area, which is a function of the depth $S(h)$ for a channel of a given shape; $b = S_h$ is the width of the free surface; σ is the coefficient of surface tension; E, I are the Young's modulus and moment of inertia of the elastic film, respectively.

Thus, the method developed in the present paper allows us to find exact solutions to the Boussinesq equations for capillary-gravitation waves in channels and for waves with an elastic film.

We consider solutions for solitary waves with the condition imposed at infinity: $h \longrightarrow h_\infty$ as $x \longrightarrow \pm\infty$.

We introduce the dimensionless coordinates of the wave profile X, Y and the wave velocity c:

$$X = \frac{x}{h_\infty}, \quad Y = \frac{h}{h_\infty}, \quad c^2 = \frac{Q^2}{gh_\infty S_\infty} = \frac{v_\infty^2}{gh_\infty}. \quad (3.2)$$

Here, the flow rate is expressed in terms of the cross-section area S_∞ and the fluid velocity at the infinity ($Q = S_\infty v_\infty$).

For a rectangular channel with a unit width and free surface, the cross-section area is $S = h$. The kinetic and potential energies are calculated exactly:

$$\frac{T}{\rho l} = \frac{1}{6}h\dot{h}^2 = \frac{Q^2(h')^2}{6h}, \quad \frac{U}{\rho l} = \frac{1}{2}gh^2, \quad \Lambda_0 = \frac{T-U}{\rho l}. \quad (3.3)$$

Substituting Λ_0 in energy integral (2.2), we arrive at the equation

$$\frac{Q^2(h')^2}{6h} + \frac{1}{2}gh^2 = \frac{Q^2}{2h} + A_1 + A_2 h,$$

whose integration is carried out completely by the method of separation of variables. For periodic waves, we obtain the well-known solution expressed in terms of elliptic functions [3].

For solitary waves, the energy integral can be reduced in terms of dimensionless variables (3.2) to the form

$$(Y')^2 = 3\left(1 + A_1 Y + A_2 Y^2 - \frac{Y^3}{c^2}\right) = 3\left(1 - \frac{Y}{c^2}\right)(Y-1)^2. \quad (3.4)$$

From this expression, the constants A_1, A_2 are determined and the relation between the wave velocity and the dimensionless amplitude a related to the depth h_∞ is found:

$$c = \frac{Q}{\sqrt{gh_\infty^3}} = \sqrt{1+a} = 1 + \frac{1}{2a} - \frac{1}{8a^2} + \ldots. \quad (3.5)$$

The exact trinomial expansion

$$c = 1 + \frac{1}{2a} - \frac{1}{8a^2} - \frac{1}{40a^2} + \ldots$$

[4, 6] differs insignificantly from approximation (3.5).

The problem of a solitary wave in a triangular channel with the cross-section shape $z = p|y|$ is solved equally easily. The cross-section area for such a channel is equal to $S = h^2/p$. The exact expressions for the kinetic and potential energies are written out [1] as

$$\frac{T}{\rho l} = \frac{Q^2(h')^2}{12h^2 p}, \quad \frac{U}{\rho l} = \frac{2h^3 g}{3p}, \quad \Lambda_0 = \frac{T-U}{\rho l}.$$

Energy integral (2.2) is reduced, in terms of dimensionless variables (3.2), to the form

$$\frac{1+3p^2}{6p^2}(Y')^2 = 1 + A_1 Y^2 + A_2 Y^4 - \frac{4Y^5}{3c^2} = \left(1 - \frac{Y}{1+a}\right)(Y-1)^2\left(1 + AY + \frac{4(1+a)}{3c^2}Y^2\right).$$

In the expansion in terms of powers of Y, the coefficients of Y and Y^3 are zeros. Thus, we find the constant A and the velocity c:

$$A = \frac{3+2a}{1+a},$$

$$c\sqrt{2} = \frac{1+a}{1+a/2}\sqrt{1+\frac{2a}{3}} = 1 + \frac{5}{6}a - \frac{5}{36}a^2 + \ldots = \frac{v_\infty\sqrt{2}}{\sqrt{gh_\infty}}.$$

4. Capillary-gravitational solitary waves. In the rectangular channel, the wave under consideration can be described by the Froude and Weber dimensionless numbers

$$\mathrm{G} = \frac{gh_\infty}{v_\infty^2}, \quad \mathrm{W} = \frac{\sigma}{\rho h_\infty v_\infty^2}.$$

We determine the Lagrange function $L = T - U_g - U_\sigma$ from (3.1) and (3.3) and substitute it into (2.1). Then, in terms of dimensionless variables (3.2), variational principle (2.1) and energy integral (2.2) take the form

$$\delta\int_{-\infty}^{\infty}\Lambda(Y', Y)dx = 0, \quad (4.1)$$

$$\Lambda = \frac{(Y')^2}{6Y}(1 - 3\mathrm{W}Y) + \frac{3}{Y}(1 - \mathrm{G}Y)(Y-1)^2,$$

$$(Y')^2 = 3(Y-1)^2\frac{1-\mathrm{G}Y}{1-3\mathrm{W}Y}, \quad \mathrm{G} = \frac{1}{c^2}. \quad (4.2)$$

The energy equation for solitary wave (3.4) follows from (4.2) for $\mathrm{W} = 0$. The employment of variational principle (4.1) for a capillary-gravitation wave is an essential adjunct, because it allows for the discovery of new solutions with a discontinuous derivative. In this case, it is insufficient to solve equation (4.2). It is essen-

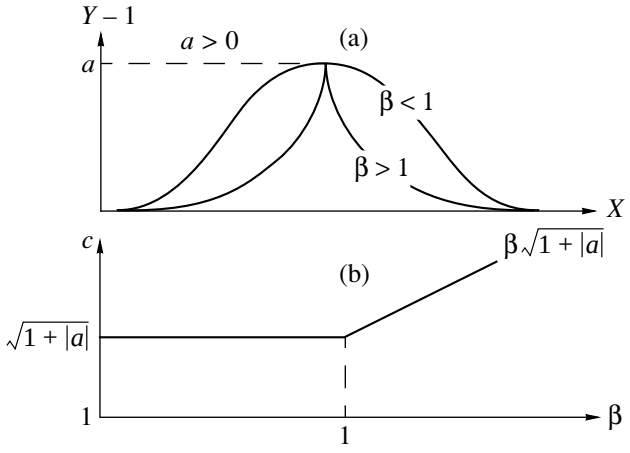

Fig. 2.

tial that, at the discontinuity point of solution (4.2), the Weierstrass–Erdman conditions should be satisfied, i.e., the conditions of the continuity of the momentum $\Lambda_{Y'}$ and energy $Y'\Lambda_{Y'} - \Lambda$. Solution (4.2) satisfies the latter condition automatically. When these conditions are fulfilled, the solution realizes the extremum of functional (4.1), i.e., the minimum for $\Lambda_{Y'Y'} \geq 0$ and the maximum for $\Lambda_{Y'Y'} \leq 0$.

The general solution to equation (4.2), which satisfies the conditions $Y \to 1$ for $X \to \pm\infty$, has the parametric representation

$$\pm\sqrt{3}X = -\beta\ln\left|\frac{1+\beta t}{1-\beta t}\right| + B\ln\left|\frac{1+Bt}{1-Bt}\right|,$$

$$Y = c^2\frac{1-t^2}{1-\beta^2t^2}, \quad \beta^2 = \frac{3W}{G} = \frac{3\sigma}{\rho g h_\infty^2}, \qquad (4.3)$$

$$B = \sqrt{\frac{1-3W}{1-G}}.$$

The point $X = \infty$ corresponds to the parameter value $t = 1/\beta$; the values $t = 0$ or $t = \infty$ correspond to the point $X = 0$. Therefore, the range of values for the parameter t is confined by the intervals $t \in [0, 1/\beta$ (smooth solitons) or $t \in (1/\beta, \infty)$ (discontinuous solitons).

It is more convenient to introduce the wave amplitude a and the Bond number $\beta > 0$ instead of the wave parameters G and W. The range of values for the parameters a and β breaks down into two regions corresponding to $a(1-\beta) > 0$ and $a(1-\beta) < 0$ in which waves have quantitative distinctions.

Smooth solitons, $a(1-\beta) > 0$. The parameter t varies within the limits $0 \leq t < 1/B$; the numbers G, W, and B depend on a and β as

$$G = \frac{1}{1+a}, \quad W = \frac{\beta^2}{3(1+a)}, \quad B = \sqrt{\frac{1+a-\beta^2}{a}},$$

the wave velocity is β-independent and equals $c = \sqrt{1+a}$. The solitons are symmetric with respect to the point $X = 0$ and have a smooth profile. In the vicinity of $|X| \ll 1$, the profile is parabolic:

$$Y = 1 + a - \frac{3a^2X^2}{4(1-\beta^2)(1+a)}. \qquad (4.4)$$

For $\beta < 1$, the solitons have the positive amplitude $a > 0$ (elevation); for $\beta > 1$, the amplitude is negative, i.e., $a < 0$ (inverse soliton). The effect of the soliton inversion for the Weber number exceeding a certain threshold value was noted in the numerical studies [7]. For periodic waves, this effect was mentioned in [8]. In the analytic investigation [9], the threshold value for the Weber number $W = 1/3G$ was found, wherein the sign of the soliton amplitude changes. The analytic solution for the inverse soliton in the case of a large value of the surface-tension coefficient was obtained in [10].

Solitons with discontinuity of a tangent, $a(1-\beta) < 0$. The parameter t varies within the limits $1/\beta < t < \infty$; the numbers G, W, and B are determined by the formulas

$$G = \frac{1}{\beta^2(1+a)}, \quad W = \frac{1}{3(1+a)},$$

$$B = \sqrt{\frac{a}{1+a-1/\beta^2}},$$

the wave velocity depends linearly on the Bond number $c = \beta\sqrt{1+a}$. Solitons are also symmetric with respect to the point $X = 0$, but the derivative $Y'(X)$ has a second-kind discontinuity. For $|X| \ll 1$, the velocity profile is of another asymptotic form:

$$Y = 1 + a - 3a\left[\frac{(\beta^2-1)(1+a)}{4\beta^2a}X^2\right]^{1/3}. \qquad (4.5)$$

The fulfillment of the Weierstrass–Erdman conditions is easily verified. Therefore, the solution obtained with a discontinuity of the tangent at $X = 0$ is an extremal for the functional in (4.1). In the extremal, for $a > 0$, the condition $\Lambda_{Y'Y'} \geq 0$ is met and the minimum of the action functional in (4.1) is realized; for $a < 0$ and $\Lambda_{Y'Y'} \geq 0$, the maximum of the functional is realized.

In Fig. 2a, the elevation-soliton profiles for constant positive amplitude and various Bond numbers are shown. As β increases, the soliton area decreases, and the curvature at the vertex monotonically increases to infinity as $\beta \longrightarrow 1$. For $\beta > 1$, solitons have vertical tangent at the vertex and the derivative Y' becomes infinite. At a constant positive amplitude, the soliton dimensionless velocity c is β-independent for $\beta < 1$ and is proportional to β for $\beta > 1$ (see Fig. 2b).

Figure 3a shows the profiles of the inverse solitons at the constant negative amplitude and various Bond

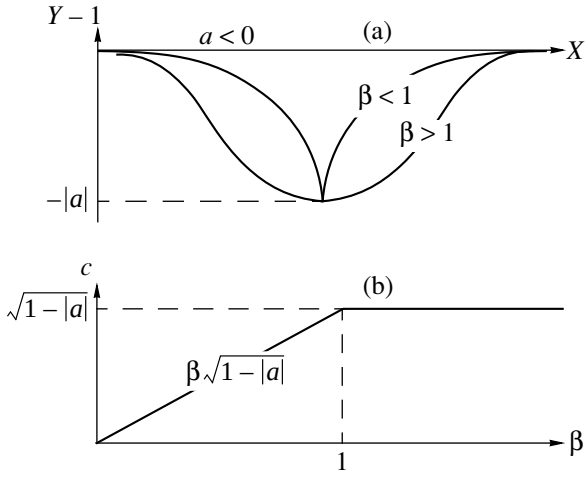

Fig. 3.

numbers. As β increases from zero to infinity, the soliton area increases from zero to infinity. At the lower point, the curvature is infinite for $0 < \beta < 1$ and monotonically decreases from infinity to zero as β increases from unity to infinity. At a constant negative amplitude, the soliton velocity is proportional to β for $\beta < 1$ and is β-independent for $\beta > 1$ (Fig. 3b).

ACKNOWLEDGMENTS

The author is grateful to A.G. Kulikovskiĭ for his fruitful remarks and to G.G. Chernyĭ for his attention to this study.

REFERENCES

1. Yu. A. Drozdova and A. G. Kulikovskiĭ, Izv. Akad. Nauk, Mekh. Zhidk. Gaza, No. 5, 136 (1996).
2. Yu. A. Madsen and H. A. Shaffer, Philos. Trans. R. Soc. London, Ser. A **356**, 3123 (1998).
3. L. N. Sretenskiĭ, *Theory of Wave Motion of a Fluid* (Nauka, Moscow, 1977).
4. E. V. Laitone, J. Fluid Mech. **9**, 430 (1960).
5. V. I. Smirnov, *A Course of Higher Mathematics* (Nauka, Moscow, 1974; Addison-Wesley, Reading, 1964), Vol. 4, Part 1.
6. Li Zhi and N. R. Sibgatullin, Prikl. Mat. Mekh. **61**, 184 (1997).
7. B. T. Brook, Quart. J. Appl. Mech. **40**, 231 (1982).
8. A. G. Petrov and V. G. Smolyanin, Vestn. Mosk. Univ., Ser. 1: Mat., Mekh., No. 3, 92 (1991).
9. G. Yoss and K. Kirchgassner, Proc. R. Soc. Edinburgh, Sect. A **122**, 267 (1992).
10. F. L. Chernous'ko, Prikl. Mat. Mekh. **29** (5), 856 (1995).

Translated by V. Tsarev

Doklady Physics, Vol. 45, No. 8, 2000, pp. 430–433. Translated from Doklady Akademii Nauk, Vol. 373, No. 6, 2000, pp. 467–470.

MECHANICS

Macrostructure and Microstructure of a Cocurrent Stratified Flow behind a Cylinder

Yu. D. Chashechkin and V. V. Mitkin

Presented by Academician A.Yu. Ishlinskiĭ December 1, 1999

Received December 7, 1999

High-resolution optical and probe methods are used to isolate not only large-scale elements (internal waves immersed into a wake and soaring vortices) in a continuously stratified fluid flow around a two-dimensional obstacle but also internal boundary flows. The latter represent thin high-gradient interlayers inside and, sometimes, outside a cocurrent flow [1]. An advancing disturbance and both internal waves and vortices in a lagging wake behind the obstacle, which were investigated in detail by experimental and theoretical methods, are presented in [2–4]. Parameters of high-gradient shells that belong to the density wake and contact with the boundary layer on the obstacle are determined in [5]. Patterns of internal boundary flows in the field of attached internal waves, which are obtained by different shadow methods, can be found in [6]. In the present paper, we, for the first time, have experimentally determined boundaries for a domain of existence (in the coordinate plane given by the Froude and Reynolds numbers) of isolated discontinuities in a wave wake behind a cylinder. We have also shown that the structure of the extended regime diagram depends on a stratification level. The usually assumed universal character of the extended diagram [3, 4] violates due to an allowance for the entire complex of steadily observed elements, which include fine-structure components of both the wave wake and density wake.

Dimensional parameters of the problem are the density $\rho(z)$ and its vertical gradient $\frac{d\rho}{dz}$, the free-fall acceleration g, the diameter D and the velocity U of the cylinder, the kinematic fluid viscosity ν, and the diffusion coefficient κ_s of a component causing stratification. The exponential stratification is characterized by the scale $\Lambda = \left(\frac{d\ln\rho}{dz}\right)^{-1}$, the buoyancy frequency $N = \sqrt{g/\Lambda}$, and the buoyancy period $T_b = 2\pi/N$. Internal scales of the problem are presented by the thicknesses of the velocity boundary layer ($\delta_u = \nu/U$) and of the density boundary layer ($\delta_\rho = \kappa_s/U$), both formed on the obstacle, and the length of the attached internal wave $\lambda = UT_b$. Both internal boundary flows and unsteady flows induced by diffusion on an impermeable surface [7] are characterized by the scales of velocity $\delta_\nu = \sqrt{\nu/N}$ and density $\delta_s = \sqrt{\kappa_s/N}$. The basic dimensionless parameters are presented by ratios between the internal scales. They are the Reynolds number $\mathrm{Re} = UD/\nu = D/\delta_u$, the internal Froude number $\mathrm{Fr} = U/ND = \lambda/2\pi D$, the scale ratio $C = \Lambda/D$, and the Schmidt number $\mathrm{Sc} = \nu/\kappa_s = \delta_u/\delta_\rho \approx 700$ (the Schmidt number was constant during the experiments). The necessity of recording all elements of the flow pattern puts forward strict requirements to experimental equipment. It is the highest resolution shadow instruments that actually satisfy this necessity [8].

The experiments were carried out in a tank with volume of $220 \times 40 \times 60$ cm^3. It had transparent windows and was filled with a stratified solution of common salt with the buoyancy period T_b from 5.3 to 25 s. Monitoring of both the homogeneity and the stratification level was carried out by the method of a density marker [9]. Plastic horizontal cylinders were towed in the tank with the constant speed U = 0.01–6.5 cm/s. They had the diameter D = 1.5–7.6 cm and a length equal to the tank width. Monitoring of motion uniformity was carried out by an optical method. The experiments were conducted at the following values of the dimensionless problem parameters: $10 < \mathrm{Re} < 5000$, $0.008 < \mathrm{Fr} < 8$, and $100 < C < 15\,000$.

We performed the observations by the IAB-451 and IAB-458 shadow instruments using Maksutov methods [10]. The most detailed flow-pattern structure in the vertical plane is obtained by the method called "Vertical slit–thread in focus" (Fig. 1). It is characterized by the complete set of scales intrinsic to the problem. The obstacle dimension D determines the vertical size of a region occupied by the fluid held in front of the body. The length λ characterizes unsteady internal waves, which smoothly turn into attached waves behind the obstacle. The scales δ_u and δ_ρ determine the thickness

Institute for Problems in Mechanics,
Russian Academy of Sciences,
pr. Vernadskogo 101, Moscow, 117526 Russia

1028-3358/00/4508-0430$20.00

of a shell for the velocity wake and density wake, respectively, at points of flow separation from the obstacle. The scales δ_v and δ_s characterize isolated interlayers that are formed in the field of internal waves and are separated from both the wake and the body by a fluid layer free from fine-structure features.

At small values of the Reynolds number (Re < 200) and moderate values of the Froude number (Fr < 1.2), the density wake splits into separate extended interlayers, whose deformation reflects distribution of wave-induced displacements behind the body. Darker lines visualize crests of unsteady waves and attached internal waves, where the former arise in front of the body and the latter, behind it. Binary light gray lines show wave troughs. The wave field is asymmetric with respect to the central horizontal plane. Wave surfaces behind the body in the quiescent fluid represent semicircles [11]. Actual shapes of the crests and the troughs differ from the calculated ones due to the Doppler effect in the flow layer with a velocity shift. A wavelength measured along a normal to the phase surface is equal to λ_u = 4 cm in the upper half-space and to λ_b = 3.1 cm in the bottom half-space. The difference is caused by the dependence of the buoyancy period on the depth (T_b = 15.0 s above the line drawn by the moving center of the body and T_b = 11.3 s below this line).

Here, the high-gradient interlayers do not form an entire exterior high-gradient shell of the density wake, as is observed in many other regimes [5]. Therefore, the attached internal waves pass through the density wake. Crests and troughs from the upper and lower half-spaces join consecutively, forming a single wave system. The shape of the connecting line inside the density wake varies with increasing distance from the obstacle, which reflects the complex vortex structure of the wake and the dependence of the buoyancy period on the depth.

Horizontal high-gradient interlayers formed in the field of attached internal waves are situated at a distance h = 3.1 cm from the wake axis. The leading edge of the interlayers is situated in the region of maximum amplitudes of the internal waves and lies at a distance of r = 4 cm from the cylinder center. The thickness of these interlayers depends weakly on parameters of the motion, while their length grows with increasing the Froude number and, under the conditions of this experiment, substantially exceeds the dimension of the window. In the case of slower motion, when these interlayers are not long [1, 6], their back and front edges are free from singularities.

Analysis of the experimental data shows that, in both strongly (T_b = 6.0 s) and weakly (T_b = 12.5 and 20.5 s) stratified fluid, isolated discontinuities are observed in the field of attached internal waves near the cylinders having the diameters D from 1.5 to 7.6 cm and towed with the speed U = 0.04–0.5 cm/s if values of the internal Froude number are small (0.02 < Fr < 0.5) and the Reynolds number is moderate (30 < Re < 500).

Fig. 1. Shadow pattern of a flow with isolated soaring discontinuities in the field of attached internal waves. A cylinder with the diameter D = 2.5 cm moves from the left to the right at a speed of U = 0.29 cm/s. The other parameters are T_b = 15 s, Fr = 0.28, Re = 74, and C = 5500.

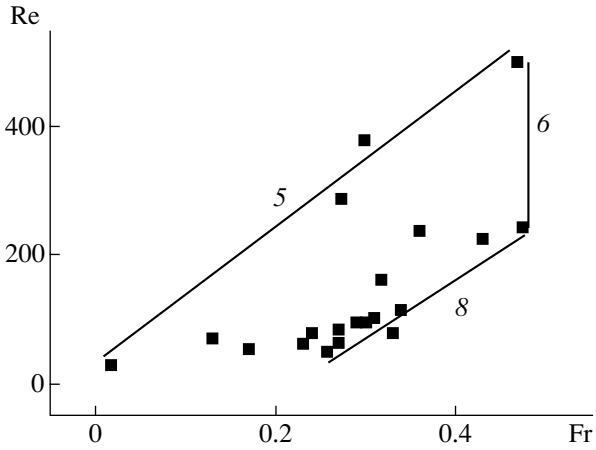

Fig. 2. Domain of existence of isolated soaring discontinuities arising in the field of attached internal waves in the coordinate plane composed of the Froude and Reynolds numbers. Flow regimes are classified according to Figs. 3 and 4: (*5*) the regime of soaring vortices, (*6*) vortex filaments in the wake, and (*8*) the density wake split into wave-and-vortex interlayers.

Similarly to papers [3, 4], a domain of existence of this flow regime is shown in the plane given by the Froude and Reynolds numbers (Fig. 2). The regime of curls [3] or vortices [4] soaring in the field of attached internal waves is realized to the left of this domain at small values of the Froude number (Fr < 0.3). Then, a multipole vortex system [4] forms at the front interlayer edge in the region of maximum amplitudes of the internal waves. This system is a source of its own density wake presented by a rectilinear or wavelike high-gradient interlayer. With increasing the Reynolds number, a flow

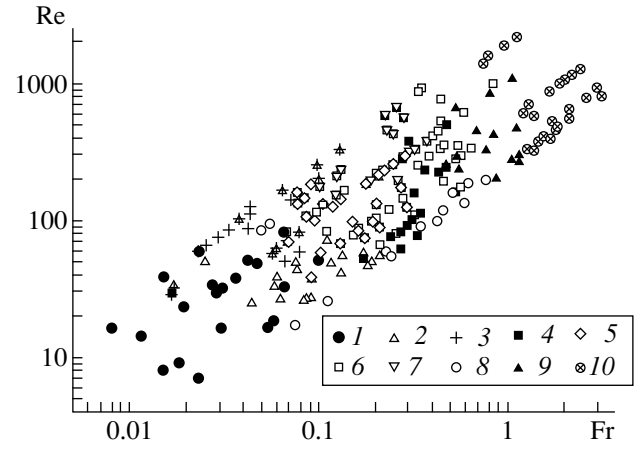

Fig. 3. Diagram of flow regimes at strong stratification ($C < 2000$).

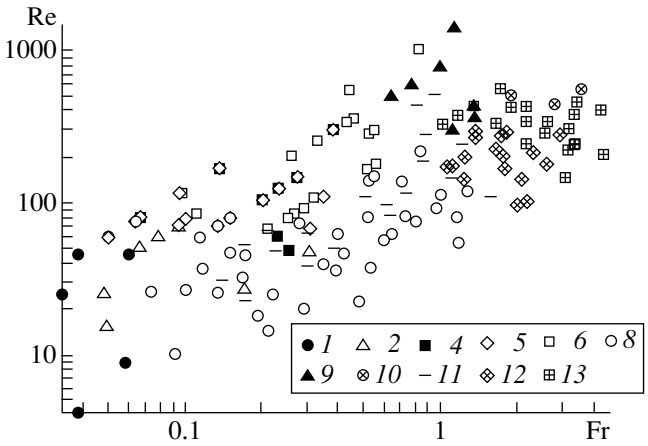

Fig. 4. Diagram of flow regimes at weak stratification ($C > 2000$).

pattern at the front edge of the interlayer becomes more complicated; i.e., a larger number of vortices are being identified in it [4]. A line that separates the regimes of soaring vortices from those of isolated discontinuities is given by the relation Re = 1200Fr + 15.

Two flow types exist to the right of the region of the isolated discontinuities. At small values of the Reynolds number (Re < 200), the flow pattern is the simplest. It includes only an advancing disturbance, internal waves, and a density wake split into separate oblique interlayers [4]. A boundary between these regimes is given by the relation Re = 960Fr – 215. At large values of the Reynolds number (Re > 200 and Fr > 0.5), the vertical wake dimension grows and decreases cyclically with the distance from the body. Horizontal vortex filaments (vortex bubbles [3]) appear in the regions of wake widening, their positions being determined by the phase structure of the attached internal waves.

Allowing for steadily reproducible small-scale components in a stratified-flow pattern behind the cylinder, the regime map loses its universality and becomes dependent on the scale ratio C. For the strong stratification of the fluid ($C < 2000$, see Fig. 3), within the parameter ranges under investigation ($5.3 < T_b < 25$ s, $1.5 < D < 7.6$ cm, and $0.01 < U < 6.5$ cm/s), we observe different flow regimes (according to the classification performed towards increasing values of the Froude and Reynolds numbers). They are a wake (*1*) with a split high-gradient shell; a wake (*2*) with a central high-gradient interlayer in which a microscale instability (*3*) develops [12]; isolated discontinuities (*4*) in the field of attached internal waves with an adjacent regime of soaring vortices (*5*) arising at the front edges of the discontinuities. At $0.1 < Fr < 1$ and $80 < Re < 1000$, the internal waves strongly deform the cocurrent flow, and isolated vortex filaments (*6*) are observed in regions of wake widening. Near regions of wake narrowing, trains of soaring vortex systems, which are separated from the wake by a fluid layer (*7*) free from fine-structure disturbances, are formed in the field of internal waves. Points corresponding to a regime of cusped wave-and-vortex objects (*8*), in which there is no whole high-gradient shell of the density wake, are situated at the lower boundary of the given parameter range. At Re > 200 and $0.45 < Fr < 1.4$, a narrow turbulent wake (*9*) is observed behind the cylinder. At Re > 350 and Fr > 1, turbulent vortex objects (*10*) are formed inside the density wake. Overlapping the regimes occurs at small and moderate values of the Froude number ($0.02 < Fr < 1$ and $20 < Re < 1000$).

The regime map has a clearer structure in a weakly stratified fluid ($C > 2000$). It is shown in Fig. 4, where the notation used in Fig. 3 is preserved for repeated flow types. Similarly to the previous case, the laminar cocurrent flow with the split high-gradient shell (*1*), which occurs at Fr < 0.02 and Re < 40, is changed by the wake (*2*) having the central high-gradient interlayer as the Reynolds number increases. At Re > 70 and Fr < 0.1, the isolated discontinuities (*4*) and the soaring vortices (*5*) arise in the field of attached internal waves. At Fr > 0.1, the separate vortex filaments (*6*) or the oblique wave-and-vortex interlayers (*8*) are observed in the density wake. In the last case, at small values of the Reynolds number and moderate values of the Froude number, there is no entire high-gradient shell of the density wake (*8*) split into separate layers and interlayers. When the speed increases, an attached vortex forms both in the bottom part of the body and in the uniform fluid. Dynamics of its intrinsic motion generates characteristic wake elements with longitudinal scales differing from a wavelength of the attached internal wave. At Re > 200, Fr > 0.7, as in strongly stratified fluid, the narrow turbulent wake (*9*) is observed rather than the wider turbulent flow with separate vortex elements (*10*) at Re > 350 and Fr > 1.

Furthermore, we discuss flow regimes that are present in the diagram and are absent in strongly strat-

ified fluid. Within a wide range of the parameters, there is an undular wake (*11*) for which the scale of longitudinal variation is determined by the period of natural oscillations of the bottom vortex. An increase in the wake speed leads to the growth of the amplitude of the wake transverse oscillations. In this case, laminar vortices forming the Strouhal–Karman vortex street (*12*) enter the wake sequentially. At a still higher speed, when the flow inside the bottom vortex becomes irregular, an array of turbulent vortices (*13*) forms in the wake.

Qualitative features of the regime maps presented in Figs. 3 and 4 differ essentially from each other. For weak stratification, domains of existence of the mentioned flow regimes are compact and, at relatively large values of the Froude and Reynolds numbers, have clear boundaries. For strong stratification, domains for the existence of the given regimes in the parameter space are being extended. Moreover, at close values of the parameters, three and more flow types can exist around the bodies differing in their diameters. The observed ambiguity of the flow regimes (each of them actually forms a compact domain in the three-dimensional parameter space given by the Froude and Reynolds numbers and the scale ratio) testify to the incompleteness of the plane regime map [3, 4] and the necessity of constructing the three-dimensional map in the *C*-, Fr-, and Re-axes. In general, the regimes should be classified in the four-dimensional space given by the Froude, Reynolds, and Peclet numbers as well as the scale ratio.

ACKNOWLEDGMENTS

This work was supported by the Ministry of Science and Technology of Russian Federation (the Program for supporting unique instrumentation) and the Russian Foundation for Basic Research (project no. 99–05–64980).

REFERENCES

1. Yu. D. Chashechkin and V. V. Mitkin, Dokl. Akad. Nauk **362**, 625 (1998) [Dokl. Phys. **43**, 636 (1998)].
2. P. G. Baines, *Topographic Effects in Stratified Flows* (Cambridge Univ. Press, Cambridge, 1995).
3. D. L. Boyer, P. A. Davies, H. J. S. Fernando, *et al.*, Philos. Trans. R. Soc. London, Ser. A **328**, 501 (1989).
4. Yu. D. Chashechkin and I. V. Voeĭkov, Izv. Akad. Nauk, Fiz. Atmos. Okeana **29**, 821 (1993).
5. I. V. Voeĭkov and Yu. D. Chashechkin, Izv. Akad. Nauk, Mekh. Zhidk. Gaza, No. 1, 20 (1993).
6. V. V. Mitkin, Cand. Sci. (Phys.–Math.) Dissertation (Moscow, Inst. Probl. Mech., Russ. Acad. Sci., 1998), p. 111.
7. V. G. Baĭdulov and Yu. D. Chashechkin, Izv. Akad. Nauk, Fiz. Atmos. Okeana **29**, 666 (1993).
8. L. A. Vasil'ev, *Shadow Methods* (Nauka, Moscow, 1968).
9. S. A. Smirnov, Yu. D. Chashechkin, and Yu. S. Il'inykh, Izmer. Tekh., No. 6, 15 (1998).
10. D. D. Maksutov, *Shadow Methods for Researching Optical Systems* (Gostekhteorizdat, Moscow, 1934).
11. M. J. Lighthill, *Waves in Fluids* (Cambridge Univ. Press, Cambridge, 1978; Mir, Moscow, 1981).
12. V. V. Voeĭkov, V. E. Prokhorov, and Yu. D. Chashechkin, Izv. Akad. Nauk, Mekh. Zhidk. Gaza, No. 3, 3 (1995).

Translated by Yu. Verevochkin